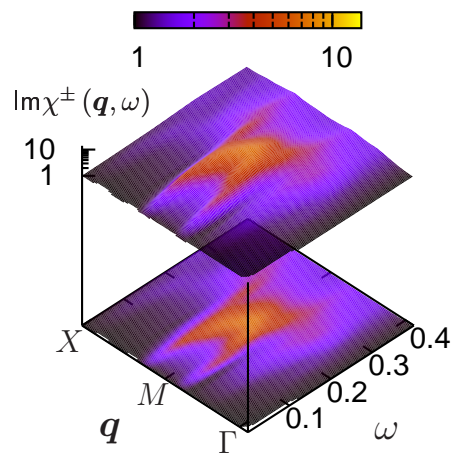


Two-Particle Excitations in the Hubbard Model for High-Temperature Superconductors: A Quantum Cluster Study



Dissertation zur Erlangung des
naturwissenschaftlichen Doktorgrades
der Bayerischen Julius-Maximilians-Universität Würzburg

vorgelegt von

SASCHA BREHM

aus Fulda

Würzburg 2009

Two-Particle Excitations in the Hubbard Model for High-Temperature Superconductors: A Quantum Cluster Study

Dissertation zur Erlangung des
naturwissenschaftlichen Doktorgrades
der Bayerischen Julius-Maximilians-Universität Würzburg

vorgelegt von

SASCHA BREHM

aus Fulda

Würzburg 2009



Eingereicht am 26.02.2009

bei der Fakultät für Physik und Astronomie

1. Gutachter: Prof. Dr. Werner Hanke

2. Gutachter: Prof. Dr. Enrico Arrigoni

der Dissertation

1. Prüfer: Prof. Dr. Werner Hanke

2. Prüfer: Prof. Dr.

3. Prüfer: Prof. Dr.

im Promotionskolloquium

Tag des Promotionskolloquiums: __. __. 2009

Doktorurkunde ausgehändigt am: __. __. 2009

Explanation of the plot on the front page:

The plot of the imaginary part of the transverse magnetic susceptibility $\text{Im}\chi^\pm(\mathbf{q}, \omega)$ exhibits the prominent resonance mode calculated with our two-particle extension of the Variational Cluster Approach in the hole-doped ($x = 0.18$) Hubbard model at $T = 0$. This salient structure is observed in cuprate superconductors by use of Inelastic Neutron Scattering experiments. Being a universal property of the cuprates, the resonance is believed to be closely related to the mechanism of high-temperature superconductivity. As an upward as well as a downward dispersion exists, the plotted structure is also called *hourglass* structure which we obtained for the first time in a strongly correlated microscopic calculation without free parameters. In addition, characteristic properties such as the doping dependencies are proved to be in accord with the experiments. This can be considered as the most important achievement of this thesis. Further explanations are given in this work or in (1).

Erläuterungen zu dem Plot auf der Titelseite:

Der Plot des Imaginärteils der transversalen magnetischen Suszeptibilität $\text{Im}\chi^\pm(\mathbf{q}, \omega)$ zeigt die bekannte Resonanzmode, welche mit Hilfe unserer Zwei-Teilchen Erweiterung des Variational Cluster Approach im loch-dotierten ($x = 0.18$) Hubbard model bei $T = 0$ berechnet wurde. Diese besondere Struktur wird in Kuprat Supraleitern im Rahmen Inelastischer Neutronenstreu Experimente beobachtet. Als universelle Eigenschaft der Kuprate wird die Resonanzmode weithin akzeptiert als eng verbunden mit dem Mechanismus der Hochtemperatur-Supraleitung gesehen. Da sowohl eine obere als auch eine untere Dispersion existiert, bezeichnet man die abgedruckte Struktur auch als *hourglass* Struktur, welche wir erstmals im Rahmen einer stark korrelierten mikroskopischen Technik ohne freie Parameter berechnet haben. Darüber hinaus zeigen sich weitere charakteristische Eigenschaften, wie z.B. Dotierungsabhängigkeiten, als übereinstimmend mit den Experimenten. Dies kann als die wichtigste Errungenschaft dieser Dissertation angesehen werden. Weitere Erläuterungen sind dieser Arbeit oder (1) zu entnehmen.

In Liebe für Eva und meine Eltern

Abstract

Two-particle excitations, such as spin and charge excitations, play a key role in high- T_c cuprate superconductors (HTSC). Due to the antiferromagnetism of the parent compound the magnetic excitations are supposed to be directly related to the mechanism of superconductivity. In particular, the so-called resonance mode is a promising candidate for the *pairing glue*, a bosonic excitation mediating the electronic pairing. In addition, its interactions with itinerant electrons may be responsible for some of the observed properties of HTSC. Hence, getting to the bottom of the resonance mode is crucial for a deeper understanding of the cuprate materials .

To analyze the corresponding two-particle correlation functions we develop in the present thesis a new, non-perturbative and parameter-free technique for $T = 0$ which is based on the Variational Cluster Approach (VCA, an embedded cluster method for one-particle Green's functions). Guided by the spirit of the VCA we extract an effective electron-hole vertex from an isolated cluster and use a fully renormalized *bubble* susceptibility χ_0 including the VCA one-particle propagators. Within our new approach, the magnetic excitations of HTSC are shown to be reproduced for the Hubbard model within the relevant strong-coupling regime. Exceptionally, the famous resonance mode occurring in the underdoped regime within the superconductivity-induced gap of spin-flip electron-hole excitations is obtained. Its intensity and *hourglass* dispersion are in good overall agreement with experiments. Furthermore, characteristic features such as the position in energy of the resonance mode and the difference of the imaginary part of the susceptibility in the superconducting and the *normal* states are in accord with Inelastic Neutron Scattering (INS) experiments. For the first time, a strongly-correlated parameter-free calculation revealed these salient magnetic properties supporting the $S=1$ magnetic exciton scenario for the resonance mode.

Besides the INS data on magnetic properties further important new insights were gained recently via ARPES (Angle-Resolved Photoemission-Spectroscopy) and Raman experiments which disclosed a quite different doping dependence of the antinodal compared to the near-nodal gap. This thesis provides an approach to the Raman response similar to the

magnetic case for inspecting this gap dichotomy. In agreement with experiments and one-particle data obtained in the VCA, we recover the antinodal gap decreasing and the near-nodal gap increasing as a function of doping. Hence, our results prove the Hubbard model to account for these salient gap features.

In summary, we develop a two-particle cluster approach which is appropriate for the strongly-correlated regime and contains no free parameter. Our results obtained with this new approach combined with the phase diagram and the one-particle excitations obtained in the VCA strongly constitute a Hubbard model description of HTSC cuprate materials.

Kurzfassung

Zwei-Teilchen Anregungen, darunter Spin und Ladungs Anregungen, sind von besonderer Bedeutung in Hoch- T_c Kuprat Supraleitern (HTSL). Aufgrund der antiferromagnetischen Phase bei niedrigen Dotierungen werden magnetische Anregungen direkt mit dem Mechanismus der Supraleitung in Verbindung gebracht. Gerade die sogenannte Resonanzmode ist ein vielversprechender Kandidat für den *pairing glue*, eine bosonische Anregung, welche die Paarung von Elektronen induziert. Weiterhin wird deren Wechselwirkung mit itineranten Elektronen verantwortlich gemacht für einige der beobachteten Eigenschaften der HTSL. Für ein tieferes Verständnis der Kuprate ist es daher unerlässlich, der Resonanzmode auf den Grund zu gehen. Um die entsprechenden Zwei-Teilchen Korrelationsfunktionen zu analysieren, entwickeln wir auf Basis des Variational Cluster Approach (VCA, eine Cluster Methode, um Ein-Teilchen Green Funktionen zu berechnen) in der vorliegenden Dissertation eine neue, nicht-perturbative und parameterfreie Technik für $T = 0$. Im Sinne der VCA berechnen wir einen effektiven Elektron-Loch Vertex auf einem einzelnen Cluster und verwenden eine vollkommen renormierte *Bubble* Suszeptibilität χ_0 , welche die VCA Ein-Teilchen-Propagatoren beinhaltet. Mit Hilfe unserer neuen Technik können wir die magnetischen Anregungen der HTSL im Rahmen des Hubbard Modells in der stark korrelierten Phase reproduzieren. Als herausragendes Ergebnis erhalten wir die berühmte Resonanzmode im underdotierten Bereich innerhalb des von der Supraleitung induzierten Gaps der Spin-Flip Elektron-Loch Anregungen. Deren Intensität und Sanduhrenförmige Dispersion zeigen eine sehr gute Übereinstimmung mit den Experimenten. Weiterhin sind charakteristische Eigenschaften, wie die Energie der Resonanzmode oder die Differenz des Imaginärteils der Suszeptibilität in der supraleitenden und *normalen* Phase im Einklang mit Inelastischen Neutronenstreu (INS) Experimenten. Zum ersten Mal bringt eine stark-korrelierte und parameterfreie theoretische Rechnung diese besonderen magnetischen Eigenschaften hervor und bekräftigt damit die Erklärung der Resonanzmode als $S=1$ magnetisches Exziton.

Neben den INS Resultaten zu magnetischen Eigenschaften wurden kürzlich weitere wichtige neue Erkenntnisse mittels ARPES (Winkelaufgelöste Photoemissionen Spektroskopie) und Raman Experimenten erhalten. Beide legten eine deutlich unterschiedliche Dotierungsab-

hängigkeit des anti-nodalen Gaps verglichen mit dem Gap nahe des nodalen Punktes offen. Im Rahmen dieser Dissertation wird eine der magnetischen Berechnung ähnliche Technik für den Raman Response benutzt, um dieses unterschiedliche Verhalten des Gaps zu untersuchen. Übereinstimmend mit den Experimenten und Ein-Teilchen Ergebnissen aus VCA Rechnungen bekommen wir ein Abfallen des anti-nodalen Gaps und Ansteigen des Gaps nahe dem nodalen Punkt als Funktion der Dotierung. Folglich zeigen unsere Ergebnisse, dass das Hubbard Modell diese besonderen Eigenschaften des Gaps beinhaltet.

Zusammenfassend entwickeln wir eine Zwei-Teilchen Cluster Technik, welche für stark korrelierte Systeme geeignet ist und keine freien Parameter enthält. Unsere Ergebnisse mit dieser neuen Technik in Verbindung mit dem Phasendiagramm und Ein-Teilchen Anregungen der VCA Rechnungen bekräftigen mit Nachdruck eine Beschreibung der HTSL Kuprate auf Basis des Hubbard Modells.

Definitions, notations and abbreviations

Throughout the present thesis the following definitions, notations and abbreviations are often used:

- The bold face type is used to denote vectors as well as matrices.
- In the Brillouin zone the following symmetry points are used:

$$\begin{aligned}\Gamma &= (0, 0) \\ X &= (\pi, 0) \\ M &= (\pi, \pi)\end{aligned}$$

- The following abbreviations are often used:

HTSC	=	high-temperature superconductor
LASCO	=	$La_{2-\delta}A_{\delta}CuO_4$, with $A = Sr$ or $A = Ba$
YBCO	=	$YBa_2Cu_3O_{6+\delta}$
VCA	=	Variational Cluster Approach
SFA	=	Self-Energy-Functional Approach
ARPES	=	Angle-Resolved Photoemission-Spectroscopy
INS	=	Inelastic Neutron Scattering

Contents

1	Introduction	1
1.1	Chemical structure of cuprate superconductors	2
1.2	Physical basics of cuprate superconductors	3
1.3	Purpose of the present thesis	7
2	Physical models	11
2.1	Three-band Hubbard model	12
2.2	One-band Hubbard model	13
2.2.1	Conserving quantities	14
2.2.2	Particle-hole-transformation	15
2.2.3	$U = 0$ limit	15
2.2.4	Large U limit	15
3	Techniques	17
3.1	Variational Cluster Approach (VCA)	18
3.1.1	Self-Energy-Functional Approach	18
3.1.2	Derivation of the Variational Cluster Approach (VCA)	22
3.1.3	Translational invariance	26
3.1.4	Limits of the VCA	27
3.1.5	Choice of variational parameters and thermodynamic consistence	27
3.1.6	Q-matrix formalism - Numerical evaluation	29
3.2	Two-particle extension of the VCA for the magnetic susceptibility	31
3.2.1	Approximation to the Bethe-Salpeter equation	32
3.2.2	<i>Dressed bubble</i> approximation to the magnetic susceptibility	35
3.2.3	Effective vertex	40
3.2.4	Controlling constant α - Checksum	42
3.3	Inelastic light scattering - Raman response	43
3.3.1	<i>Dressed bubble</i> approximation to the Raman response	43

3.3.2	Effective mass approximation to the Raman vertex	45
3.4	Exact Diagonalization using the (Block-)Lanczos algorithm	47
3.4.1	Krylov space	47
3.4.2	(Block-)Lanczos	49
4	Magnetic correlations in high-T_c superconductors	51
4.1	Preliminaries to the Hubbard model within the VCA	52
4.1.1	Choice of the reference clusters	53
4.2	Antiferromagnetic phase	55
4.3	Superconducting phase	59
4.4	Controlling constant α	64
4.4.1	Results with $\alpha = 1$	65
5	Raman response in high-T_c superconductors	67
5.1	Raman vertex in the effective mass approximation	68
5.2	Superconducting phase	71
5.3	<i>Normal</i> state - Paramagnetic phase	73
6	Summary	75
A	Appendix	79
A.1	Restoring the translational invariance	79
A.2	Matsubara frequency sums	80
A.2.1	Analytic evaluation of the $i\omega$ -sum	80
A.2.2	Numerical evaluation of the $i\omega$ -sum	81
A.3	Particle-hole transformation in one spin-channel	84
A.4	Avoiding singularities in the vertex function	86
	Bibliography	87
	Danksagung	93
	Versicherung an Eides statt	95

List of Figures

1.1	Sketch of the chemical elementary cell of $YBa_2Cu_3O_7$ (YBCO). The bold dashed lines indicate the CuO_2 planes.	3
1.2	Sketch of the chemical elementary cell of La_2CuO_4 (LASCO). The bold dashed lines indicate the CuO_2 planes.	4
1.3	Generic phase diagram of cuprate superconductors.	5
1.4	Schematic visualization of the super-exchange mechanism.	6
1.5	Schematic visualization of the instantaneous pairing mechanism within a quadratic lattice in the antiferromagnetic phase.	9
2.1	Sketch of the three-band model for the CuO_2 planes in the cuprates.	12
2.2	Phase convention for the hopping matrix elements of the three-band Hubbard model.	13
2.3	Sketch of the one-band model for the CuO_2 planes in the cuprates with nearest and next-nearest neighbor hopping.	14
3.1	Diagrammatical definition of the Luttinger-Ward functional with double lines depicting the fully interacting Green's function while the dashed lines symbolize the interaction.	19
3.2	Sketch of the approximated stationarity condition in case of two variational parameters. The vector \mathbf{a} indicates the non-vanishing bracket in Eq. (3.14) and is perpendicular to the tangential vectors \mathbf{b}_1 and \mathbf{b}_2 of the \mathbf{t}' parameterized hypersurface.	21
3.3	Tiling up the original real space lattice into N_c finite clusters with L_c sites each. This lattice is called superlattice with the cluster being the elementary cell.	22
3.4	The clustered lattice in real space and the corresponding first Brillouin zone in reciprocal space with the shaded area indicating the reduced Brillouin zone. Note, that for an infinite lattice the \mathbf{k} -points become dense.	26

3.5	Diagrammatic representation of the general Bethe-Salpeter equation. The tiny black lines depict non-interacting one-particle Green's functions.	31
3.6	Diagrammatic representation of the Bethe-Salpeter equation for the magnetic susceptibility. The tiny black lines depict non-interacting one-particle Green's functions.	32
3.7	Diagrammatic representation of the approximated Bethe-Salpeter equation for the magnetic susceptibility. The tiny black lines depict non-interacting one-particle Green's functions.	32
3.8	Diagrammatic representation of the approximated Bethe-Salpeter equation for the magnetic susceptibility with fully dressed one-particle propagators depicted as double lines.	37
4.1	Phase diagram of the hole-doped Hubbard model obtained from a VCA calculation using the $\sqrt{10} \times \sqrt{10}$ cluster (taken from (2)).	53
4.2	Geometry of the clusters used in our calculations: 2×2 , 3×3 , 4×2 and $\sqrt{10} \times \sqrt{10}$	54
4.3	Density plot of $\text{Im}\chi^\pm(\mathbf{q}, \omega)$ at half-filling in the antiferromagnetic phase using the 2×2 cluster.	55
4.4	Density plot of $\text{Im}\chi^\pm(\mathbf{q}, \omega)$ at half-filling in the antiferromagnetic phase using the 4×2 cluster.	55
4.5	Density plot of $\text{Im}\chi^\pm(\mathbf{q}, \omega)$ at half-filling in the antiferromagnetic phase using the $\sqrt{10} \times \sqrt{10}$ cluster.	56
4.6	Plot of $\text{Im}\chi^\pm(\mathbf{q}_{AF}, \omega)$ at half-filling using various clusters.	56
4.7	Density plot of $\text{Im}\chi^\pm(\mathbf{q}, \omega)$ at $x = 0.06$ doping in the mixed antiferromagnetic + superconducting phase using the 2×2 cluster. The red line denote the lower boundary of the spin-flip electron-hole continuum (extracted from Eq. (3.69)).	57
4.8	Plot of $\text{Im}\chi^\pm(\mathbf{q}_{AF}, \omega)$ at various dopings using the 2×2 cluster.	57
4.9	Density plot of $\text{Im}\chi^\pm(\mathbf{q}, \omega)$ at $x = 0.04$ doping in the mixed antiferromagnetic + superconducting phase using the 2×2 cluster.	58
4.10	Density plot of $\text{Im}\chi^\pm(\mathbf{q}, \omega)$ at $x = 0.04$ doping in the mixed antiferromagnetic + superconducting phase using the 4×2 cluster.	58
4.11	Density plot of $\text{Im}\chi^\pm(\mathbf{q}, \omega)$ at $x = 0.04$ doping in the mixed antiferromagnetic + superconducting phase using the $\sqrt{10} \times \sqrt{10}$ cluster.	58
4.12	Plot of $\text{Im}\chi^\pm(\mathbf{q}_{AF}, \omega)$ at $x = 0.04$ doping using various clusters.	58
4.13	Density plot of $\text{Im}\chi^\pm(\mathbf{q}, \omega)$ at $x = 0.18$ doping in the superconducting phase using the 3×3 cluster.	59
4.14	Same as 4.13 but focusing on the <i>hourglass</i> structure. The red line denote the lower boundary of the spin-flip electron-hole continuum (extracted from Eq. (3.69)).	59
4.15	Density plot of the low-energy spectral weight obtained from the corresponding VCA calculation for the one-particle Green's function displaying the Fermi surface with the nodal scattering vector $2\mathbf{k}_N \simeq 0.8(\pi, \pi)$	60

4.16	Lower boundary of the spin-flip electron-hole continuum in the superconducting phase at $x = 0.18$ doping. The plot follows a path along $\mathbf{q} = \eta(\pi, \pi)$ revealing a minimum at $2\mathbf{k}_N \simeq 0.8(\pi, \pi)$. The red line is extracted from Eq. (3.69), while the hatched area is only for reason of visualization.	60
4.17	$\omega_{\text{res}}(\mathbf{q}_{AF})$ as a function of doping.	61
4.18	Doping dependence of the ω -integrated spin-spectral weight at \mathbf{q}_{AF}	61
4.19	Difference between $\text{Im}\chi(\mathbf{q}_{AF}, \omega)$ in the superconducting and normal states at $x = 0.17$ doping.	62
4.20	Density plot of $\text{Im}\chi^\pm(\mathbf{q}, \omega)$ at $x = 0.18$ doping in the <i>normal</i> state using the 3×3 cluster.	62
4.21	Density plot of $\text{Im}\chi^\pm(\mathbf{q}, \omega)$ at $x = 0.15$ doping in the superconducting phase using the 2×2 cluster.	63
4.22	Density plot of $\text{Im}\chi^\pm(\mathbf{q}, \omega)$ at $x = 0.15$ doping in the superconducting phase using the $\sqrt{10} \times \sqrt{10}$ cluster.	63
4.23	Dependence of the controlling constant on the cluster size at half-filling.	64
4.24	Doping dependence of the controlling constant α for the 2×2 cluster.	64
4.25	Density plot of $\text{Im}\chi^\pm(\mathbf{q}, \omega)$ at half-filling in the antiferromagnetic phase using the 2×2 cluster with a fixed $\alpha = 1$	65
4.26	Density plot of $\text{Im}\chi^\pm(\mathbf{q}, \omega)$ at $x = 0.18$ doping in the superconducting phase using the 3×3 cluster with a fixed $\alpha = 1$	65
5.1	Exemplary plot of the spectral function calculated within the VCA at $x = 0.11$ hole-doping in the superconducting phase (white areas mean higher spectral weight). blue: numerically found quasi-particle dispersion ; red: fitted tight-binding dispersion up to 4th nearest neighbors	68
5.2	Doping dependence of the fit parameter within a fit procedure of a tight-binding dispersion to the quasi-particle band up to 4th nearest neighbors in the superconducting phase.	69
5.3	Doping dependence of the fit parameter within a fit procedure of a tight-binding dispersion to the quasi-particle band up to 4th nearest neighbors in the paramagnetic phase.	69
5.4	Density plot of $(\gamma^\nu(\mathbf{k}))^2$ for the B1g and B2g Raman symmetries in the superconducting phase at $x = 0.11$ hole-doping (black area means higher value). The results shown in the left column are obtained from a fitted dispersion up to next-nearest neighbor hopping while the results in the right column stem from a fitted dispersion up to 4th nearest neighbor hopping. The red lines indicate the paths which are used to extract the antinodal (upper row) and near-nodal (lower row) gaps out of the one-particle spectral-function (taken from (3)).	70
5.5	Plot of the B1g Raman spectrum for various hole-dopings in the superconducting phase. $\Delta[\text{Raman}]$ and $2 \times \Delta[\text{SC}]$ are guides to the eye (black: gap extracted from the Raman response; yellow: gap extracted from the one-particle spectral function, taken from (3)).	71

5.6	Plot of the B2g Raman spectrum for various hole-dopings in the superconducting phase. $\Delta[\text{Raman}]$ and $2 \times \Delta[\text{SC}]$ are guides to the eye (black: gap extracted from the Raman response; yellow: gap extracted from the one-particle spectral function, taken from (3)).	71
5.7	Doping dependence of the superconducting gap at the antinodal and near-nodal points extracted from the B1g and B2g Raman spectra.	72
5.8	Doping dependence of the superconducting gap at the antinodal and near-nodal points extracted from the spectral function (taken from (3)).	72
5.9	Plot of the B1g Raman spectrum for various hole-dopings in the paramagnetic phase.	73
5.10	Plot of the B2g Raman spectrum for various hole-dopings in the paramagnetic phase.	73
5.11	Plot of the B1g Raman spectrum for various hole-dopings in the superconducting phase with $\Sigma^{SC} = 0$	74
5.12	Plot of the B2g Raman spectrum for various hole-dopings in the superconducting phase with $\Sigma^{SC} = 0$	74
A.1	Contour deforming from path C_1 over C_2 to C_3 in the complex plane for an analytical summation over Matsubara frequencies of a function with an explicitly known pole structure. Note, that we have to sum over a, in principle, infinite number of Matsubara frequencies. The finite number of paths C_1 and the finite range of the paths C_2 and C_3 is only for reason of visualization.	80
A.2	Contour for the evaluation of a Matsubara sum of a function with poles only in the interval $[-\Omega', 0[$ and $]0, \Omega']$ on the real axis.	82

1

Introduction

The experimental and theoretical research on condensed matter physics and electronic many-body systems is one of the most impressive success stories in science. It is needless to mention the importance of the semiconductor physics making possible the electronic devices which accompany, enrich and change our daily life in an unthinkable short time. And still nowadays the condensed matter physics is an inexhaustible wide field of interesting and very complex problems and phenomena challenging the creativity and intelligence of the scientists. One of the most important parts in this field is the strongly-correlated condensed matter physics. These many-body systems are characterized by a correlation of the particles being of the same magnitude as the band width which is a measure of the kinetic energy. This rules out a perturbative treatment of the interaction as well as the kinetic part in a theoretical approach to these systems. Rather, it is inevitable to take both mechanisms into account for a realistic description. To meet these requirement the development of a variety of new techniques was spurred in the field of the theoretical investigations (see the introduction to chapter 3). One of the most prominent examples for the rich physics of strong correlations was unclosed with the discovery of the copper-oxide (cuprate) high-temperature superconductor (HTSC) $La_{2-\delta}Ba_{\delta}CuO_4$ by J.G. Bednorz and K.A. Müller in the year 1986 (4). That followed a multitude of cuprate superconductors was found and strong effort has been made from many scientists to get to the bottom of the microscopic mechanisms producing the observed macroscopic properties. Although great progress was achieved in the field of the cuprates, it is still a very hot topic and worthy to work intensively in order to prove the roots of the mechanisms producing high-temperature superconductivity.

Conventional low-temperature superconductors as Nb_3Ti with a critical temperature of $T_c \approx 10K$ were discovered in 1911 (5) and are well described by the BCS (Bardeen-Cooper-Schrieffer) theory (6) invented about 45 years afterwards. It was shown that an effective electron-electron interaction mediated by an exchange of phonons (quantized lattice vibrations) is able to lead to a pairing of electrons into cooper pairs. After a Bose-Einstein transition the condensate of cooper pairs can be described by a macroscopic wave-function which

rules out microscopic scattering processes and therefore resistivity. A very important proof of the BCS theory was the comparison of the phonon spectrum, measured by Inelastic Neutron Scattering (INS) experiments, with results from Electron Tunneling experiments. By use of the Eliashberg theory (7) a quantitative agreement was found (8; 9; 10). In addition the BCS theory renders the explanation of the isotope effect (11) which states that the critical temperature is associated with the mass M of the atoms the superconductor consists of via: $T_c M^\alpha = constant$. The exponent is for most conventional superconductors $\alpha \approx 0.5$. Furthermore most thermodynamic properties can be understood on the basis of the so-called BCS mean-field hamiltonian. However, it exists a strong consensus that the theory of phonon-mediated pairing is not applicable to the new HTSC. The reason is that at the relative high critical temperature of for example $T_c \approx 35K$ measured in $La_{1.85}Ba_{0.15}CuO_4$ the thermal excited photons would probably disturb and destroy a phonon-induced pairing mechanism. A further important difference is the strong electron-electron Coulomb interaction in the cuprates in contrast to the weak-coupling conventional superconductors making a description through a mean-field hamiltonian impossible. From 1986 on more and more members of the new class of cuprate superconductors were found with successive higher critical temperatures up to $T_c \approx 160K$ measured in $HgBa_2CaCu_2O_{6+\delta}$ under pressure. A very important cornerstone was the discovery of $YBa_2Cu_3O_{6+\delta}$ (YBCO) as it was the first material becoming superconducting above the liquid nitrogen temperature ($T_c \approx 90K$ for $\delta \approx 1$). Not at last, this made the HTSC an interesting material for industrial use as the superconducting phase can be reached by cooling with the much cheaper liquid nitrogen than liquid helium.

1.1 Chemical structure of cuprate superconductors

Next, we will consider the chemical structure of cuprate superconductors using the example of YBCO and $La_{2-\delta}A_\delta CuO_4$ (LASCO) sketched in Fig. 1.1 and Fig. 1.2, respectively. It is widely believed, that the properties observed in experiments stem from the physics of the two-dimensional CuO_2 planes indicated by the bold dashed lines in Fig. 1.1 and Fig. 1.2. Highly anisotropic properties such the normal state conductivity are justifying this assumption. Under this premise the rest of the chemical structure serves only as a charge reservoir changing the electronic density of the CuO_2 planes. In case of LASCO the stoichiometry is such that the Cu turns into Cu^{2+} , the La into La^{3+} and the oxygen atoms are charged twofold negative. While a single copper atom has a $[3d^{10}][4s^1]$ electronic configuration a copper atom embedded in the crystal is in the $[3d^9]$ configuration. Therefore, every copper ion has one hole in a d-orbital with a spin 1/2 and the 2p-orbitals of the oxygen ions are saturated with two additional electrons $[2p^6]$. The electronic filling of the CuO_2 planes in LASCO can be modified through a substitution of lanthanum atoms with either strontium ($A = Sr$) or barium ($A = Ba$) atoms. The different valence of these elements leads the a lowering of the electronic filling of the CuO_2 planes which means hole(p)-doping. In case of YBCO this is achieved through additional oxide atoms. Also electron(n)-doped materials of the cuprate family were discovered. Examples for n-doped cuprates are $Nd_{2-\delta}Ce_\delta CuO_4$ and $LaPr_{1-\delta}Ce_\delta CuO_4$.

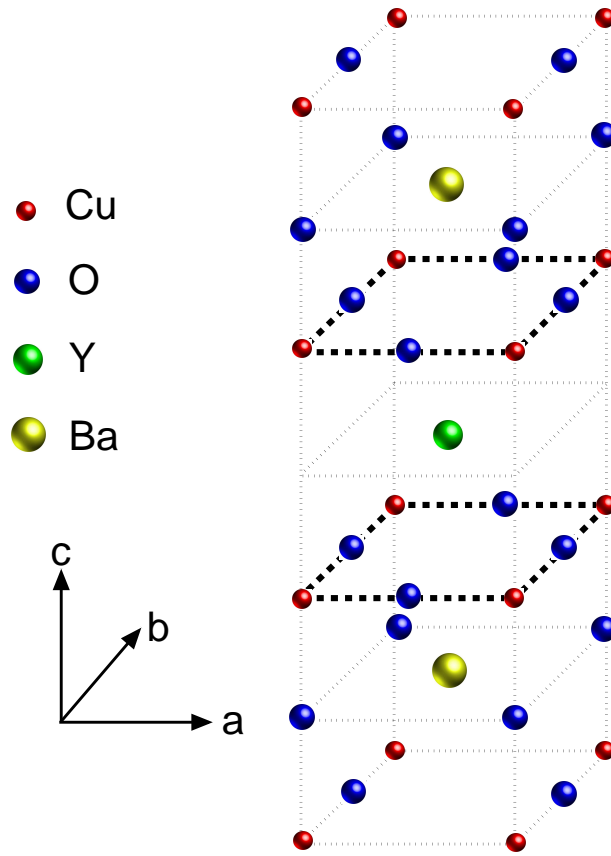


Figure 1.1: Sketch of the chemical elementary cell of $YBa_2Cu_3O_7$ (YBCO). The bold dashed lines indicate the CuO_2 planes.

1.2 Physical basics of cuprate superconductors

Besides the interesting high critical temperature of cuprate superconductors this class of materials also exhibits a rich phase diagram depending strongly on the electronic filling of the CuO_2 planes. Fig. 1.3 shows a generic phase diagram in dependence of the doping x and the temperature T .

At zero doping ($x = 0$) an antiferromagnetic Mott-insulating (12; 13) phase is observed which will be explained briefly. We consider a hypercubic lattice with one orbital per site (this will be detailed in chapter 2) at half-filling. Without an electron-electron interaction, the hopping between lattice sites leads to a metallic band. Switching on a strong local Coulomb interaction between the electrons impedes double occupancy, as an additional electron means an energy cost due to the local Coulomb repulsion denoted with U . Hence, the non-interacting band splits up into two bands (called lower and upper Hubbard band) separated by the Mott-gap U . Although the electrons in this regime at half-filling are localized, virtual hopping processes to and back adjacent sites, which are occupied with an electron carrying an opposite

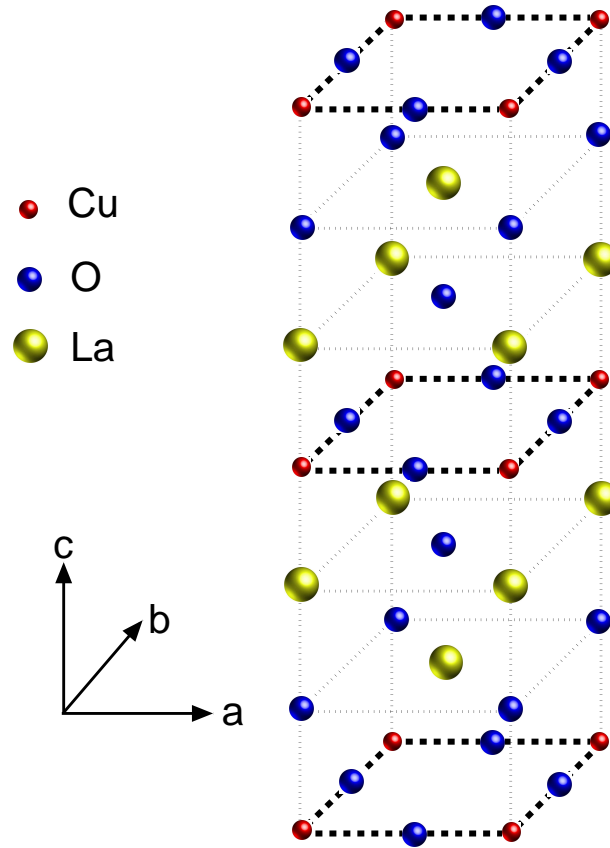


Figure 1.2: Sketch of the chemical elementary cell of La_2CuO_4 (LSCO). The bold dashed lines indicate the CuO_2 planes.

spin, are possible. This so-called super-exchange leads to an antiferromagnetic coupling and is given in two dimensions by $J = 4\frac{t^2}{U}$, with t the nearest-neighbor hopping integral (see Fig. 1.4).

Due to doping the corresponding Néel temperature decreases, but much slower on the n- than the p-doped side of the phase diagram. That followed, the superconducting phase with a maximum critical temperature at a certain value of doping, called optimal doping, is observed. Phase-sensitive experiments revealed that the underlying pairing has a d-wave symmetry in the p-doped as well as in the n-doped regime (see (14) for a review). The superconducting region in the phase diagram below optimal doping is called the underdoped regime. And, complementary, above optimal doping one speaks of the overdoped regime. So far, the observed phase diagram at the p-doped side is richer than at the n-doped side. Experimental results proposing a spin-glass phase in between the antiferromagnetic and the superconducting phase (15; 16; 17; 18) and, furthermore, the so-called pseudogap phase is observed (see (19; 20) for reviews). The characteristic of this phase is a finite superconducting gap without superconductivity.

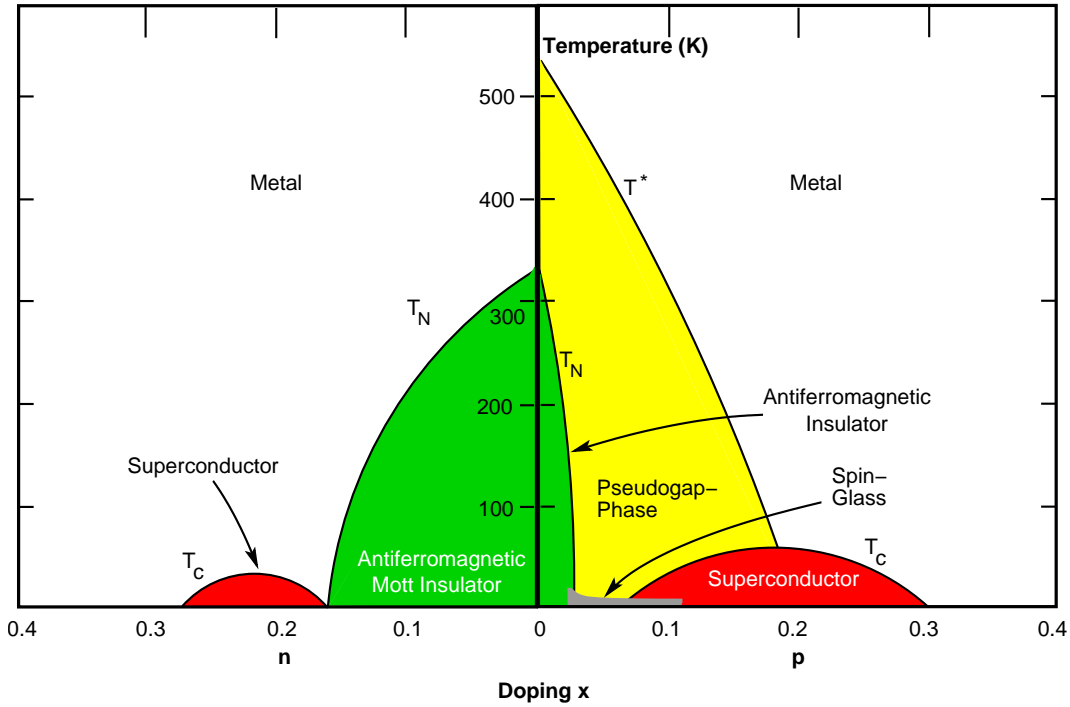


Figure 1.3: Generic phase diagram of cuprate superconductors.

A variety of theories based on a preformed pair scenario was invented to elucidate the physics of the pseudogap phase. Involving spin-charge separation, the Resonating Valence Bond (RVB) for example ascribes the pseudogap to the spin gap produced by spinon pairs below T^* while the holons undergo a Bose-Einstein transition at the critical temperature T_c (21; 22; 23; 24). Another proposed explanation based on preformed pairs is the following. Dynamical charged stripes are separated by insulating antiferromagnetic stripes on a microscopic scale below $T' > T^*$. As the charge carriers are confined in the stripes, an one-dimensional electron gas is formed. Below T^* the spin gap in the antiferromagnetic stripes lead to pairing due to pair-hopping between the antiferromagnetic stripes and the one-dimensional electron gas. Large enough Josephson coupling below T_c creates the phase coherence and therefore superconductivity (25).

In addition, there are theories which try to explain the pseudogap state with phases competing with superconductivity. Possible candidates for such phases are charge density and spin density waves. A further interesting scenario is that of orbital currents circulating around plaquettes of four copper atoms (26; 27; 28; 29; 30; 31) or involving plaquettes of the $Cu - O$ bonds (32; 33).

So far, the nature of this phase is still intensively debated and still unclear.

The proximity of the Mott-insulating antiferromagnetic to the superconducting phase advises us to consider the HTSC as a doped Mott-insulator. A theoretical description is challenged

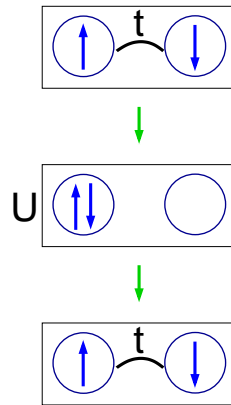


Figure 1.4: Schematic visualization of the super-exchange mechanism.

with the task of explaining these dominant phases as well as the doping-driven evolution from one to the other phase. Against this background the probably most crucial question is the microscopic mechanism of pairing and how it is connected to the antiferromagnetic phase.

Considering the doped antiferromagnetic Mott-insulator one possible short-ranged mechanism of pairing is based on the antiferromagnetic exchange coupling J . Fig. 1.5 sketches the propagation of a single hole compared to a hole-pair on an antiferromagnetic background on a quadratic lattice with one orbital per site. In case of a single hole a tail of parallel spins is produced (upper sketches) which is energetically not favorable. The propagation of a hole-pair avoids this tail (lower sketches). After the hopping of the first hole two frustrations (middle sketch) creating an potential with leads to an attraction between the two holes, as the following second hole lets the frustration disappear (right sketch). Although this is very simplified pictorial argument, it already gives a clue of what is called the instantaneous pairing mechanism involving the virtual high-energy excitations above the Mott gap.

A further possible pairing mechanism is based on the exchange of electron-hole spin fluctuations whose energy dispersion is analyzed in INS experiments (34; 35; 36; 37; 38; 39). Resembling the phonon-induced mechanism in conventional superconductors this retarded spin fluctuation mediated pairing is called the *pairing glue*. Currently, the instantaneous or retarded nature is intensively debated and there is some evidence that both mechanism are accounting for the pairing (40; 41; 42). The mentioned INS experiments revealed an interesting spectrum of electron-spin fluctuations in the underdoped and optimal doped regime. When entering the superconducting state in the high- T_c cuprates, the magnetic excitation spectrum is characteristically and markedly modified: a resonant mode emerges with its peak intensity being highest around the wave vector $\mathbf{q}_{AF} = (\pi, \pi)$ characteristic of antiferromagnetism in the undoped parent compound (34; 35; 36; 37; 38; 39). Its frequency $\omega_{\text{res}}(\mathbf{q}_{AF})$ follows the doping dependence of T_c and is of the order of 40 meV. Away from \mathbf{q}_{AF} , the mode has both a downward and upward *hourglass*-like dispersion with the latter being strongly damped as it extends into the continuum of electron-hole spin-flip excitations. The expression *hourglass* is

meanwhile established for the combined upward and downward dispersion as it is observed in several p-doped cuprate superconductors. In the n-doped cuprates only the resonance peak is detected as an universal feature so far (43). A variety of experiments in the HTSC, such as Angle-Resolved Photoemission-Spectroscopy (ARPES), Optical and Tunneling Spectroscopies, have been interpreted as evidence of interactions of electrons with this mode (44; 45; 46). However its microscopic origin, in particular its role in pairing and the more detailed effects arising from the interactions of charge carriers with this magnetic mode are still unclear and intensively debated (47; 48; 49; 50; 51; 52; 53). A prerequisite to resolve this debate obviously requires a consistent theoretical description of the neutron resonance mode and, more generally, the magnetic excitation spectrum (54; 55; 56) and at the same time of the phase diagram, containing the competing antiferromagnetic and superconducting phases.

1.3 Purpose of the present thesis

In this thesis, on the basis of a microscopic theory for two-particle excitations, we provide a consistent description for the experimentally relevant regime of the two-dimensional one-band Hubbard model. This is a simplified model derived from the chemical structure of the CuO_2 planes which is believed to contain the essential microscopic physics of the cuprates. Chapter 2 is devoted to this issue and introduces the three-band (57) and one-band (58) Hubbard model.

Chapter 3 contains the technical approaches used in the present thesis. We start in section 3.1 with a review of the Variational Cluster Approach (VCA), its derivation from the Self-Energy-Functional Approach (SFA) and the numerical realization using the Q-matrix formalism. This part follows closely the seminal publications of Potthoff et al. (59; 60; 61; 62). That followed, we present in section 3.2 our new approach to two-particle, i.e. the magnetic, excitations, which is the basic technical development of the present work. We extend the original idea of the VCA, which is to extrapolate cluster results to the infinite lattice, to the treatment of two-particle excitations. In our novel approach, the two-particle vertex extracted from the corresponding cluster susceptibilities is used to obtain the susceptibilities in the infinite-lattice limit. Hence, the whole approach is controlled by the cluster size and the two-particle as well as the one-particle quantities become exact in the limit of infinite cluster sizes. In addition, section 3.3 deals with an approximation to the Raman response function. We present an approach similar to the magnetic case but without vertex corrections as the k-dependence of the Raman vertex leads to a more complicated numerical treatment. This chapter closes with the introduction of our method of choice to solve the cluster problem. We explain the (Block-)Lanczos algorithm following the corresponding book chapter of Freund (63).

The VCA was recently applied to calculate the zero-temperature ($T = 0$) phase diagram as well as one-particle excitations (61; 64; 65; 66; 67; 68; 69) of the one-band Hubbard model for the appropriate strongly correlated regime ($U = 8t$). These results successfully reproduced salient experimental features such as the electron-hole asymmetry in the doping dependence of antiferromagnetic and superconducting phases (65; 66; 67; 68; 69) in the HTSC materials.

Also the VCA one-particle excitations were found to reproduce characteristic features observed in ARPES experiments such as the much-discussed presence of a gap dichotomy of the nodal and antinodal superconducting gaps (3). Reviewed briefly, these one-particle data obtained with the VCA are related to the new two-particle results of our parameter-free calculation for the underdoped one-band Hubbard model in chapter 4 and 5.

The essential new points in this thesis are that our non-perturbative theory for two-particle excitations (e.g. the dynamic spin-susceptibility) is (i) parameter-free (given fixed, widely-accepted values for the one-band Hubbard model parameters) and (ii) is working in the relevant strong correlation regime of the underlying one-band Hubbard model.

Within this theory we present in chapter 4 a systematic analysis of the magnetic correlations in the hole-doped regime that captures salient features measured in INS experiments. As one of the most salient outcome the celebrated resonance with its *hourglass*-like dispersion structure is obtained for the first time in a parameter-free strongly correlated microscopic calculation. It is verified to be a spin $S=1$ excitonic bound state, which appears in the superconductivity-induced gap in the spectrum of electron-hole spin-flip (i.e. $S=1$) excitations. This will be detailed in our results, where we find the doping dependence of $\omega_{\text{res}}(\mathbf{q}_{AF})$, the energy-integrated spectral weight evaluated at \mathbf{q}_{AF} and the difference of the magnetic susceptibilities in the superconducting and the normal states to be in qualitative accord with INS data for underdoped YBCO, where the mode was studied in great detail (34; 35; 36; 37; 38; 39). In contrast, previous descriptions of the magnetic resonance have been obtained by weak-coupling (70) and/or semi-phenomenological approaches (71; 72; 73; 74; 75; 76) reproducing the experimental behavior with adjustable parameters.

The infinite-lattice limit is crucial to obtain the magnetic resonance which may be considered as a *fingerprint* of the antiferromagnetic order in the superconducting state. Only then are we able to differentiate between the competing antiferromagnetic and superconducting orders in the phase diagram. Therefore, this limit is also embedded in our controlled description of the corresponding susceptibilities.

In case of the Raman response our data presented in chapter 5 reveal the prominent dichotomy of nodal and antinodal superconducting gaps observed in Raman (77; 78) and ARPES (79; 80; 81) experiments. In addition, we address the question of an origin of the gap in the superconducting phase apart from superconductivity. Our findings can be reconciled with the found gap results extracted from the VCA spectral function (3)

Combined with the earlier one-particle calculations, our new results for two-particle excitations presented in chapter 4 and 5 provide a consistent picture, which lends substantial support to Hubbard-model descriptions of high- T_c cuprate superconductivity.

At last, in chapter 6 a short summary of the present thesis is provided.

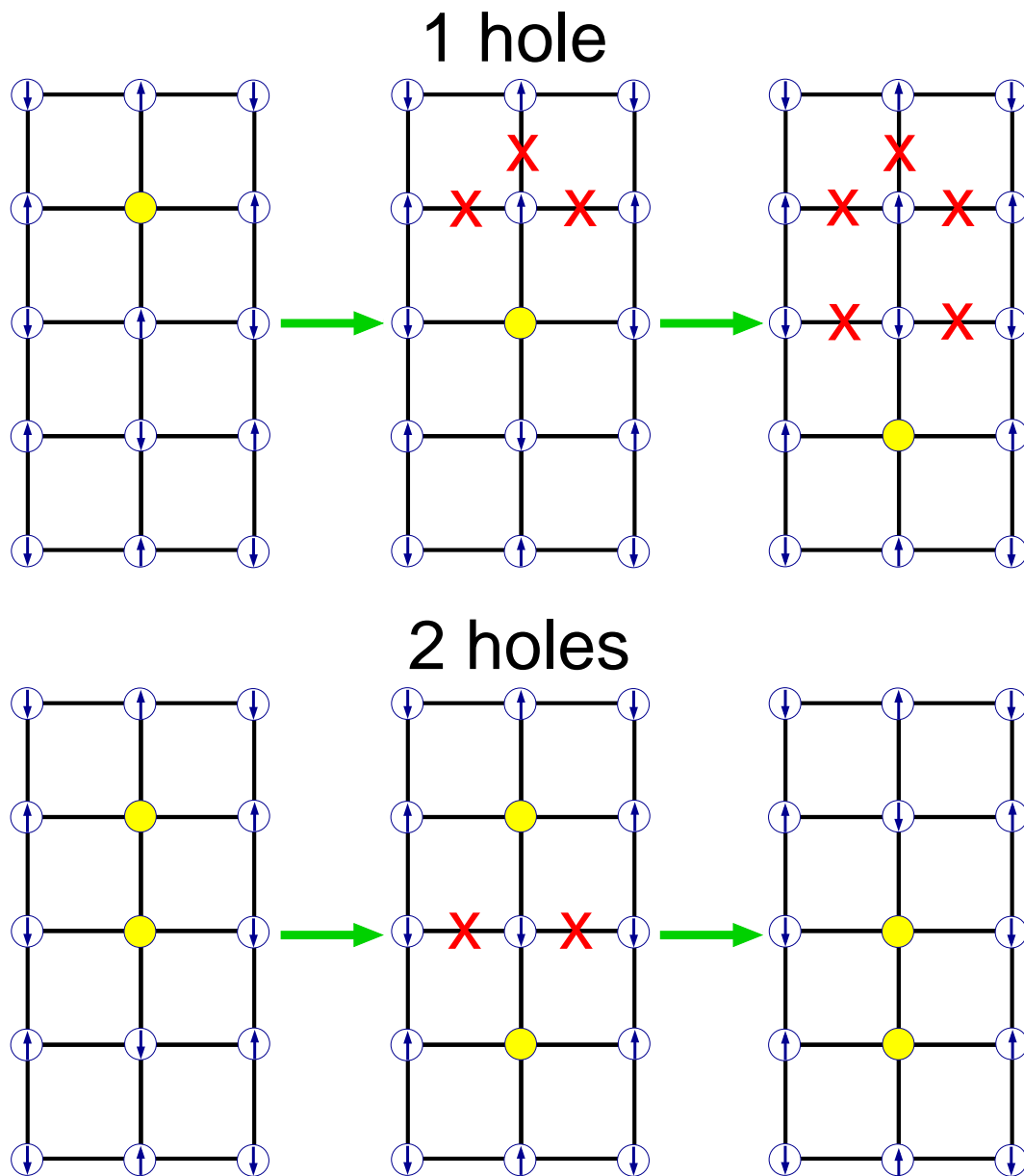


Figure 1.5: Schematic visualization of the instantaneous pairing mechanism within a quadratic lattice in the antiferromagnetic phase.

2

Physical models

The derivation of an appropriate mathematical model is a crucial task for the theoretical investigation in condensed matter physics. On the one hand the model should be as easy as possible but on the other hand it has to contain the relevant physical mechanisms of the considered material. Therefore, according to a prominent statement from A. Einstein the following imperative can be formulated:

Create your model as easy as possible but not easier

We want to describe the properties of cuprate superconductors whose chemical structure is, in principle, described in chapter 1 using the example of LSCO and YBCO. We already stated that the relevant physical processes of cuprates are believed to happen in the CuO_2 planes with a strong electron-electron Coulomb interaction competing with the kinetic energy. Furthermore, we ruled out phonons as important excitations for the physical properties. This leads to the following assumptions for an appropriate model:

- The dynamics of the atoms take place on a much larger time scale compared to the electrons \Rightarrow we can restrict to a pure electronic model.
- All relevant spin and charge degrees of freedom are in the CuO_2 planes \Rightarrow we can restrict to a two-dimensional model on a square lattice. Due to the Mermin-Wagner theorem (82) long-range order can only be established in the ground state at $T = 0$ in less than three dimensions. Nevertheless, in numerical calculations at finite temperatures the correlation length can approach the system size wherefore the system appears to be long-range ordered.
- The dominating interaction between the electrons is a short-range repulsive Coulomb interaction \Rightarrow we can restrict to a local or at least nearest neighbor Coulomb interaction.

Following the seminal publication (57) we introduce the so-called three-band Hubbard model which maps the relevant orbitals within the CuO_2 planes: the $3d_{x^2-y^2}$ orbitals of the copper

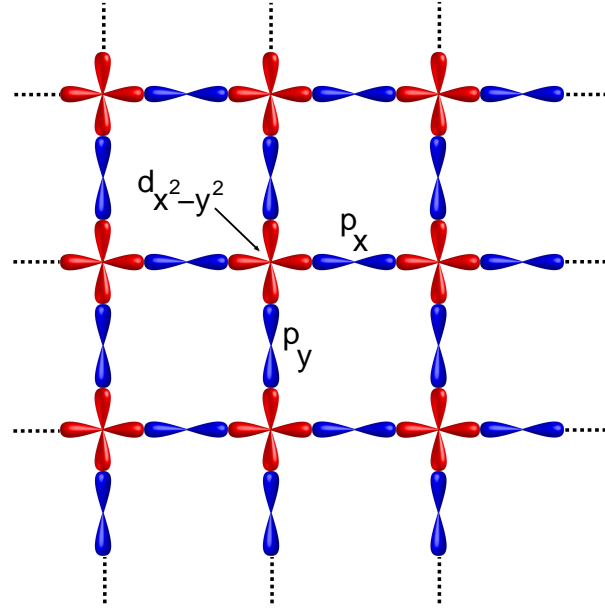


Figure 2.1: Sketch of the three-band model for the CuO_2 planes in the cuprates.

atoms and the $2p_x$ and $2p_y$ orbitals of the oxygen atoms (see Fig. 2.1).

But first we will define the electronic operators used in the following models. $c_{i\sigma}$ annihilates and $c_{i\sigma}^\dagger = (c_{i\sigma})^\dagger$ creates an electron with the spin σ at the site i . These operators obey the fermionic anticommutation relations:

$$[c_{i\sigma}^\dagger, c_{i'\sigma'}^\dagger]_+ = [c_{i\sigma}, c_{i'\sigma'}]_+ = 0 \quad ; \quad [c_{i\sigma}, c_{i'\sigma'}^\dagger]_+ = \delta_{i,i'}\delta_{\sigma,\sigma'} \quad (2.1)$$

2.1 Three-band Hubbard model

The three-band Hubbard model (57) contains hopping of electrons between the oxygen $2p_x$ - and $2p_y$ -orbitals (t^{pp}) as well as a hopping between the copper $3d_{x^2-y^2}$ - and the oxygen $2p$ -orbitals (t^{pd}). Furthermore, the hamiltonian includes a local Coulomb interaction U^p and U^d and a Coulomb interaction between adjacent oxygen $2p$ - and copper d -orbitals U^{pd} . Finally the different energy levels of the oxygen $2p$ - and copper d -orbitals are taken into account via the on-site energies ϵ^p and ϵ^d . Thus, the hamiltonian reads:

$$H_{Hubb3} = - \sum_{\langle j,j' \rangle, \sigma} t_{jj'}^{pp} (c_{j\sigma}^\dagger c_{j'\sigma} + h.c.) - \sum_{\langle i,j \rangle, \sigma} t_{ij}^{pd} (c_{i\sigma}^\dagger c_{j\sigma} + h.c.) \quad (2.2)$$

$$+ U^p \sum_j n_{j\uparrow} n_{j\downarrow} + U^d \sum_i n_{i\uparrow} n_{i\downarrow} + U^{pd} \sum_{\langle i,j \rangle} n_i n_j + \epsilon^p \sum_j n_j + \epsilon^d \sum_i n_i .$$

The indices i and j refer to sublattice of copper d - and oxygen p -orbitals, respectively. $n_{i\sigma} = c_{i\sigma}^\dagger c_{i\sigma}$ ($n_{j\sigma} = c_{j\sigma}^\dagger c_{j\sigma}$) is the number of electrons with spin σ at the site i (j) while

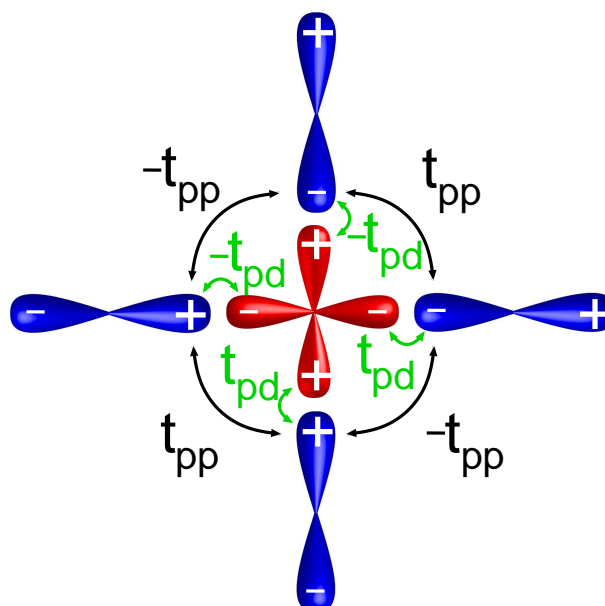


Figure 2.2: Phase convention for the hopping matrix elements of the three-band Hubbard model.

$n_i = n_{i\uparrow} + n_{i\downarrow}$ ($n_j = n_{j\uparrow} + n_{j\downarrow}$). $\langle \dots \rangle$ denotes the summation over nearest neighbors. Due to the symmetry properties of the orbitals a phase convention for the hopping matrix elements has to be introduced (see Fig. 2.2). For a recent VCA study of the three-band model see (83).

2.2 One-band Hubbard model

This section deals with the model we will use for our calculations presented in this thesis. In chapter 1 we analyzed the electronic configuration of the copper and oxygen atoms within the CuO_2 planes and found at zero doping $[3d^9]$ for the first and $[2p^6]$ for the latter one. That means, without doping each oxygen orbital is fully occupied while the $3d_{x^2-y^2}$ copper orbital contains one hole in the d-orbitals on an average. It was shown (84) that in the strong coupling limit it is favorable for doped holes to go into the oxygen p-orbitals and form the famous Zhang-Rice singlet with the hole at the copper d-orbital. Furthermore, on the basis of this Zhang-Rice singlet an effective low-energy one-band model was derived in (84). Therefore, we will consider as a simplification only one hybridized $3d_{x^2-y^2} - 2p_x - 2p_y$ -orbital located at each copper site. The oxygen orbitals will be neglected except for providing the orbitals for the hybridization. This effective model is called one-band Hubbard model which was previously introduced to describe the magnetism of itinerant electrons in narrow bands (58). It contains a local Coulomb interaction U and an hopping between the lattice sites. In our case, we consider nearest (t) and next-nearest (t') neighbor hopping. Although this model appears very simple, an exact solution only exists in one dimension through the Bethe ansatz (85). The

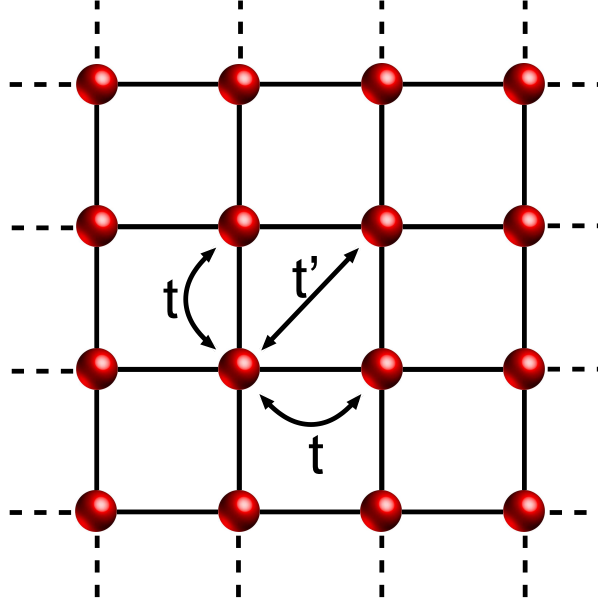


Figure 2.3: Sketch of the one-band model for the CuO_2 planes in the cuprates with nearest and next-nearest neighbor hopping.

hamiltonian in the grand canonical form reads:

$$\begin{aligned} \mathcal{H}_{Hubb1} = H_{Hubb1} - \mu \sum_i n_i &= -t \sum_{\langle i,j \rangle, \sigma} (c_{i\sigma}^\dagger c_{j\sigma} + h.c.) - t' \sum_{\langle\langle i,j \rangle\rangle, \sigma} (c_{i\sigma}^\dagger c_{j\sigma} + h.c.) \\ &\quad - \mu \sum_i n_i + U \sum_i n_{i\uparrow} n_{i\downarrow}, \end{aligned} \quad (2.3)$$

with $\langle\langle \dots \rangle\rangle$ denoting the summation over next-nearest neighbors. Fig. 2.3 gives a sketch of the effective one-band model with nearest and next-nearest neighbor hopping.

As the one-band Hubbard model is our model of choice for the description of the cuprate superconductors we will leave the attribute one-band in the further thesis for simplicity. Next, we review some general symmetries and limits of the Hubbard model.

2.2.1 Conserving quantities

It is straightforward to prove the Hubbard hamiltonian symmetric under $U(1)$ and $SU(2)$ transformations which leads to a conserving of the particle number $N_\sigma = \sum_i n_{i\sigma}$, the squared total spin $(\mathbf{S})^2 = (\sum_i \mathbf{S}_i)^2$ and the z-component of the total spin $S^z = \sum_i S_i^z = \frac{1}{2} \sum_i (n_{i\uparrow} - n_{i\downarrow})$.

$$[H_{Hubb1}, N_\sigma]_- = [H_{Hubb1}, (\mathbf{S})^2]_- = [H_{Hubb1}, S^z]_- = 0 \quad (2.4)$$

2.2.2 Particle-hole-transformation

A hypercubic lattice, such as we will use for the cuprates, belongs to the class of bipartite lattices. These lattices can be constructed by two sublattices A and B with each site of sublattice A having only sites of B as nearest neighbors and vice versa. Considering such a bipartite lattice we perform a particle-hole transformation defined as:

$$c_{i\sigma} \rightarrow c_{i\sigma}^\dagger \quad ; \quad c_{i\sigma}^\dagger \rightarrow \eta_i c_{i\sigma} \quad , \quad (2.5)$$

with $\eta_i = 1$ at the sites of A and $\eta_i = -1$ at the sites of B. Application to the hamiltonian in Eq. 2.3 yields

$$\begin{aligned} \mathcal{H}_{Hubb1}^{ph} = & -t \sum_{\langle i,j \rangle, \sigma} (c_{i\sigma}^\dagger c_{j\sigma} + h.c.) + t' \sum_{\langle\langle i,j \rangle\rangle, \sigma} (c_{i\sigma}^\dagger c_{j\sigma} + h.c.) \\ & - (U - \mu) \sum_i n_i + U \sum_i n_{i\uparrow} n_{i\downarrow} + (U - 2\mu)N \quad , \end{aligned} \quad (2.6)$$

with N the number of lattice sites. We realize that the Hubbard model is particle-hole symmetric for $t' = 0$ at $\mu = \frac{U}{2}$.

2.2.3 $U = 0$ limit

In the limit of a vanishing interaction the Hubbard model can be solved straightforwardly by a Fourier transformation

$$c_{i\sigma} = \frac{1}{\sqrt{N}} \sum_{\mathbf{k}} c_{\mathbf{k}\sigma} e^{i\mathbf{k}r_i} \quad ; \quad c_{i\sigma}^\dagger = \frac{1}{\sqrt{N}} \sum_{\mathbf{k}} c_{\mathbf{k}\sigma}^\dagger e^{-i\mathbf{k}r_i} \quad . \quad (2.7)$$

Inserting in Eq. 2.3 yields in two dimensions

$$\mathcal{H}_{Hubb1} = \sum_{\mathbf{k}, \sigma} c_{\mathbf{k}\sigma}^\dagger c_{\mathbf{k}\sigma} (\epsilon(\mathbf{k}) - \mu) \quad (2.8)$$

$$\epsilon(\mathbf{k}) = -2t(\cos(k_x) + \cos(k_y)) - 2t'(\cos(k_x + k_y) + \cos(k_x - k_y)) \quad . \quad (2.9)$$

2.2.4 Large U limit

In the limit of a strong local repulsion U double occupancy is impeded. Applying second order perturbation theory in $\frac{1}{U}$ renders in case of only nearest-neighbor hopping and a filling $n \leq 1$ the prominent $t - J$ model

$$H_{tJ} = -t \sum_{\langle i,j \rangle, \sigma} (\tilde{c}_{i\sigma}^\dagger \tilde{c}_{j\sigma} + h.c.) + J \sum_{\langle i,j \rangle} \left(\mathbf{S}_i \mathbf{S}_j - \frac{1}{4} n_i n_j \right) \quad , \quad (2.10)$$

with $J = \frac{4t^2}{U}$ and the modified one-particle operators omitting double occupancy $\tilde{c}_{i\sigma} = c_{i\sigma}(1 - n_{i-\sigma})$, $\tilde{c}_{i\sigma}^\dagger = c_{i\sigma}^\dagger(1 - n_{i-\sigma})$. The spin- $\frac{1}{2}$ operators \mathbf{S}_i are defined in section 3.2.2.

At half-filling the $t - J$ model simplifies to the Heisenberg model

$$H_H = J \sum_{\langle i,j \rangle} \left(\mathbf{s}_i \mathbf{s}_j - \frac{1}{4} \right) . \quad (2.11)$$

We discover that the Hubbard model in the strong coupling limit describes at half-filling an insulator with an antiferromagnetic spin interaction.

3

Techniques

We are interested in the equilibrium dynamics of elementary one- and two-particle excitations of a system of strongly-correlated electrons. These dynamics are described by the Green's function which we will define in the Matsubara formalism (86; 87; 88; 89)

$$\begin{aligned} G_{\alpha\beta}(i\omega) = \langle\langle A_\alpha; B_\beta \rangle\rangle_{i\omega} &= \frac{1}{2} \int_{-\infty}^{\infty} d\tau G_{\alpha\beta}(\tau) e^{i\omega\tau} \\ &= -\frac{1}{2} \int_{-\infty}^{\infty} d\tau \langle T_\tau \{ A_\alpha(\tau) B_\beta(0) \} \rangle e^{i\omega\tau}, \end{aligned} \quad (3.1)$$

with the imaginary time Heisenberg representation $A(\tau) = e^{H\tau} A e^{-H\tau}$, $\tau = it$ and T_τ denoting the time-ordering operator. In case of the fermionic one-particle Green's function the A and B are fermionic creation and annihilation operators and $i\omega_n^f = i(2n+1)\pi T$; $n \in \mathbb{Z}$ are fermionic Matsubara frequencies, while for the two-particle analogon each of the two operators (A, B) consists of two fermionic operators and $i\omega_n^b = i2n\pi T$; $n \in \mathbb{Z}$ are bosonic Matsubara frequencies. However, a perturbatively calculation of a Green's function of a strongly-correlated system fails as the interaction strength is comparable to the bandwidth and no small parameter exists. Many numerical methods have been invented to attack the strong correlated many-body problem. Most of them became essentially exact in some cases. For limited system sizes this holds for the Quantum Monte Carlo (QMC) method (90) and the Exact Diagonalization (ED), while the Density-Matrix Renormalization-Group (DMRG) (91; 92) works best in one dimension. In case of infinite dimensions the Dynamical Mean-Field Theory (DMFT) (93) becomes exact also for the thermodynamic limit on infinite systems. However the DMFT is for low-dimensional system only an approximation as no spatial correlations are considered. Improvements can be obtained by cluster extensions (94). These extensions incorporate short-range spatial correlations by solving a small cluster exactly. There are existing two realizations, a real-space construction called Cellular-DMFT (C-DMFT) (95; 96; 97; 98) and a reciprocal-space construction called Dynamical Cluster Approximation (DCA) (99). Both methods are improvements in low dimensions but they are no longer exact in the limit of infinite dimensions.

In the following chapter we introduce a technique to calculate the one-particle Green's function for infinite sized systems which also considers spatial correlations via the exact solution of a finite cluster. The dynamic quantity obtained from the cluster calculation is the electronic self-energy Σ . Therefore, this technique called Variational Cluster Approach (VCA) (61) is closely related to the Cluster Perturbation Theory (CPT) (100; 101; 102). As an improvement compared to the CPT the VCA combines a cluster technique with a variational principle which allows for symmetry broken phases. Thus, the VCA combines short-range correlations and long-range order phenomena. Noteworthy, it turns out, that the CPT as well as the C-DMFT can be derived as special cases of the VCA, wherefore the VCA can be considered as a more general principle (62) (for an explanation of these three techniques see also (103)).

As the present thesis focuses on two-particle excitations of strongly-correlated systems, we derive an extension to the VCA for two-particle correlation functions which will contain no free adjustable parameters. Guided by the spirit of the VCA we define an effective two-particle vertex obtained at the cluster level. This ensures that the approach is controlled by the cluster size, which means, that the one-particle as well as the two-particle correlation functions become exact in the limit of infinite cluster sizes. In case of the Raman response the treatment of the vertex function is more complicated and we use the effective mass approximation for the bare Raman vertex. The subsequent chapter will show that the derived technique enables us to calculate salient two-particle properties of strongly-correlated high-temperature superconductors without adjustable free parameters for the first time.

This chapter closes with the explanation of the ED which is our method of choice for solving the finite cluster in the $T = 0$ limit.

3.1 Variational Cluster Approach (VCA)

The VCA (61) is based on the Self-Energy-Functional Approach (SFA) (59; 60). Here, the grand potential Ω can be expressed as functional of the self-energy of the system. The stationary point of this functional yields the physical self-energy at which also the grand potential becomes physical. In case of not exactly solvable systems, the stationarity condition also provides a powerful method to find the best approximated self-energy in a certain subspace of trial self-energies.

3.1.1 Self-Energy-Functional Approach

We consider a system of electrons on an infinite lattice at the temperature T and the chemical potential μ with the hamiltonian

$$H = H_0(\mathbf{t}) + H_1(\mathbf{U}) . \quad (3.2)$$

The H_0 contains all one-particle terms depending on the parameters \mathbf{t}

$$H_0 = \sum_{\alpha,\beta} t_{\alpha\beta} c_{\alpha}^{\dagger} c_{\beta} , \quad (3.3)$$

$$\Phi[\mathbf{G}] = \text{diagram 1} + \text{diagram 2} + \text{diagram 3} + \dots$$

Figure 3.1: Diagrammatical definition of the Luttinger-Ward functional with double lines depicting the fully interacting Green's function while the dashed lines symbolize the interaction.

while H_1 is the interaction part depending on U

$$H_1 = \frac{1}{2} \sum_{\alpha, \beta, \gamma, \delta} U_{\alpha\beta\gamma\delta} c_{\alpha}^{\dagger} c_{\beta}^{\dagger} c_{\delta} c_{\gamma} . \quad (3.4)$$

The $\alpha\beta\gamma\delta$ refer to a complete and orthonormal set of one-particle basis states. By use of the Dyson equation, the one-particle Green's function $G_{\alpha\beta} = G_{\alpha\beta}(i\omega_n^f) = \langle\langle c_{\alpha}; c_{\beta}^{\dagger} \rangle\rangle_{i\omega_n^f}$ can be calculated as follows:

$$\mathbf{G} = \mathbf{G}_0 + \mathbf{G}_0 \Sigma \mathbf{G} , \quad (3.5)$$

where $\mathbf{G}_0 = \mathbf{G}_0(i\omega_n^f) = (i\omega_n^f + \mu - \mathbf{t})^{-1}$ is the non-interacting Green's function and $\Sigma_{\alpha\beta} = \Sigma_{\alpha\beta}(i\omega_n^f)$ the electronic irreducible self-energy, which can be obtained by the functional derivation of the so-called Luttinger-Ward functional $\Phi[\mathbf{G}]$ (104)

$$\Sigma = \Sigma[\mathbf{G}] = T^{-1} \frac{\delta \Phi[\mathbf{G}]}{\delta \mathbf{G}} . \quad (3.6)$$

In their original work Luttinger and Ward constructed the functional $\Phi[\mathbf{G}]$ diagrammatically for the weak-coupling case and found it to be given by an infinite series of closed skeleton diagrams (Fig. 3.1). As no self-energy insertions are in the series of diagrams the functional depends only on the fully interacting Green's function (dressed one-particle propagators) and the bare interaction. With $\Phi[\mathbf{G}]$ showing no explicit dependence on one-particle terms \mathbf{t} such as the hopping, two systems with different one-particle terms but the same interaction are described by the same universal Luttinger-Ward functional. To avoid the weak-coupling diagrammatic series Potthoff provided a non-perturbative construction of $\Phi[\mathbf{G}]$ and proved the universality explained above to be still valid (105).

The grand potential Ω of the considered system is given by the following self-energy functional evaluated at its stationary point

$$\Omega_{\mathbf{t}}[\Sigma] = Tr \ln \left(- (\mathbf{G}_0^{-1} - \Sigma)^{-1} \right) + F[\Sigma] , \quad (3.7)$$

with $F[\Sigma] = \Phi[\mathbf{G}[\Sigma]] - Tr(\Sigma \mathbf{G}[\Sigma])$ the Legendre transform of $\Phi[\mathbf{G}]$ and $\mathbf{G}[\Sigma]$ the inverse of $\Sigma[\mathbf{G}]$ (see (59) for details). The subscript \mathbf{t} indicates the explicit \mathbf{t} dependence of the

grand potential due to \mathbf{G}_0 . Note, that the trace appearing in the equation is defined as $Tr\mathbf{O} = T \sum_{\omega, \alpha} O_{\alpha\alpha}(i\omega)$. The above functional becomes stationary at the exact self-energy of the system:

$$\frac{\delta\Omega_t[\boldsymbol{\Sigma}]}{\delta\boldsymbol{\Sigma}} = 0 \iff \mathbf{G}[\boldsymbol{\Sigma}] = (\mathbf{G}_0^{-1} - \boldsymbol{\Sigma})^{-1} . \quad (3.8)$$

However, the self-energy functional $\Omega_t[\boldsymbol{\Sigma}]$ is not known explicitly.

Next, we define a so-called reference-system, which is described by a hamiltonian similar to Eq. (3.2)

$$H' = H_0(\mathbf{t}') + H_1(\mathbf{U}) , \quad (3.9)$$

but with a different one-particle operator

$$H_0 = \sum_{\alpha, \beta} t'_{\alpha\beta} c_{\alpha}^{\dagger} c_{\beta} . \quad (3.10)$$

As the steps explained above are also valid for this reference-system we derive a similar expression for the grand potential

$$\Omega_{\mathbf{t}'}[\boldsymbol{\Sigma}] = Tr \ln \left(- \left(\mathbf{G}'_0^{-1} - \boldsymbol{\Sigma} \right)^{-1} \right) + F[\boldsymbol{\Sigma}] , \quad (3.11)$$

with $\mathbf{G}'_0 = \mathbf{G}'_0(i\omega_n^f) = (i\omega_n^f + \mu - \mathbf{t}')^{-1}$. Note, that Eq. (3.7) as well as Eq. (3.11) contains $F[\boldsymbol{\Sigma}]$. This is a universal functional of the self-energy with a functional dependence that is the same for any \mathbf{t} and therefore also for \mathbf{t}' . That very important fact will be used to eliminate the $F[\boldsymbol{\Sigma}]$ by a subtraction of the equations (3.7) and (3.11)

$$\Omega_{\mathbf{t}}[\boldsymbol{\Sigma}] = \Omega_{\mathbf{t}'}[\boldsymbol{\Sigma}] + Tr \ln \left(- \left(\mathbf{G}_0^{-1} - \boldsymbol{\Sigma} \right)^{-1} \right) - Tr \ln \left(- \left(\mathbf{G}'_0^{-1} - \boldsymbol{\Sigma} \right)^{-1} \right) . \quad (3.12)$$

So far we made no approximation and all equations are still exact, but as the original hamiltonian is not exactly solvable, the physical self-energy is also not accessible.

Next, we make the essential assumption, that the reference-system is simple enough to be solved. This provides a certain space of trial self-energies $\boldsymbol{\Sigma}(\mathbf{t}')$ parameterized by \mathbf{t}' . The evaluation of Eq. (3.12) at these trial self-energies yields

$$\begin{aligned} \Omega_{\mathbf{t}}[\boldsymbol{\Sigma}(\mathbf{t}')] &= \Omega_{\mathbf{t}'}[\boldsymbol{\Sigma}(\mathbf{t}')] + Tr \ln \left(- \left(\mathbf{G}_0^{-1} - \boldsymbol{\Sigma}(\mathbf{t}') \right)^{-1} \right) \\ &\quad - Tr \ln \left(- \left(\mathbf{G}'_0^{-1} - \boldsymbol{\Sigma}(\mathbf{t}') \right)^{-1} \right) \\ &= \Omega' + Tr \ln \left(- \left(\mathbf{G}_0^{-1} - \boldsymbol{\Sigma}(\mathbf{t}') \right)^{-1} \right) - Tr \ln (-\mathbf{G}') . \end{aligned} \quad (3.13)$$

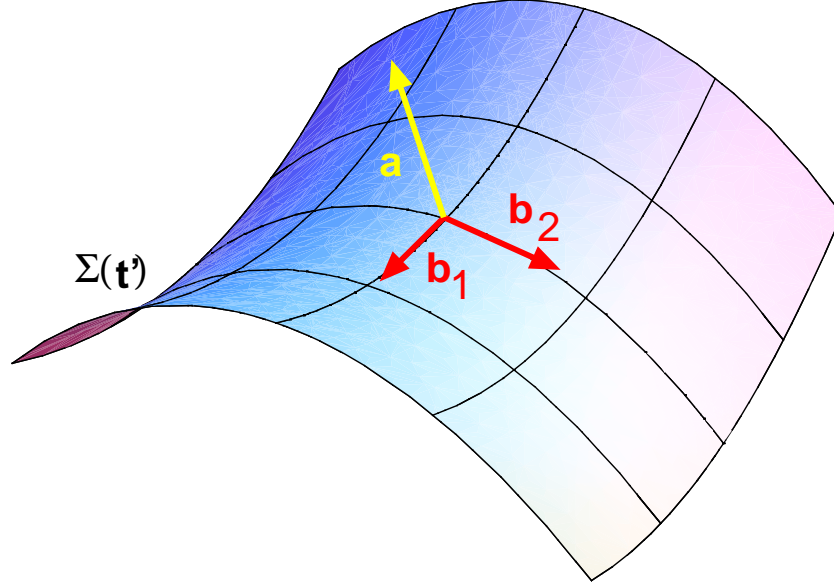


Figure 3.2: Sketch of the approximated stationarity condition in case of two variational parameters. The vector \mathbf{a} indicates the non-vanishing bracket in Eq. (3.14) and is perpendicular to the tangential vectors \mathbf{b}_1 and \mathbf{b}_2 of the \mathbf{t}' parameterized hypersurface.

By applying the Euler equation $\delta\Omega_t[\Sigma(\mathbf{t}')] / \delta\mathbf{t}' = 0$ to the last expression, we obtain as a very important result

$$T \sum_{\omega} \sum_{\alpha, \beta} \left((\mathbf{G}_0^{-1} - \Sigma(\mathbf{t}'))^{-1} - \mathbf{G}' \right)_{\beta\alpha} \frac{\delta\Sigma_{\alpha\beta}(\mathbf{t}')}{\delta\mathbf{t}'} = 0. \quad (3.14)$$

Only the non-interacting Green's function has to be calculated within the original system. The problem of finding the exact self-energy is approximated by the reduction of the space of trial self-energies to a hypersurface parameterized by \mathbf{t}' . If the exact one is captured by this hypersurface, the bracket in Eq. (3.14) will be zero at the exact self-energy. It is a precious fact, that Eq. (3.14) also holds for trial self-energies not containing the exact one. In this case the bracket will not become zero, but as the derivative in Eq. (3.14) defines a tangential vector to the \mathbf{t}' parameterized hypersurface, Eq. (3.14) can be interpreted as the projection of the exact stationarity condition onto this hypersurface. Therefore, even for not exact trial self-energies Eq. (3.14) can be fulfilled due to an orthogonality of the non-vanishing bracket to the hypersurface (see the sketch in Fig. 3.2). Although the found self-energy is not exact in this case, it is the best approximated one which is covered by the hypersurface of trial self-energies. Therefore we will call the stationarity condition in this case an approximated

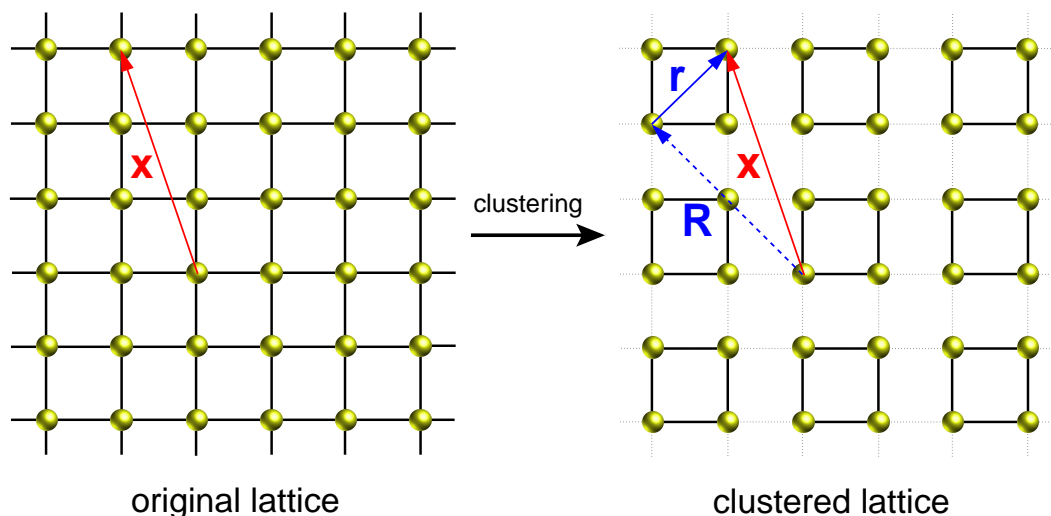


Figure 3.3: Tiling up the original real space lattice into N_c finite clusters with L_c sites each. This lattice is called superlattice with the cluster being the elementary cell.

stationarity condition. We mention that the SFA can be shown to be causal (see (60) for a detailed proof). It is noteworthy, that a found stationary point is not an extremum in general and that more than only a single point may be found. In practice, they are mostly saddle points and in case of more than one of these points the physical self-energy is the one which diminishes the grand potential. However, there are some exceptions from the latter rule. Stationary points which can not be reconciled with the overall phased diagram or which lead to huge discrepancies between the physical and the reference system have to be neglected in some cases.

3.1.2 Derivation of the Variational Cluster Approach (VCA)

On the general basis of the SFA we intent to explain the derivation of a non-perturbative approach to Green's functions of fermionic lattice systems. This approach will be determined by a proper choice of the reference system, which must obey the condition to be solvable. For this reason we tile up the infinite lattice into N_c finite clusters with L_c sites each (see Fig. 3.3). The total number of sites is $N = N_c \times L_c$. As the original lattice is in principle infinite ($N \rightarrow \infty$) the number of cluster will also be infinite $N_c \rightarrow \infty$. Assuming the interaction to be local, which is a proper choice as we aim at the Hubbard model for explicit calculations, allows for a splitting of the hamiltonian into an intracluster and intercluster part:

$$H = \sum_a \left[H_0^{(\text{intra})}(\mathbf{R}_a) + H_1(\mathbf{R}_a) \right] + \sum_{a,b} H_0^{(\text{inter})}(\mathbf{R}_a, \mathbf{R}_b) , \quad (3.15)$$

with the intracluster one-particle part

$$H_0^{(\text{intra})}(\mathbf{R}_a) = \sum_{i,j,\sigma} t_{ij} c_{ai\sigma}^\dagger c_{aj\sigma} , \quad (3.16)$$

an arbitrary local interaction part H_1 and the intercluster one-particle part

$$H_0^{(\text{inter})}(\mathbf{R}_a, \mathbf{R}_b) = \sum_{i,j,\sigma} V_{(ai)(bj)} c_{ai\sigma}^\dagger c_{bj\sigma} . \quad (3.17)$$

The latter part connects different clusters with each cluster labeled by it's reference point \mathbf{R} . Therefore the intercluster hopping obeys the constraint $V_{(ai)(aj)} = 0$. While the translational invariance of the original system is broken on the cluster level due to open boundary conditions on a single cluster, we assume the invariance of the intercluster part under translation with respect to the superlattice vector \mathbf{R} . Note, that the open boundary conditions are not a requirement but an intrinsic characteristic of the approximation, which will be discussed later in this section and also in section 3.1.3.

For the next step towards the VCA we introduce a transformation under which the hamiltonian Eq. (3.15) remains invariant

$$\begin{aligned} H_0^{(\text{intra})}(\mathbf{R}_a) &\rightarrow H_0^{(\text{intra})}(\mathbf{R}_a) + \Delta(\mathbf{R}_a) \\ H_0^{(\text{inter})}(\mathbf{R}_a, \mathbf{R}_b) &\rightarrow H_0^{(\text{inter})}(\mathbf{R}_a, \mathbf{R}_b) - \delta_{a,b} \Delta(\mathbf{R}_a) , \end{aligned} \quad (3.18)$$

with an arbitrary one-particle operator $\Delta(\mathbf{R}_a) = \sum_{i,j,\sigma,\sigma'} \{ \Delta_{ij}^{n,\sigma\sigma'} c_{ai\sigma}^\dagger c_{aj\sigma'} + \Delta_{ij}^{sc,\sigma\sigma'} (c_{ai\sigma} c_{aj\sigma'} + h.c.) \}$. The first part of these one-particle operator accounts for all normal fields while the latter one covers all superconducting fields. For simplicity, we reduce the notation $\Delta_{ij}^{n/sc,\sigma\sigma'}$ in the following to Δ_{ij} . So far we did no approximation and the original hamiltonian remains unchanged. For a solvable reference system which provides the trial self-energies for the SFA, we neglect the intercluster part of the hamiltonian

$$H' = \sum_a \left[H_0^{(\text{intra})}(\mathbf{R}_a) + \Delta(\mathbf{R}_a) + H_1(\mathbf{R}_a) \right] . \quad (3.19)$$

Due to the clustering we use open boundary conditions, but in principal also periodic boundary conditions could be used. The proof that our choice is the correct one we introduce an additional hopping between the edge sites of the cluster with the parameter t_r . As the hopping operator is a one-particle operator we can apply the Euler equation to find the t_r for which the self-energy is approximated best. Indeed, it turns out that the VCA yields $t_r = 0$ as a result (61). Thus, in contrast to the CPT the VCA answers the question of a proper choice of boundary condition by itself.

As we require this reference system to be solvable, we can extract the self-energy from the Dyson equation for the reference system Eq. (3.5)

$$\Sigma(\mathbf{t}') = \mathbf{G}'_0{}^{-1} - \mathbf{G}'^{-1} . \quad (3.20)$$

In principal, we are now able to use Eq. (3.14) for finding the stationary points. The task is to calculate the grand potential by use of the exact cluster information and perform the optimization of the cluster self-energy to fulfill $\delta\Omega_t[\Sigma(\mathbf{t}')]/\delta\mathbf{t}' = 0$ in the space of the variational parameters Δ_{ij} . These variational parameter can be understood as an enlargement of the space of trial self-energies. A further improvement could be achieved by implementing the

so-called bath sites in the reference system. These are additional cluster sites where the interaction vanishes. The additional variational parameter is the so-called hybridization function which is the hopping from an correlated to such an uncorrelated site. In this work bath sites would mean too much numerical effort and are therefore not considered.

Systematically, the procedure runs as follows: For a set of variational parameters the self-energy of the reference system has to be calculated via Eq. (3.20) and used to evaluate the grand potential via Eq. 3.13. These steps have to be repeated (of course in an intelligent and purposeful way) until $\delta\Omega_t[\Sigma(\mathbf{t}')] / \delta\mathbf{t}' = 0$.

VCA Green's function

Inserting the optimized self-energy into the Dyson equation for the original system Eq. (3.5) yields the desired VCA Green's function

$$\mathbf{G} = \left(\mathbf{G}_0^{-1} - \mathbf{G}'_0^{-1} + \mathbf{G}'^{-1} \right)^{-1}. \quad (3.21)$$

This expression can be simplified as we know the explicit solutions of the non-interacting Green's functions $\mathbf{G}_0^{-1} = \mathbf{G}_0^{-1}(i\omega_n^f) = (i\omega_n^f + \mu - \mathbf{T})$ and $\mathbf{G}'_0^{-1} = \mathbf{G}'_0^{-1}(i\omega_n^f) = (i\omega_n^f + \mu - \mathbf{T}')$. With N_c the number of clusters (in principle, N_c is infinite, but for practical calculations it is a sufficient large and finite number) and L_c the number of cluster sites, the matrix \mathbf{T}' is defined as $\mathbf{T}' = \mathbb{1}_{N_c \times N_c} \otimes (\mathbf{t} + \Delta)$ with \mathbf{t} the cluster hopping matrix and Δ the arbitrary one-particle fields, both having the dimension $L_c \times L_c$ (see Eq. (3.22)). Therefore \mathbf{T}' has the dimension $(N_c \times L_c) \times (N_c \times L_c)$ and shows a block-diagonal shape with each block being the cluster hopping matrix plus the matrix Δ . \mathbf{T} differs from \mathbf{T}' by the $(N_c \times L_c) \times (N_c \times L_c)$ intercluster hopping matrix \mathbf{V} (see Eq. (3.23)) as well as Δ and therefore reads $\mathbf{T} = \mathbf{T}' + \mathbf{V} - \mathbb{1}_{N_c \times N_c} \otimes \Delta$.

$$\mathbf{T}' = \begin{pmatrix} \boxed{\begin{matrix} \mathbf{t} + \Delta \\ L_c \times L_c \end{matrix}} & & & & 0 \\ & \boxed{\begin{matrix} \mathbf{t} + \Delta \\ L_c \times L_c \end{matrix}} & & & \\ & & * & & \\ & & & * & \\ 0 & & & & * \\ & & & & \boxed{\begin{matrix} \mathbf{t} + \Delta \\ L_c \times L_c \end{matrix}} \end{pmatrix}_{N_c \times N_c} \quad (3.22)$$

$$\mathbf{V} = \begin{pmatrix} 0 & \boxed{\mathbf{V}_{12}} & \boxed{\mathbf{V}_{13}} & * & * & * \\ \boxed{\mathbf{V}_{21}} & 0 & \boxed{\mathbf{V}_{23}} & * & * & * \\ \boxed{\mathbf{V}_{31}} & \boxed{\mathbf{V}_{32}} & * & * & * & * \\ * & * & * & * & * & * \\ * & * & * & * & * & * \\ * & * & * & * & * & * \end{pmatrix}_{N_c \times N_c} \quad (3.23)$$

With these considerations Eq. (3.21) becomes

$$\mathbf{G} = \left(\mathbf{G}'^{-1} - (\mathbf{T} - \mathbf{T}') \right)^{-1} = \left(\mathbf{G}'^{-1} - \mathbf{V} + \mathbb{1}_{N_c \times N_c} \otimes \Delta \right)^{-1}. \quad (3.24)$$

Note, that \mathbf{G}' is the Green's function of the reference system, which has the dimension $(N_c \times L_c) \times (N_c \times L_c)$ like \mathbf{V} and which is of a block-diagonal form with each block the interacting cluster Green's function $\mathbf{G}' = \mathbb{1}_{N_c \times N_c} \otimes \mathbf{G}^c$.

As the superlattice obeys the translational invariance we are allowed to perform a Fourier transformation with respect to the superlattice vector \mathbf{R} induced by the unitary matrix \mathbf{U} : $\mathbf{V}_{\mathbf{k}} = \mathbf{U} \mathbf{V} \mathbf{U}^\dagger$. The matrix $\mathbf{V}_{\mathbf{k}}$ is block-diagonal with each block a \mathbf{k} -dependent $L_c \times L_c$ matrix $\mathbf{V}(\mathbf{k})$. Note, that \mathbf{k} is an element of the reduced Brillouin zone. Inserting this result into Eq. (3.24) yields

$$\begin{aligned} \mathbf{G}(\mathbf{k}) &= \mathbf{U} \mathbf{G} \mathbf{U}^\dagger = \mathbf{U} \left(\mathbb{1}_{N_c \times N_c} * \mathbf{G}^{c-1} - \mathbf{U}^\dagger \mathbf{V}_{\mathbf{k}} \mathbf{U} + \mathbb{1}_{N_c \times N_c} * \Delta \right)^{-1} \mathbf{U}^\dagger \\ &= \mathbf{U} \left(\mathbf{U}^\dagger (\mathbb{1}_{N_c \times N_c} * \mathbf{G}^{c-1}) \mathbf{U}^\dagger - \mathbf{V}_{\mathbf{k}} + \mathbf{U} (\mathbb{1}_{N_c \times N_c} * \Delta) \mathbf{U}^\dagger \right)^{-1} \mathbf{U}^\dagger \\ &= \left(\mathbb{1}_{N_c \times N_c} * \mathbf{G}^{c-1} - \mathbf{V}_{\mathbf{k}} + \mathbb{1}_{N_c \times N_c} * \Delta \right)^{-1}. \end{aligned} \quad (3.25)$$

We used $\mathbf{U}^\dagger \mathbf{U} = \mathbb{1}$ and $\mathbf{U}(\text{const} \otimes \mathbb{1}_{N_c \times N_c}) \mathbf{U}^\dagger = \text{const} \otimes \mathbb{1}_{N_c \times N_c}$. This is a very interesting and important result, as the whole equation Eq. (3.25) is \mathbf{k} -separable and becomes a $L_c \times L_c$ matrix equation which is \mathbf{k} and ω dependent

$$\mathbf{G}(\mathbf{k}, i\omega_n^f) = \left(\mathbf{G}^{c-1}(i\omega_n^f) - \mathbf{V}(\mathbf{k}) + \Delta \right)^{-1}. \quad (3.26)$$

This \mathbf{k} -separability implies that for any practical purpose there is no need to distinguish between the reference system and the cluster Green's function.

The last equation can be understood as follows: We included the additional one-particle fields Δ in the reference system. As the hopping matrix, these fields will enter the Green's function

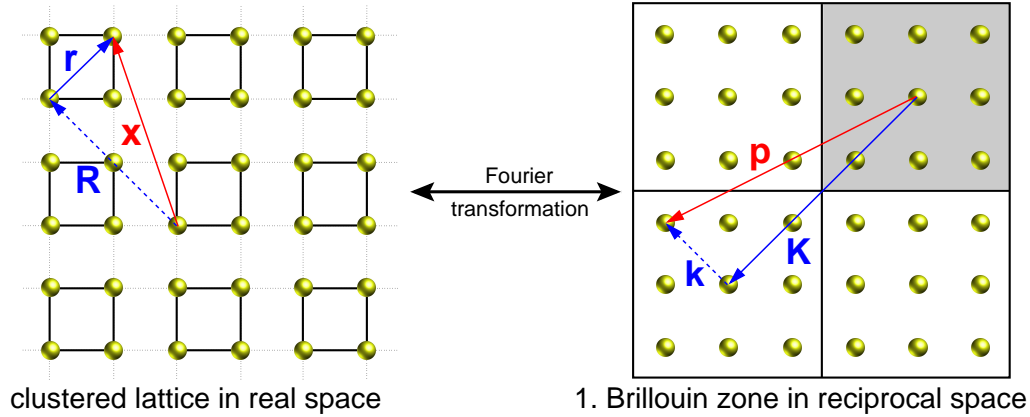


Figure 3.4: The clustered lattice in real space and the corresponding first Brillouin zone in reciprocal space with the shaded area indicating the reduced Brillouin zone. Note, that for an infinite lattice the \mathbf{k} -points become dense.

G^c in the denominator with a minus sign. But the term $+\Delta$ in Eq. (3.26) annihilates this part. Therefore these fields only effect the cluster self-energy also included in the G^c . Without the variational procedure for finding the optimized one-particle parameters the CPT is obtained with the intercluster hopping and Δ as the perturbation. In this sense the VCA can be understood as the CPT combined with a variational principle.

3.1.3 Translational invariance

The VCA Green's function as shown in Eq. (3.26) is given in a mixed representation as beside the wave vector \mathbf{k} it is still a matrix in the cluster indices. However, such a mixed representation is not appropriate for physical quantities, e.g. the spectral function $A(\mathbf{k}, \omega) = \mp \frac{1}{\pi} \text{Im} G_{\text{av}}^{\text{ret}}(\mathbf{k}, \omega)$ (86; 87; 88; 89). This problem stems from the broken translational invariance due to the clustering and is a shortcoming of the VCA itself. To get rid of the mixed representation we inspect the full Fourier transformation of the real-space Green's function

$$G(\mathbf{k}+\mathbf{K}, \mathbf{k}'+\mathbf{K}') = \frac{1}{N_c L_c} \sum_{a,b,i,j} e^{i(\mathbf{k}+\mathbf{K})(\mathbf{R}_a+\mathbf{r}_i)} G(\mathbf{R}_a+\mathbf{r}_i, \mathbf{R}_b+\mathbf{r}_j) e^{-i(\mathbf{k}'+\mathbf{K}')(\mathbf{R}_b+\mathbf{r}_j)}. \quad (3.27)$$

As a notation we write \mathbf{k} for the reciprocal vectors of the reduced Brillouin zone according to the superlattice $\mathbf{R} \leftrightarrow \mathbf{k}$ and \mathbf{K} according to the cluster vectors $\mathbf{r} \leftrightarrow \mathbf{K}$ (see Fig. 3.4). With

$e^{i\mathbf{K}\mathbf{R}} = 1$ and the translational invariance due to the superlattice we obtain

$$\begin{aligned}
G(\mathbf{k} + \mathbf{K}, \mathbf{k}' + \mathbf{K}') &= \frac{1}{N_c L_c} \sum_{l,b,i,j} e^{i(\mathbf{k}+\mathbf{K})\mathbf{r}_i} G(\mathbf{R}_b + \mathbf{R}_l + \mathbf{r}_i, \mathbf{R}_b + \mathbf{r}_j) e^{-i(\mathbf{k}'+\mathbf{K}')\mathbf{r}_j} \\
&\quad \times e^{i(\mathbf{k}-\mathbf{k}')\mathbf{R}_b} e^{i\mathbf{k}\mathbf{R}_l} \\
&= \frac{1}{L_c} \sum_{l,i,j} e^{i(\mathbf{k}+\mathbf{K})\mathbf{r}_i} G(\mathbf{R}_l + \mathbf{r}_i, \mathbf{0} + \mathbf{r}_j) e^{-i(\mathbf{k}'+\mathbf{K}')\mathbf{r}_j} \delta_{\mathbf{k},\mathbf{k}'} e^{i\mathbf{k}\mathbf{R}_l} \\
&= \frac{1}{L_c} \sum_{i,j} e^{i(\mathbf{k}+\mathbf{K})\mathbf{r}_i} G_{ij}(\mathbf{k}) e^{-i(\mathbf{k}'+\mathbf{K}')\mathbf{r}_j} \delta_{\mathbf{k},\mathbf{k}'} . \tag{3.28}
\end{aligned}$$

The Green's function is no longer in a mixed representation. To restore the translational invariance only the diagonal elements are taken into account $G(\mathbf{k} + \mathbf{K}) := G(\mathbf{k} + \mathbf{K}, \mathbf{k} + \mathbf{K}') \delta_{\mathbf{K},\mathbf{K}'}$. The \mathbf{k} vector is an element of the reduced Brillouin zone according to the superlattice and as N_c is in principle an infinite number, \mathbf{k} is continuous. However, \mathbf{K} is a vector of the reciprocal lattice whose smallest non-zero value is exactly the periodicity of the reduced Brillouin zone. Therefore we can rewrite the Green's function as $G(\mathbf{k}) := G(\mathbf{k}, \mathbf{k})$ with \mathbf{k} a continuous element of the original Brillouin zone. For details using the example of one dimension see appendix A.1.

The *diagonalization* of the Green's function is not the only possible choice for the restoration of the translational invariance. One could also apply the above procedure to the self-energy. But due to the matrix operations arising from the Dyson equation the result differs from Eq. (3.28). However, experience tells us to proceed in the way explained above, as it yields better results (103). See, for a deeper discussion on this topic Ref. (106).

3.1.4 Limits of the VCA

First we want to analyze the $L_c \rightarrow \infty$ limit. As the exact self-energy is captured by the reference system in this case, the VCA becomes exact.

For a vanishing hopping matrix $\mathbf{T} = \mathbf{0}$ all lattice sites decouple and the self-energy is local. Therefore the exact self-energy is captured even by an one-site cluster and the VCA becomes exact.

At last we consider the non-interacting limit. As the self-energy of the original system and of the reference system is zero, the VCA also becomes exact in this limit.

3.1.5 Choice of variational parameters and thermodynamic consistency

This section is addressed to the choice of appropriate variational parameters. A larger parameter space means also a larger space of trial self-energies and improves the approach. But the numerical effort arising from the variational procedure to find the stationary points limits the number of parameters. Therefore one has to make a thorough decision which parameters to take into account and which not. The aim of this work is to analyze the physics of

high-temperature superconductors microscopically. And by taking into consideration the phase diagram of the cuprate superconductors two phases are apparently dominant. The antiferromagnetic at low doping and, of course, the d-wave superconducting phase at higher doping. For this reason we introduce an U(1) symmetry breaking pairing field and a SU(2) symmetry breaking antiferromagnetic field:

$$\Delta_{SC}(\mathbf{R}_a) = h_{SC} \sum_{n.n.} \frac{\eta_{ij}}{2} (c_{ai\uparrow} c_{aj\downarrow} + h.c.) \quad (3.29)$$

$$\Delta_{AF}(\mathbf{R}_a) = h_{AF} \sum_i (n_{ai\uparrow} - n_{ai\downarrow}) e^{i\mathbf{q}_{AF} \cdot \mathbf{r}_i} \quad (3.30)$$

$\mathbf{q}_{AF} = (\pi, \pi)$ is the antiferromagnetic wave vector in two dimensions and η_{ij} accounts for the d-wave pairing and is defined as

$$\eta_{ij} = \begin{cases} +1, & \text{for } \mathbf{r}_i - \mathbf{r}_j \text{ in x-direction} \\ -1, & \text{for } \mathbf{r}_i - \mathbf{r}_j \text{ in y-direction} \end{cases} \quad (3.31)$$

Beside the phases of interest, the choice of the variational parameter is crucial also for the thermodynamic consistence. This means the equivalence of a quantity on the one hand calculated via the spectral theorem (86; 87; 88; 89)

$$\langle c_{i\sigma}^\dagger c_{j\sigma} \rangle = \int_{-\infty}^{\infty} d\omega \frac{A_{ij\sigma}(\omega)}{1 + e^{\beta\omega}}, \quad (3.32)$$

and on the other hand as the derivation of a thermodynamic potential

$$\langle c_{i\sigma}^\dagger c_{j\sigma} \rangle = \frac{\delta\Omega}{\delta t_{ij\sigma}}. \quad (3.33)$$

As both, the grand potential and the Green's function and therefore the spectral function are approximated, this equivalence is not necessary. However, the introduction of a variational parameter $t'_{ij\sigma}$ in the reference system corresponding to $t_{ij\sigma}$ in the original system ensures the thermodynamic consistence for the considered quantity. To proof this statement we evaluate Eq. (3.33):

$$\frac{\delta\Omega_t[\Sigma(\mathbf{t}'_{opt})]}{\delta t_{ij\sigma}} = T \sum_n (\mathbf{G}_0^{-1}(i\omega_n^f) - \Sigma(\mathbf{t}'_{opt}, i\omega_n^f))_{j i \sigma}^{-1} + \underbrace{\frac{\delta\Omega_t[\Sigma(\mathbf{t}'_{opt})]}{\delta \mathbf{t}'}}_{=0} \Big|_{\mathbf{t}'=\mathbf{t}'_{opt}} \frac{\delta \mathbf{t}'_{opt}}{\delta t_{ij\sigma}} \quad (3.34)$$

The first part of the right side stems from the explicit $t_{ij\sigma}$ dependence of the \mathbf{G}_0 while the second one stems from the implicit dependence of the variational parameter on $t_{ij\sigma}$. The latter vanishes as the derivative of the grand potential is evaluated at a stationary point. And the sum in the first part can be transformed by use of the Matsubara sum (see appendix A.2.1) into an integral over real frequencies and becomes Eq. (3.32), q.e.d..

In this work we analyze in detail the doping dependence of physical quantities. For this reason we want to ensure the thermodynamic consistence of the particle number $N = \sum_{i\sigma} \langle c_{i\sigma}^\dagger c_{i\sigma} \rangle$ and introduce an onsite energy as a third variational parameter:

$$\Delta_\mu(\mathbf{R}_a) = \mu' \sum_i (n_{ai\uparrow} + n_{ai\downarrow}) \quad (3.35)$$

3.1.6 Q-matrix formalism - Numerical evaluation

In this section we introduce a formalism which allows for an effective computation of the VCA and, furthermore, provides a good starting point for an elegant derivation of a two-particle approach. This formalism is based on the Lehmann representation (86; 87; 88; 89) for the cluster Green's function

$$\begin{aligned}
G_{\alpha\beta}^c(i\omega_l^f) &= \frac{1}{Z'} \sum_{m,n} \frac{\langle m|c_\alpha|n\rangle\langle n|c_\beta^\dagger|m\rangle}{i\omega_l^f - (E_n - E_m)} (e^{-\beta E_m} + e^{-\beta E_n}) \\
&\stackrel{T \rightarrow 0}{=} \frac{1}{d} \sum_{m,n} \left(\frac{\langle 0_m|c_\alpha|n\rangle\langle n|c_\beta^\dagger|0_m\rangle}{i\omega_l^f - (E_n - E_0)} + \frac{\langle 0_n|c_\beta^\dagger|m\rangle\langle m|c_\alpha|0_n\rangle}{i\omega_l^f - (E_0 - E_m)} \right). \quad (3.36)
\end{aligned}$$

We used d for the possible degeneration of the ground state and Z' as the grand canonical partition function. The exact solution of the cluster is achieved by employing the Lanczos algorithm (see section 3.4) which yields the eigenvalues and eigenstates of the hamiltonian up to a certain energy. With these we define the so-called Q-matrix which essentially contains the spectral weights of the one-particle excitations. Note, that we assume the chemical potential μ as already included in the hamiltonian $\mathcal{H} = H - \mu N$.

$$\begin{aligned}
Q_{\alpha s} &= \langle m|c_\alpha|n\rangle \sqrt{\frac{e^{-\beta E_m} + e^{-\beta E_n}}{Z'}} \\
&\stackrel{T \rightarrow 0}{=} \frac{1}{\sqrt{d}} (\delta_{E_m, E_0} \langle 0_m|c_\alpha|n\rangle + \delta_{E_n, E_0} \langle m|c_\alpha|0_n\rangle) \quad (3.37)
\end{aligned}$$

The index s denotes as a double index the two states $s = (m, n)$. With the matrix

$$g_{st}(\omega) = \frac{\delta_{st}}{\omega - (E_n - E_m)} = \frac{\delta_{st}}{\omega - \omega'_s} \quad (3.38)$$

the Lehmann representation of the cluster Green's function is recovered by

$$\mathbf{G}^c(i\omega_l^f) = \mathbf{Q} \mathbf{g}(i\omega_l^f) \mathbf{Q}^\dagger \quad (3.39)$$

The latter result allows us to rewrite the VCA Green's function (Eq. 3.26) with the simplified notation $\bar{\mathbf{V}}(\mathbf{k}) = \mathbf{V}(\mathbf{k}) - \mathbf{\Delta}$:

$$\begin{aligned}
\mathbf{G}(\mathbf{k}, i\omega_l^f) &= \left(\left(\mathbf{Q} \mathbf{g}(i\omega_l^f) \mathbf{Q}^\dagger \right)^{-1} - \bar{\mathbf{V}}(\mathbf{k}) \right)^{-1} \\
&= \mathbf{Q} \mathbf{g}(i\omega_l^f) \mathbf{Q}^\dagger \sum_{l=0}^{\infty} \left(\bar{\mathbf{V}}(\mathbf{k}) \mathbf{Q} \mathbf{g}(i\omega_l^f) \mathbf{Q}^\dagger \right)^l \\
&= \mathbf{Q} \mathbf{g}(i\omega_l^f) \sum_{l=0}^{\infty} \left(\mathbf{Q}^\dagger \bar{\mathbf{V}}(\mathbf{k}) \mathbf{Q} \mathbf{g}(i\omega_l^f) \right)^l \mathbf{Q}^\dagger \\
&= \mathbf{Q} \left(\mathbf{g}^{-1}(i\omega_l^f) - \mathbf{Q}^\dagger \bar{\mathbf{V}}(\mathbf{k}) \mathbf{Q} \right)^{-1} \mathbf{Q}^\dagger \quad (3.40)
\end{aligned}$$

As the $\mathbf{g}(i\omega_l^f)$ is a diagonal matrix the inverse is easily $\mathbf{g}^{-1}(i\omega_l^f) = i\omega_l^f - \mathbf{\Lambda}$ with the definition $\Lambda_{st} = \delta_{st}\omega_s'$. This allows for a further simplification

$$\mathbf{G}(\mathbf{k}, i\omega_l^f) = \mathbf{Q} \left(i\omega_l^f - \mathbf{M}(\mathbf{k}) \right)^{-1} \mathbf{Q}^\dagger. \quad (3.41)$$

The poles of the VCA Green's function are given by the eigenvalues of the matrix $\mathbf{M}(\mathbf{k}) = \mathbf{\Lambda} + \mathbf{Q}^\dagger \bar{\mathbf{V}}(\mathbf{k}) \mathbf{Q}$ via $\omega_s(\mathbf{k}) = (\mathbf{U}^\dagger(\mathbf{k}) \mathbf{M}(\mathbf{k}) \mathbf{U}(\mathbf{k}))_{ss}$ with $\mathbf{U}(\mathbf{k})$ the unitary transformation which diagonalizes $\mathbf{M}(\mathbf{k})$.

The knowledge about the discrete pole structure enables us to evaluate infinite Matsubara sums as well as numerical integrations along the real ω -axis occurring in the expressions for expectation values and the grand potential. In the following the $T = 0$ expression for the particle density will be derived as an example.

$$\begin{aligned} \langle c_{i\sigma}^\dagger c_{i\sigma} \rangle &= \frac{1}{N_c} \sum_{\mathbf{k}} \int_{-\infty}^{\infty} d\omega \frac{A_{ii\sigma}(\mathbf{k}, \omega)}{1 + e^{\beta\omega}} = \frac{1}{N_c} \sum_{\mathbf{k}} \int_{-\infty}^0 d\omega A_{ii\sigma}(\mathbf{k}, \omega) \\ &= -\frac{1}{\pi} \frac{1}{N_c} \sum_{\mathbf{k}} \int_{-\infty}^0 d\omega \operatorname{Im} \left[\mathbf{Q} (\omega + i0^+ - \mathbf{M}(\mathbf{k}))^{-1} \mathbf{Q}^\dagger \right]_{ii\sigma} \\ &= -\frac{1}{\pi} \frac{1}{N_c} \sum_{\mathbf{k}} \int_{-\infty}^0 d\omega \operatorname{Im} \left[\sum_s (\mathbf{Q} \mathbf{U}(\mathbf{k}))_{i\sigma s} \frac{1}{\omega + i0^+ - \omega_s(\mathbf{k})} (\mathbf{U}^\dagger(\mathbf{k}) \mathbf{Q}^\dagger)_{s i\sigma} \right] \\ &= -\frac{1}{\pi} \frac{1}{N_c} \sum_{\mathbf{k}} \int_{-\infty}^0 d\omega \sum_s |\mathbf{Q} \mathbf{U}(\mathbf{k})|_{i\sigma s}^2 \left[\operatorname{Im} \frac{1}{\omega + i0^+ - \omega_s(\mathbf{k})} \right] \\ &\stackrel{*}{=} \frac{1}{N_c} \sum_{\mathbf{k}} \int_{-\infty}^0 d\omega \sum_s |\mathbf{Q} \mathbf{U}(\mathbf{k})|_{i\sigma s}^2 \delta(\omega - \omega_s(\mathbf{k})) \\ &= \frac{1}{N_c} \sum_{\substack{\mathbf{k}, s \\ \omega_s(\mathbf{k}) < 0}} |\mathbf{Q} \mathbf{U}(\mathbf{k})|_{i\sigma s}^2 \end{aligned} \quad (3.42)$$

(*: Here, the Dirac identity is used: $\frac{1}{x-x_0 \pm i0^+} = P \frac{1}{x-x_0} \mp i\pi \delta(x-x_0)$, with P the principal value of the integral)

Note, that the $\langle c_{i\sigma}^\dagger c_{i\sigma} \rangle$ is dependent on the site i as open boundary conditions are used. To obtain a local quantity (such as the density) of the original system in the VCA approach means to average over the cluster sites as the following calculation of the local VCA Green's function shows. Using Eq. (3.28) yields:

$$\begin{aligned} \frac{1}{N_c L_c} \sum_{\mathbf{k}, \mathbf{K}} G(\mathbf{k} + \mathbf{K}, i\omega_l^f) &= \frac{1}{N_c L_c L_c} \sum_{\mathbf{k}, \mathbf{K}, i, j} G_{ij}(\mathbf{k}, i\omega_l^f) e^{i\mathbf{k}(\mathbf{r}_i - \mathbf{r}_j)} e^{i\mathbf{K}(\mathbf{r}_i - \mathbf{r}_j)} \\ &= \frac{1}{N_c L_c} \sum_{\mathbf{k}, i} G_{ii}(\mathbf{k}, i\omega_l^f) e^{i\mathbf{k}(\mathbf{r}_i - \mathbf{r}_i)} = \frac{1}{N_c L_c} \sum_{\mathbf{k}, i} G_{ii}(\mathbf{k}, i\omega_l^f) \\ &= \frac{1}{L_c} \sum_i G_{ii}(\Delta \mathbf{R} = \mathbf{0}, i\omega_l^f) \end{aligned} \quad (3.43)$$

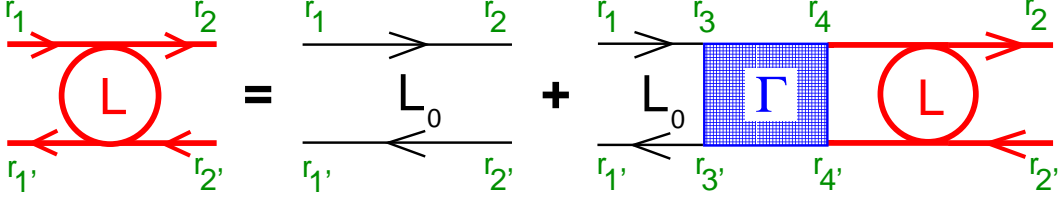


Figure 3.5: Diagrammatic representation of the general Bethe-Salpeter equation. The tiny black lines depict non-interacting one-particle Green's functions.

Hence, the density derived in Eq. (3.42) has also to be averaged over the cluster sites to give the density of the original system in the VCA approach.

The knowledge about the discrete pole structure of the VCA Green's function also enables us to reformulate the grand potential Eq. (3.13) as (details on the derivation are given in (60))

$$\begin{aligned} \Omega_t[\Sigma(\mathbf{t}')] &= \Omega_{t'}[\Sigma(\mathbf{t}')] + T \sum_s \ln(1 + e^{-\beta\omega'_s}) - T \sum_s \ln(1 + e^{-\beta\omega_s}) \\ &\stackrel{T \rightarrow 0}{=} E_0 - \sum_s \omega'_s \Theta(-\omega'_s) + \sum_s \omega_s \Theta(-\omega_s). \end{aligned} \quad (3.44)$$

3.2 Two-particle extension of the VCA for the magnetic susceptibility

The focus of this thesis is on the calculation of two-particle response functions, in particular the transversal magnetic susceptibility χ which yields the magnetic excitation spectrum. Such quantities are obeying the Bethe-Salpeter equation as an analogon to the Dyson equation for one-particle correlation functions. However, as the exact vertex is not known in general, we need an appropriate approximation which works in the strongly-correlated regime. Hence, this section is about a two-step approach with first an approximation to the Bethe-Salpeter equation itself and second an approximation to the two-particle vertex function. That followed, a self-consistently determined controlling constant is introduced to effect a fine-tuning of the vertex function and to assess the quality of the approximation via a checksum.

Note, that the approach derived in this section holds also for other two-particle correlation functions, e.g. the charge response function.

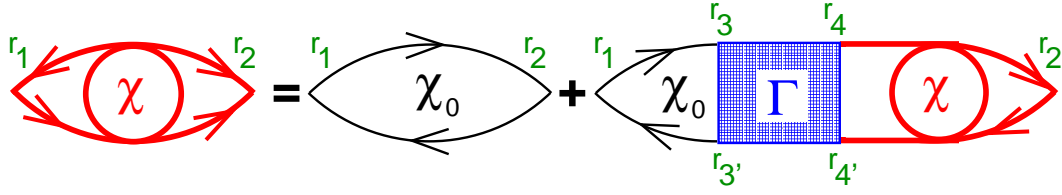


Figure 3.6: Diagrammatic representation of the Bethe-Salpeter equation for the magnetic susceptibility. The tiny black lines depict non-interacting one-particle Green's functions.

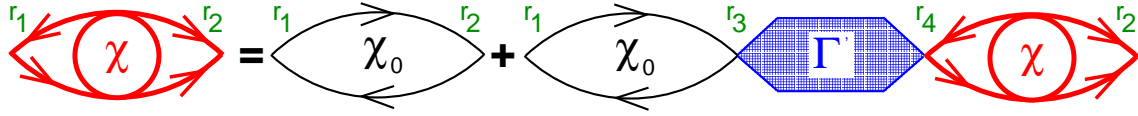


Figure 3.7: Diagrammatic representation of the approximated Bethe-Salpeter equation for the magnetic susceptibility. The tiny black lines depict non-interacting one-particle Green's functions.

3.2.1 Approximation to the Bethe-Salpeter equation

The general Bethe-Salpeter equation for a two-particle response function L is given in real space by (86; 87; 88; 89) (see also Fig. 3.5)

$$L(\bar{r}_1, \bar{r}_1', \bar{r}_2, \bar{r}_2') = L_0(\bar{r}_1, \bar{r}_1', \bar{r}_2, \bar{r}_2') + \sum_{\substack{\mathbf{r}_3, \mathbf{r}_3' \\ \mathbf{r}_4, \mathbf{r}_4' \\ \sigma_3, \sigma_3' \\ \sigma_4, \sigma_4'}} \int d\tau_3 \dots d\tau_4 L_0(\bar{r}_1, \bar{r}_1', \bar{r}_3, \bar{r}_3') \Gamma(\bar{r}_3, \bar{r}_3', \bar{r}_4, \bar{r}_4') L(\bar{r}_4, \bar{r}_4', \bar{r}_2, \bar{r}_2') , \quad (3.45)$$

where we used the four-vector notation $r_i = (\mathbf{r}_i, \tau_i)$ and $\bar{r}_i = (r_i, \sigma_i)$ as a multiple index. Γ denotes the irreducible particle-hole vertex depending, after Fourier transformation, in general on four internal frequencies and momenta which reduces to three internal frequencies and momenta due to momentum and energy conservation. This already gives a hint for the more complex task of calculating two-particle compared to one-particle correlation functions, where the self-energy only depends on one frequency and momentum.

In the following we will consider two-particle response functions which are of the form $\langle\langle A_i B_j \rangle\rangle$ (e.g. the magnetic susceptibility or the charge response function) for which the above equation simplifies as we have to set $r_1 = r_1'$ and $r_2 = r_2'$ (see Fig 3.6). As the structure of the Bethe-Salpeter equation concerning the space and time coordinates is the same for the considered response functions we will shorten the notation by negligence of the spin indices in the following approximation. The obtained result will hold for the transversal magnetic

susceptibility and the longitudinal as well by adapting the spin indices.

However, we still need to deal with a vertex function depending on three internal frequencies and momenta. This will lead to at least dramatical numerical problems. With $\delta_{r_3, r_{3'}} = \delta_{r_3, r_{3'}} \delta(\tau_3 - \tau_{3'})$ and $\delta_{r_4, r_{4'}} = \delta_{r_4, r_{4'}} \delta(\tau_4 - \tau_{4'})$ we achieve an important progress by introducing the following approximation

$$\Gamma(r_3, r_{3'}, r_4, r_{4'}) \longrightarrow \Gamma'(r_3, r_4,) \delta_{r_3, r_{3'}} \delta_{r_4, r_{4'}} . \quad (3.46)$$

In this approximation the response function reads (see also Fig 3.7)

$$\chi(r_1, r_2) = \chi_0(r_1, r_2) + \sum_{r_3, r_4} \int d\tau_3 d\tau_4 \chi_0(r_1, r_3) \Gamma'(r_3, r_4) \chi(r_4, r_2) . \quad (3.47)$$

Using the definition $q_i = (\mathbf{q}_i, \omega_i)$ and $\tilde{q} = (\mathbf{q}, \omega_m^b)$ with ω_i and ω_m^b discrete Matsubara frequencies allows for a compact formulation of the Fourier transform:

$$\begin{aligned} \chi(\mathbf{q}, i\omega_m^b) &= \chi(\tilde{q}, \tilde{q}) = \frac{1}{N} \sum_{r_1, r_2} \int d\tau_1 d\tau_2 \chi(r_1, r_2) e^{i\tilde{q}(r_2 - r_1)} \\ &= \chi_0(\tilde{q}, \tilde{q}) + \sum_{q_1, q_2} \chi_0(\tilde{q}, q_1) \Gamma'(q_1, q_2) \chi(q_2, \tilde{q}) \\ &= \chi_0(\tilde{q}, \tilde{q}) + \chi_0(\tilde{q}, \tilde{q}) \Gamma'(\tilde{q}, \tilde{q}) \chi(\tilde{q}, \tilde{q}) \\ &= \chi_0(\mathbf{q}, i\omega_m^b) + \chi_0(\mathbf{q}, i\omega_m^b) \Gamma'(\mathbf{q}, i\omega_m^b) \chi(\mathbf{q}, i\omega_m^b) \end{aligned} \quad (3.48)$$

We made explicit use of the translational invariance in time and space to only retain the diagonal parts of the interacting and non-interacting response functions.

Shedding light on what the approximation means physically

To gain a deeper understanding of the approximation used above, we implement the approximation Eq. (3.46) via the Fourier representation $\delta_{r_3, r_{3'}} = \delta_{r_3, r_{3'}} \delta(\tau_3 - \tau_{3'}) = \frac{T}{N} \sum_{q_3} e^{iq_3(r_3 - r_{3'})}$ and $\delta_{r_4, r_{4'}} = \delta_{r_4, r_{4'}} \delta(\tau_4 - \tau_{4'}) = \frac{T}{N} \sum_{q_4} e^{iq_4(r_4 - r_{4'})}$ into the Bethe-Salpeter equation Eq. (3.45). With the specialization $r_1 = r_{1'}$ and $r_2 = r_{2'}$ we obtain

$$\chi(r_1, r_2) = \chi_0(r_1, r_2) + \quad (3.49)$$

$$\left(\frac{T}{N}\right)^2 \sum_{\substack{\mathbf{r}_3, \mathbf{r}_{3'} \\ \mathbf{r}_4, \mathbf{r}_{4'} \\ q_3, q_4}} \int d\tau_3 \dots d\tau_{4'} \chi_0(r_1, r_3, r_{3'}) e^{iq_3(r_3 - r_{3'})} \Gamma(r_3, r_{3'}, r_4, r_{4'}) e^{iq_4(r_4 - r_{4'})} \chi(r_4, r_{4'}, r_2) .$$

The Fourier transform yields

$$\begin{aligned}\chi(\mathbf{q}, i\omega_m^b) &= \chi(\tilde{q}, \tilde{q}) = \frac{1}{N} \sum_{\mathbf{r}_1, \mathbf{r}_2} \int d\tau_1 d\tau_2 \chi(r_1, r_2) e^{i\tilde{q}(r_2 - r_1)} \\ &= \chi_0(\tilde{q}, \tilde{q}) + \left(\frac{T}{N}\right)^2 \sum_{\substack{q_1, q_2 \\ q_3, q_4}} \chi_0(q_1, q_1 + \tilde{q}) \times \\ &\quad \times \Gamma[-\tilde{q} - (q_1 - q_3), (q_1 - q_3), (q_2 + q_4), \tilde{q} - (q_2 + q_4)] \chi(-q_2, -q_2 + \tilde{q}) .\end{aligned}$$

The vertex is coupled to χ and χ_0 via q_1 and q_2 . But for each pair of these variables an averaging is performed due to the sum over q_3 and q_4 which, in principle, decouples the vertex from χ and χ_0 :

$$\begin{aligned}\chi(\mathbf{q}, i\omega_m^b) &= \chi(\tilde{q}, \tilde{q}) = \chi_0(\tilde{q}) + \chi_0(\tilde{q}) \tilde{\Gamma}(\tilde{q}) \chi(\tilde{q}) \\ &= \chi_0(\mathbf{q}, i\omega_m^b) + \chi_0(\mathbf{q}, i\omega_m^b) \tilde{\Gamma}(\mathbf{q}, i\omega_m^b) \chi(\mathbf{q}, i\omega_m^b)\end{aligned}\quad (3.50)$$

Of, course the approximation has to render the same result as in Eq. (3.48), which leads to $\tilde{\Gamma}(\mathbf{q}, i\omega_m^b) = \Gamma'(\mathbf{q}, i\omega_m^b)$. In this sense our approximation can be understood as an averaging over the internal frequencies and momenta occurring in the Bethe-Salpeter equation.

Cluster approach

However, we are still faced with the task of calculating the response function of a strong correlated system on an infinite lattice which is not solvable in general. Therefore, we are seeking for a microscopic approach which includes short-range spatial correlations and allows for symmetry breaking long-range phases as the VCA does for the one-particle Green's function. Thus, we act in the spirit of the VCA and introduce a clustering of the real-space lattice. Rewriting Eq. (3.47) in a mixed inter- and intracluster representation yields

$$\begin{aligned}\chi_{ij}(\mathbf{R}_a, \mathbf{R}_b, \tau_1, \tau_2) &= \chi_{0,ij}(\mathbf{R}_a, \mathbf{R}_b, \tau_1, \tau_2) + \\ &\quad \sum_{\substack{\mathbf{R}_c, \mathbf{R}_d \\ i, j}} \int d\tau_3 d\tau_4 \chi_{0,ik}(\mathbf{R}_a, \mathbf{R}_c, \tau_1, \tau_3) \Gamma'_{kl}(\mathbf{R}_c, \mathbf{R}_d, \tau_3, \tau_4) \chi_{lj}(\mathbf{R}_d, \mathbf{R}_b, \tau_4, \tau_2) .\end{aligned}\quad (3.51)$$

Translational invariance only holds for the intercluster indices \mathbf{R} , wherefore Eq. (3.48) turns into a matrix equation in the intracluster indices i, j

$$\chi(\mathbf{q}, i\omega_m^b) = \chi_0(\mathbf{q}, i\omega_m^b) + \chi_0(\mathbf{q}, i\omega_m^b) \Gamma'(\mathbf{q}, i\omega_m^b) \chi(\mathbf{q}, i\omega_m^b) .\quad (3.52)$$

To restore the translational invariance we follow directly the procedure in section 3.1.3. After a Fourier transform with respect to the intracluster indices we only take the diagonal elements into account $\chi(\mathbf{q} + \mathbf{Q}) := \chi(\mathbf{q} + \mathbf{Q}, \mathbf{q} + \mathbf{Q}') \delta_{\mathbf{Q}, \mathbf{Q}'}$. The \mathbf{q} vector is an element of the reduced Brillouin zone according to the superlattice and as N_c is in principle an infinite number, \mathbf{q} is

continuous. However, \mathbf{Q} is a vector of the reciprocal lattice associated with the cluster sites and whose smallest non-zero value is exactly the periodicity of the reduced Brillouin zone. Therefore we can rewrite the susceptibility as $\chi(\mathbf{q}) := \chi(\mathbf{q}, \mathbf{q})$ with \mathbf{q} a continuous element of the original Brillouin zone. For details using the example of one dimension see appendix A.1.

In the following, an approximation to the irreducible particle-hole vertex will be done which is a crucial innovation of the technique presented in this thesis. The vertex will be approximated by an effective vertex obtained from a cluster calculation in the same manner as the self-energy for the one-particle Green's function is obtained. The directly following section deals with the calculation of the *dressed bubble* susceptibility χ_0 . The denotation *dressed bubble* implies the fact, that our χ_0 already contains fully dressed one-particle Green's functions and, thus, the correlated physics at the one-particle level. We will see, that this is important for rendering the non-collective single-particle spin-flip continuum as well as the correct value of the effective vertex. A further section is devoted to the introduction of a controlling mechanism. We employ an exact sum-rule for improving and checking the quality of the used approximation.

We need to mention a special procedure for the calculation in the superconducting phase. According to the broken U(1) symmetry of the hamiltonian the particle number is no longer conserved. But for the purpose of the practical application we introduce a particle-hole transformation with respect to only one spin-channel, here the spin-down channel. With the loss of the hamiltonian's SU(2) symmetry we gain the restoration of the U(1) symmetry, which eases the numerical calculations. See appendix A.3 for details on the particle-hole transformation.

3.2.2 *Dressed bubble* approximation to the magnetic susceptibility

This section deals with the *dressed bubble* approximation to the magnetic susceptibility which, however, captures the fully interacting physics at the one-particle level. This *bubble* susceptibility will be denoted χ_0 . Starting point is the definition of the magnetic susceptibility (86; 87; 88; 89) in a mixed representation according to the inter- and intracluster indices as we consider a superlattice produced by finite clusters

$$\chi_{ij}^{\alpha\beta}(q, i\omega_m^b) = \int_0^\beta d\tau e^{i\omega_m^b \tau} \frac{1}{N_c} \sum_a e^{-i\mathbf{q}\mathbf{R}_a} \langle S_{ai}^\alpha(\tau) S_{0j}^\beta(0) \rangle, \quad (3.53)$$

with the imaginary-time Heisenberg representation $S_i^\alpha(\tau) = e^{H\tau} S_i^\alpha e^{-H\tau}$. The notation concerning the intercluster and intracluster indices is the same we used for the derivation of the VCA. The spin operator S_i^α in the above equation is defined as (86; 87; 88; 89)

$$S_i^\alpha = \begin{pmatrix} c_{i\uparrow}^\dagger & c_{i\downarrow}^\dagger \end{pmatrix} \boldsymbol{\sigma}^\alpha \begin{pmatrix} c_{i\uparrow} \\ c_{i\downarrow} \end{pmatrix}, \quad (3.54)$$

with $\boldsymbol{\sigma}^{x,y,z}$ the Pauli spin matrices

$$\boldsymbol{\sigma}^x = \begin{pmatrix} 0 & 1 \\ 1 & 0 \end{pmatrix}, \quad \boldsymbol{\sigma}^y = \begin{pmatrix} 0 & -i \\ i & 0 \end{pmatrix}, \quad \boldsymbol{\sigma}^z = \begin{pmatrix} 1 & 0 \\ 0 & -1 \end{pmatrix}. \quad (3.55)$$

Due to the scalar product $\mathbf{S}_i \mathbf{S}_j = S_i^z S_j^z + \frac{1}{2} (S_i^+ S_j^- + S_i^- S_j^+)$ where $S_i^\pm = S_i^x \pm i S_i^y$ are the spin ladder operators, we can define a longitudinal (along the z-axis) and a transversal part (in the x,y plane) of the magnetic susceptibility:

$$\chi_{ij}^\pm(q, i\omega_m^b) = \chi_{ij}^{-+}(q, i\omega_m^b), \quad (3.56)$$

$$\chi_{ij}^l(q, i\omega_m^b) = \chi_{ij}^{zz}(q, i\omega_m^b). \quad (3.57)$$

In case of a SU(2) symmetric hamiltonian the transversal and the longitudinal susceptibilities yield the same information. The derivation will be made in great detail for the transversal magnetic susceptibility. For the longitudinal part of magnetic susceptibility we give only the result for brevity.

We consider the transversal magnetic susceptibility

$$\begin{aligned} \chi_{ij}^\pm(q, i\omega_m^b) &= \int_0^\beta d\tau e^{i\omega_m^b \tau} \frac{1}{N_c} \sum_a e^{-i\mathbf{q}\mathbf{R}_a} \langle S_{ai}^-(\tau) S_{0j}^+(0) \rangle \\ &= \int_0^\beta d\tau e^{i\omega_m^b \tau} \frac{1}{N_c} \sum_a e^{-i\mathbf{q}\mathbf{R}_a} \langle T_\tau \{ S_{ai}^-(\tau) S_{0j}^+(0) \} \rangle, \end{aligned} \quad (3.58)$$

and apply the *bubble* approximation to the expectation value $\langle T_\tau \{ S_{ai}^-(\tau) S_{0j}^+(0) \} \rangle$:

$$\begin{aligned} \langle T_\tau \{ c_{ai\downarrow}^\dagger(\tau) c_{ai\uparrow}(\tau) c_{0j\uparrow}^\dagger(0) c_{0j\downarrow}(0) \} \rangle &\approx \langle T_\tau \{ c_{ai\uparrow}(\tau) c_{0j\uparrow}^\dagger(0) \} \rangle \langle T_\tau \{ c_{ai\downarrow}^\dagger(\tau) c_{0j\downarrow}(0) \} \rangle \\ &\quad - \langle T_\tau \{ c_{ai\uparrow}(\tau) c_{0j\downarrow}(0) \} \rangle \langle T_\tau \{ c_{ai\downarrow}^\dagger(\tau) c_{0j\uparrow}^\dagger(0) \} \rangle \\ &= - \langle T_\tau \{ c_{ai\uparrow}(\tau) c_{0j\uparrow}^\dagger(0) \} \rangle \langle T_\tau \{ c_{0j\downarrow}(0) c_{ai\downarrow}^\dagger(\tau) \} \rangle \\ &\quad - \langle T_\tau \{ c_{ai\uparrow}(\tau) c_{0j\downarrow}(0) \} \rangle \langle T_\tau \{ c_{ai\downarrow}^\dagger(\tau) c_{0j\uparrow}^\dagger(0) \} \rangle \\ &= -G_{a0ij\uparrow}(\tau) G_{0aj\downarrow}(-\tau) \\ &\quad - F_{a0ij}(\tau) F_{0aj\downarrow}^*(-\tau). \end{aligned} \quad (3.59)$$

In the last step the normal G and anomalous F (which are vanishing in case of a U(1) symmetric hamiltonian) Green's functions are identified

$$G_{a0ij\uparrow}(\tau) = - \langle T_\tau \{ c_{ai\uparrow}(\tau) c_{0j\uparrow}^\dagger(0) \} \rangle, \quad (3.60)$$

$$F_{a0ij}(\tau) = - \langle T_\tau \{ c_{ai\uparrow}(\tau) c_{0j\downarrow}(0) \} \rangle. \quad (3.61)$$

Translational invariance due to the intercluster index and the periodicity in the imaginary time enables us to insert the Fourier transforms of the Green's functions which yields after a straightforward algebra

$$\begin{aligned} \chi_{0,ij}^\pm(q, i\omega_m^b) &= - \frac{T}{N_c} \sum_{n, \mathbf{k}} (G_{ij\uparrow}(\mathbf{k} + \mathbf{q}, i\omega_n^f + i\omega_m^b) G_{ji\downarrow}(\mathbf{k}, i\omega_n^f) \\ &\quad + F_{ij}(\mathbf{k}, i\omega_n^f) F_{ji}^*(\mathbf{q} - \mathbf{k}, i\omega_m^b - i\omega_n^f)). \end{aligned} \quad (3.62)$$

As already explained, a particle-hole transformation for the spin-down channel is used in case of a U(1) symmetry broken hamiltonian. The following derivation will be done in detail for

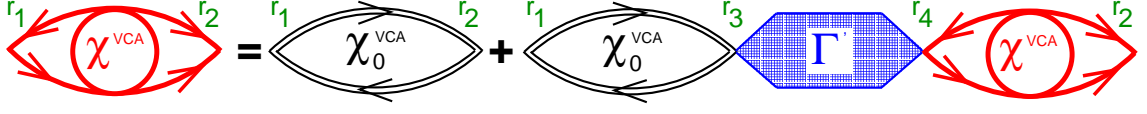


Figure 3.8: Diagrammatic representation of the approximated Bethe-Salpeter equation for the magnetic susceptibility with fully dressed one-particle propagators depicted as double lines.

the particle-hole transformed case while in case of a U(1) symmetric hamiltonian without the particle-hole transformation we only give the results for brevity. With the results of appendix A.3 we obtain the particle-hole transformed *bubble* susceptibility

$$\begin{aligned} \chi_{0,ij}^{\pm,ph}(q, i\omega_m^b) &= \frac{T}{N_c} \sum_{n,\mathbf{k}} \left(G_{ij\uparrow}^{ph}(\mathbf{q} - \mathbf{k}, i\omega_m^b - i\omega_n^f) G_{ij\downarrow}^{ph}(\mathbf{k}, i\omega_n^f) \right. \\ &\quad \left. - G_{ij\uparrow\downarrow}^{ph}(\mathbf{k}, i\omega_n^f) G_{ij\downarrow\uparrow}^{ph}(\mathbf{q} - \mathbf{k}, i\omega_m^b - i\omega_n^f) \right). \end{aligned} \quad (3.63)$$

The basic idea is now to use in the expression for the *bubble* susceptibility χ_0 the fully interacting VCA Green's functions obtained with the same clustering. This idea is depicted diagrammatically in Fig. 3.8. In the subsequent step we are able to insert the Q-matrix representation for the VCA Green's functions Eq. (3.41)

$$\begin{aligned} \chi_{0,ij}^{\pm,ph,VCA}(q, i\omega_m^b) &= \frac{T}{N_c} \sum_{n,\mathbf{k}} \left(G_{ij\uparrow}^{ph,VCA}(\mathbf{q} - \mathbf{k}, i\omega_m^b - i\omega_n^f) G_{ij\downarrow}^{ph,VCA}(\mathbf{k}, i\omega_n^f) \right. \\ &\quad \left. - G_{ij\uparrow\downarrow}^{ph,VCA}(\mathbf{q} - \mathbf{k}, i\omega_m^b - i\omega_n^f) G_{ij\downarrow\uparrow}^{ph,VCA}(\mathbf{k}, i\omega_n^f) \right) \\ &= \frac{T}{N_c} \sum_{n,\mathbf{k}} \left(\left[\mathbf{Q}(i\omega_m^b - i\omega_n^f - \mathbf{M}(\mathbf{q} - \mathbf{k}))^{-1} \mathbf{Q}^\dagger \right]_{ij\uparrow} \left[\mathbf{Q}(i\omega_n^f - \mathbf{M}(\mathbf{k}))^{-1} \mathbf{Q}^\dagger \right]_{ij\downarrow} \right. \\ &\quad \left. - \left[\mathbf{Q}(i\omega_m^b - i\omega_n^f - \mathbf{M}(\mathbf{q} - \mathbf{k}))^{-1} \mathbf{Q}^\dagger \right]_{ij\downarrow\uparrow} \left[\mathbf{Q}(i\omega_n^f - \mathbf{M}(\mathbf{k}))^{-1} \mathbf{Q}^\dagger \right]_{ij\uparrow\downarrow} \right) \\ &= \frac{T}{N_c} \sum_{\substack{n,\mathbf{k},s,t \\ \mu_1,\mu_2,\mu_3,\mu_4}} \left(\frac{Q_{i\uparrow\mu_1} U_{\mu_1 s}(\mathbf{q} - \mathbf{k}) U_{s\mu_2}^\dagger(\mathbf{q} - \mathbf{k}) Q_{\mu_2 j\uparrow}^\dagger Q_{i\downarrow\mu_3} U_{\mu_3 t}(\mathbf{k}) U_{t\mu_4}^\dagger(\mathbf{k}) Q_{\mu_4 j\downarrow}^\dagger}{i\omega_m^b - i\omega_n^f - \omega_s(\mathbf{q} - \mathbf{k})} \frac{Q_{i\downarrow\mu_3} U_{\mu_3 t}(\mathbf{k}) U_{t\mu_4}^\dagger(\mathbf{k}) Q_{\mu_4 j\downarrow}^\dagger}{i\omega_n^f - \omega_t(\mathbf{k})} \right. \\ &\quad \left. - \frac{Q_{i\downarrow\mu_1} U_{\mu_1 s}(\mathbf{q} - \mathbf{k}) U_{s\mu_2}^\dagger(\mathbf{q} - \mathbf{k}) Q_{\mu_2 j\uparrow}^\dagger Q_{i\uparrow\mu_3} U_{\mu_3 t}(\mathbf{k}) U_{t\mu_4}^\dagger(\mathbf{k}) Q_{\mu_4 j\downarrow}^\dagger}{i\omega_m^b - i\omega_n^f - \omega_s(\mathbf{q} - \mathbf{k})} \frac{Q_{i\uparrow\mu_3} U_{\mu_3 t}(\mathbf{k}) U_{t\mu_4}^\dagger(\mathbf{k}) Q_{\mu_4 j\downarrow}^\dagger}{i\omega_n^f - \omega_t(\mathbf{k})} \right) \\ &= \frac{1}{N_c} \sum_{\substack{\mathbf{k},s,t \\ \mu_1,\mu_2,\mu_3,\mu_4}} \left(Q_{i\uparrow\mu_1} U_{\mu_1 s}(\mathbf{q} - \mathbf{k}) U_{s\mu_2}^\dagger(\mathbf{q} - \mathbf{k}) Q_{\mu_2 j\uparrow}^\dagger Q_{i\downarrow\mu_3} U_{\mu_3 t}(\mathbf{k}) U_{t\mu_4}^\dagger(\mathbf{k}) Q_{\mu_4 j\downarrow}^\dagger \right. \\ &\quad \left. - Q_{i\downarrow\mu_1} U_{\mu_1 s}(\mathbf{q} - \mathbf{k}) U_{s\mu_2}^\dagger(\mathbf{q} - \mathbf{k}) Q_{\mu_2 j\uparrow}^\dagger Q_{i\uparrow\mu_3} U_{\mu_3 t}(\mathbf{k}) U_{t\mu_4}^\dagger(\mathbf{k}) Q_{\mu_4 j\downarrow}^\dagger \right) \\ &\quad \times \Xi_{st}(\mathbf{q}, \mathbf{k}, i\omega_m^b), \end{aligned} \quad (3.64)$$

with $\Xi_{st}(\mathbf{q}, \mathbf{k}, i\omega_m^b)$ the frequency sum, which can be evaluated due to the knowledge of the discrete pole structure $\omega_s(\mathbf{k})$. We make intense use of the technique of Matsubara sums which is explained in the appendix A.2.1 in detail.

$$\begin{aligned}
\Xi_{st}(\mathbf{q}, \mathbf{k}, i\omega_m^b) &= T \sum_n \frac{1}{i\omega_m^b - i\omega_n^f - \omega_s(\mathbf{q} - \mathbf{k})} \frac{1}{i\omega_n^f - \omega_t(\mathbf{k})} \\
&= \frac{1}{2\pi i} \oint_{C_3} d\omega f(\omega) \frac{1}{\omega - i\omega_m^b + \omega_s(\mathbf{q} - \mathbf{k})} \frac{1}{\omega - \omega_t(\mathbf{k})} \\
&= - \sum_{\text{RES}} f(\omega) \frac{1}{\omega - i\omega_m^b + \omega_s(\mathbf{q} - \mathbf{k})} \frac{1}{\omega - \omega_t(\mathbf{k})}
\end{aligned} \tag{3.65}$$

Enclosed by the path C_3 are the two poles $i\omega_m^b - \omega_s(\mathbf{q} - \mathbf{k})$ and $\omega_t(\mathbf{k})$ leading to

$$\begin{aligned}
\Xi_{st}(\mathbf{q}, \mathbf{k}, i\omega_m^b) &= f(i\omega_m^b - \omega_s(\mathbf{q} - \mathbf{k})) \frac{-1}{i\omega_m^b - \omega_s(\mathbf{q} - \mathbf{k}) - \omega_t(\mathbf{k})} \\
&\quad + f(\omega_t(\mathbf{k})) \frac{-1}{\omega_t(\mathbf{k}) - i\omega_m^b + \omega_s(\mathbf{q} - \mathbf{k})} \\
&= \frac{f(\omega_t(\mathbf{k})) - f(i\omega_m^b - \omega_s(\mathbf{q} - \mathbf{k}))}{i\omega_m^b - (\omega_s(\mathbf{q} - \mathbf{k}) + \omega_t(\mathbf{k}))}.
\end{aligned} \tag{3.66}$$

For a further simplification, we consider the Fermi distribution $f(i\omega_m^b - \omega_s(\mathbf{q} - \mathbf{k}))$:

$$\begin{aligned}
f(i\omega_m^b - \omega_s(\mathbf{q} - \mathbf{k})) &= \frac{1}{e^{\beta(i\omega_m^b - \omega_s(\mathbf{q} - \mathbf{k}))} + 1} = \frac{1}{e^{-\beta\omega_s(\mathbf{q} - \mathbf{k})} e^{i\beta\omega_m^b} + 1} \\
&= \frac{1}{e^{-\beta\omega_s(\mathbf{q} - \mathbf{k})} \underbrace{e^{im2\pi}}_{=1} + 1} = f(-\omega_s(\mathbf{q} - \mathbf{k}))
\end{aligned} \tag{3.67}$$

For clarity, the abbreviation $P_{i\uparrow s}(\mathbf{k}) = \sum_{\mu} Q_{i\uparrow\mu} U_{\mu s}(\mathbf{k})$ is introduced and together with the frequency sum the equation Eq. (3.64) becomes

$$\begin{aligned}
\chi_{0,ij}^{\pm,ph,VCA}(q, i\omega_m^b) &= \frac{1}{N_c} \sum_{\mathbf{k}, s, t} \left(P_{i\uparrow s}(\mathbf{q} - \mathbf{k}) P_{s j \uparrow}^{\dagger}(\mathbf{q} - \mathbf{k}) P_{i \downarrow t}(\mathbf{k}) P_{t j \downarrow}^{\dagger}(\mathbf{k}) \right. \\
&\quad \left. - P_{i \downarrow s}(\mathbf{q} - \mathbf{k}) P_{s j \uparrow}^{\dagger}(\mathbf{q} - \mathbf{k}) P_{i \uparrow t}(\mathbf{k}) P_{t j \downarrow}^{\dagger}(\mathbf{k}) \right) \\
&\quad \times \frac{f(\omega_t(\mathbf{k})) - f(-\omega_s(\mathbf{q} - \mathbf{k}))}{i\omega_m^b - (\omega_s(\mathbf{q} - \mathbf{k}) + \omega_t(\mathbf{k}))}.
\end{aligned} \tag{3.68}$$

Next, the retarded *bubble* susceptibility is obtained by analytically continuing from the bosonic Matsubara frequencies to the real axis and as we are basically interested in the ground state

properties we also consider the $T = 0$ limit:

$$\begin{aligned} \chi_{0,ij}^{\pm,ph,VCA}(q, \omega) = & -\frac{1}{N_c} \sum_{\mathbf{k},s,t} \left(P_{i\uparrow s}(\mathbf{q} - \mathbf{k}) P_{sj\uparrow}^\dagger(\mathbf{q} - \mathbf{k}) P_{i\downarrow t}(\mathbf{k}) P_{tj\downarrow}^\dagger(\mathbf{k}) \right. \\ & \left. - P_{i\downarrow s}(\mathbf{q} - \mathbf{k}) P_{sj\downarrow}^\dagger(\mathbf{q} - \mathbf{k}) P_{i\uparrow t}(\mathbf{k}) P_{tj\uparrow}^\dagger(\mathbf{k}) \right) \\ & \times \frac{\Theta(\omega_s(\mathbf{q} - \mathbf{k})) + \Theta(\omega_t(\mathbf{k})) - 1}{\omega + i0^+ - (\omega_s(\mathbf{q} - \mathbf{k}) + \omega_t(\mathbf{k}))} \end{aligned} \quad (3.69)$$

The $T = 0$ normal state *bubble* susceptibility without the particle-hole transformation is:

$$\begin{aligned} \chi_{0,ij}^{\pm,VCA}(q, \omega) = & -\frac{1}{N_c} \sum_{\mathbf{k},s,t} P_{i\uparrow s}(\mathbf{q} + \mathbf{k}) P_{sj\uparrow}^\dagger(\mathbf{q} + \mathbf{k}) P_{j\downarrow t}(\mathbf{k}) P_{ti\downarrow}^\dagger(\mathbf{k}) \\ & \times \frac{\Theta(\omega_s(\mathbf{q} + \mathbf{k})) - \Theta(\omega_t(\mathbf{k}))}{\omega + i0^+ - (\omega_s(\mathbf{q} + \mathbf{k}) - \omega_t(\mathbf{k}))} \end{aligned} \quad (3.70)$$

The derivation of the longitudinal magnetic susceptibility at $T = 0$ proceeds analogous to the transversal magnetic susceptibility. Hence, we only give the results for brevity:

$$\begin{aligned} \chi_{0,ij}^{l,ph,VCA}(q, \omega) = & -\frac{1}{4N_c} \sum_{\mathbf{k},s,t,\sigma} \left(P_{i\sigma s}(\mathbf{q} + \mathbf{k}) P_{sj\sigma}^\dagger(\mathbf{q} + \mathbf{k}) P_{j\sigma t}(\mathbf{k}) P_{ti\sigma}^\dagger(\mathbf{k}) \right. \\ & \left. + P_{i\sigma s}(\mathbf{q} + \mathbf{k}) P_{sj-\sigma}^\dagger(\mathbf{q} + \mathbf{k}) P_{j-\sigma t}(\mathbf{k}) P_{ti\sigma}^\dagger(\mathbf{k}) \right) \\ & \times \frac{\Theta(\omega_s(\mathbf{q} + \mathbf{k})) - \Theta(\omega_t(\mathbf{k}))}{\omega + i0^+ - (\omega_s(\mathbf{q} + \mathbf{k}) - \omega_t(\mathbf{k}))} \end{aligned} \quad (3.71)$$

$$\begin{aligned} \chi_{0,ij}^{l,VCA}(q, \omega) = & -\frac{1}{4N_c} \sum_{\mathbf{k},s,t,\sigma} P_{i\sigma s}(\mathbf{q} + \mathbf{k}) P_{sj\sigma}^\dagger(\mathbf{q} + \mathbf{k}) P_{j\sigma t}(\mathbf{k}) P_{ti\sigma}^\dagger(\mathbf{k}) \\ & \times \frac{\Theta(\omega_s(\mathbf{q} + \mathbf{k})) - \Theta(\omega_t(\mathbf{k}))}{\omega + i0^+ - (\omega_s(\mathbf{q} + \mathbf{k}) - \omega_t(\mathbf{k}))} \end{aligned} \quad (3.72)$$

The results for the susceptibilities resemble the common non-interacting susceptibility

$$\chi_0(\mathbf{q}, \omega) = \sum_{\mathbf{k},\sigma} \frac{n_{\mathbf{k}\sigma}^0 - n_{\mathbf{k}+\mathbf{q}\sigma}^0}{\omega + i0^+ - (\omega(\mathbf{k} + \mathbf{q}) - \omega(\mathbf{k}))}, \quad (3.73)$$

where $n_{\mathbf{k}\sigma}^0$ is the non-interacting occupation number. But our approach includes the fully renormalized one-particle excitation energies as well as the renormalization of the quasi-particle spectral weights effected by the P -matrices.

3.2.3 Effective vertex

This section is devoted to the development of an effective vertex which allows for a numerical calculation. We use the χ_0^{VCA} derived in the latter section in the approximated Bethe-Salpeter equation Eq. (3.52)

$$\chi(\mathbf{q}, i\omega_m^b) = \chi_0^{VCA}(\mathbf{q}, i\omega_m^b) + \chi_0^{VCA}(\mathbf{q}, i\omega_m^b)\Gamma'(\mathbf{q}, i\omega_m^b)\chi(\mathbf{q}, i\omega_m^b). \quad (3.74)$$

This defines the vertex

$$\Gamma' = (\chi_0^{VCA}(\mathbf{q}, i\omega_m^b))^{-1} - (\chi(\mathbf{q}, i\omega_m^b))^{-1}. \quad (3.75)$$

But this vertex is still not attainable as the exact susceptibility occurs in the equation. We need to introduce a further approximation which is motivated from the VCA itself. In fact, we restrict the calculation of the vertex function to a finite cluster which is exactly the same that renders the self-energy for the VCA

$$\Gamma_{eff}(i\omega_m^b) = (\chi_0^c(i\omega_m^b))^{-1} - (\chi^c(i\omega_m^b))^{-1}. \quad (3.76)$$

With this approximated vertex the susceptibility is feasible to calculate

$$\chi(\mathbf{q}, i\omega_m^b) = (\mathbb{1} - \chi_0^{VCA}(\mathbf{q}, i\omega_m^b)\Gamma_{eff}(i\omega_m^b))^{-1} \chi_0^{VCA}(\mathbf{q}, i\omega_m^b). \quad (3.77)$$

We already mention, that we are going to introduce a constant factor α which modifies the effective vertex and serves as a indicator for the quality of our approach. Furthermore, with this α it can be achieved a fine-tuning of the effective vertex to render the correct pole structure of the susceptibility from Eq. (3.77)

$$\Gamma_{eff}(i\omega_m^b) \longrightarrow \alpha\Gamma_{eff}(i\omega_m^b) \quad ; \quad \alpha \in \mathbb{R}. \quad (3.78)$$

It is very important to make sure, that α is not an adjustable free parameter, but rather a self-consistently determined number. This will be detailed in section 3.2.4.

For the evaluation of the effective vertex only cluster quantities are invoked. The $\chi_0^c(i\omega_m^b)$ emerges as the restriction of $\chi_0^{VCA}(\mathbf{q}, i\omega_m^b)$ to the finite cluster and becomes the convolution of the exact cluster Green's functions Eq. (3.39). The derivation follows exactly the procedure of the last section and yields the simpler result ($T = 0$):

$$\begin{aligned} \chi_{0,ij}^{\pm,ph,c}(q, \omega) &= - \sum_{s,t} \left(Q_{i\uparrow s} Q_{sj\uparrow}^\dagger Q_{i\downarrow t} Q_{tj\downarrow}^\dagger - Q_{i\downarrow s} Q_{sj\uparrow}^\dagger Q_{i\uparrow t} Q_{tj\downarrow}^\dagger \right) \\ &\quad \times \frac{\Theta(\omega'_s) + \Theta(\omega'_t) - 1}{\omega + i0^+ - (\omega'_s + \omega'_t)} \end{aligned} \quad (3.79)$$

$$\chi_{0,ij}^{\pm,c}(q, \omega) = - \sum_{s,t} Q_{i\uparrow s} Q_{sj\uparrow}^\dagger Q_{j\downarrow t} Q_{ti\downarrow}^\dagger \frac{\Theta(\omega'_s) - \Theta(\omega'_t)}{\omega + i0^+ - (\omega'_s - \omega'_t)} \quad (3.80)$$

$$\chi_{0,ij}^{l,ph,c}(q, \omega) = - \sum_{s,t,\sigma} \left(Q_{i\sigma s} Q_{sj\sigma}^\dagger Q_{j\sigma t} Q_{ti\sigma}^\dagger + Q_{i\sigma s} Q_{sj-\sigma}^\dagger Q_{j-\sigma t} Q_{ti\sigma}^\dagger \right) \times \frac{\Theta(\omega'_s) - \Theta(\omega'_t)}{\omega + i0^+ - (\omega'_s - \omega'_t)} \quad (3.81)$$

$$\chi_{0,ij}^{l,c}(q, \omega) = - \sum_{s,t,\sigma} Q_{i\sigma s} Q_{sj\sigma}^\dagger Q_{j\sigma t} Q_{ti\sigma}^\dagger \frac{\Theta(\omega'_s) - \Theta(\omega'_t)}{\omega + i0^+ - (\omega'_s - \omega'_t)} \quad (3.82)$$

Besides these *bubble* susceptibilities the exact cluster susceptibility $\chi^c(i\omega_m^b)$ is needed. But as we are able to calculate the eigenstates and eigenenergies of the cluster the direct calculation via the spectral representation is rendered possible. We provide the general expression for the spectral representation

$$\chi_{ij}^c(i\omega_l^b) = \int_0^\beta d\tau e^{i\omega_l^b \tau} \langle A_i(\tau) B_j(0) \rangle = - \int_{-\infty}^{\infty} d\omega' \frac{S_{A_i B_j}(\omega')}{i\omega_l^b - \omega'} , \quad (3.83)$$

with the spectral function

$$S_{A_i B_j}(\omega) = \frac{1}{Z} \sum_{m,n} \langle m | A_i | n \rangle \langle n | B_j | m \rangle e^{-\beta E_m} (1 - e^{-\beta \omega}) \delta(\omega - (E_n - E_m)) . \quad (3.84)$$

In the $T = 0$ limit we obtain

$$\chi_{ij}^c(\omega) = - \frac{1}{d} \sum_{m,n} \left(\frac{\langle 0_m | A_i | n \rangle \langle n | B_j | 0_m \rangle}{\omega + i0^+ - (E_n - E_0)} - \frac{\langle 0_m | B_j | n \rangle \langle n | A_i | 0_m \rangle}{\omega + i0^+ + (E_n - E_0)} \right) . \quad (3.85)$$

The operators which have to be used for A and B are

$$\begin{array}{ll} \chi^{\pm,c} & : \quad A_i = S_i^- \quad , \quad B_j = S_j^+ \\ \chi^{l,c} & : \quad A_i = S_i^z \quad , \quad B_j = S_j^z \end{array} ,$$

and in case of the particle-hole transformation

$$\begin{array}{ll} \chi^{\pm,c,ph} & : \quad A_i = c_{i\downarrow} c_{i\uparrow} \quad , \quad B_j = c_{j\uparrow}^\dagger c_{j\downarrow}^\dagger \\ \chi^{l,c,ph} & : \quad A_i = c_{i\uparrow}^\dagger c_{i\uparrow} - c_{i\downarrow} c_{i\downarrow}^\dagger \quad , \quad B_j = c_{j\uparrow}^\dagger c_{j\uparrow} - c_{j\downarrow} c_{j\downarrow}^\dagger . \end{array}$$

Calculating the effective vertex in the superconducting phase leads to numerical problems arising from the exact cluster susceptibility. As the magnetic response is small, the inversion of the exact cluster susceptibility is numerically very difficult. For this reason we provide in appendix A.4 a procedure to calculate Eq. (3.77) which avoids this inversion. This transformation is no approximation and is only based on straightforward algebraic operations.

It is noteworthy to mention that the effective vertex is not perturbatively obtained but rather controlled by the size of the clusters producing the infinite superlattice. The same holds for the self-energy of the one-particle Green's function. The latter as well as the susceptibilities will be exact for infinite cluster sizes.

3.2.4 Controlling constant α - Checksum

We already mentioned to include an additional controlling constant α in Eq. (3.78) which is not an adjustable free parameter, but rather a self-consistently determined number. This self-consistent procedure stems from the constraint, that the sum of the susceptibility over all wave vectors and frequencies yields a local and equal-time quantity (similar sum-rules are used in (107) for constructing a controlled local approximation for the irreducible vertex)

$$\frac{T}{N} \sum_{\mathbf{q}, i\omega_m^b} \chi^\pm(\mathbf{q}, i\omega_m^b) = \langle S_i^- S_i^+ \rangle, \quad (3.86)$$

$$\frac{T}{N} \sum_{\mathbf{q}, i\omega_m^b} \chi^l(\mathbf{q}, i\omega_m^b) = \langle (S_i^z)^2 \rangle. \quad (3.87)$$

Such local and equal-time quantities can be also obtained by use of the filling n and the double occupancy d_2 of the system as the following consideration shows:

- For each of the $n - 2d_2$ single-occupied site i , the expectation value $\langle (S_i^z)^2 \rangle$ gives $\frac{1}{4}$ while unoccupied and double-occupied sites yield 0. Hence we obtain $\langle (S_i^z)^2 \rangle = \frac{1}{4}(n - 2d_2)$.
- In case of the transversal susceptibility we use the relation $\mathbf{S}_i \mathbf{S}_j = S_i^z S_j^z + \frac{1}{2}(S_i^+ S_j^- + S_i^- S_j^+)$ in combination with $\langle S_i^+ S_j^- \rangle = \langle S_i^- S_j^+ \rangle$. Since each single-occupied site i gives $\langle \mathbf{S}_i \mathbf{S}_i \rangle = S(S+1) = \frac{3}{4}$ and unoccupied as well as double-occupied sites give $\langle \mathbf{S}_i \mathbf{S}_i \rangle = 0$ we calculate $\langle S_i^- S_i^+ \rangle = \frac{3}{4}(n - 2d_2) - \frac{1}{4}(n - 2d_2) = \frac{1}{2}(n - 2d_2)$.

The only quantity left so far is the double occupancy d_2 . But within the Hubbard model d_2 is the derivative of grand potential with respect to the onsite interaction strength U :

$$d_2 = \left\langle \sum_i n_{i\uparrow} n_{i\downarrow} \right\rangle = \left\langle \frac{d}{dU} H \right\rangle = \frac{d}{dU} \Omega \quad (3.88)$$

The self-consistent calculation that has to be performed is given in the following scheme:

1. Choose a certain α close to 1.
2. Calculate the susceptibility via Eq. (3.77).
3. Evaluate the sum Eq. (3.86)/(3.87).
4. Vary α and turn to item 2.

Run this loop until the sum-rule is fulfilled.

At last we point out the difficulty in evaluating the frequency sum in Eq. (3.86)/(3.87). For real frequencies we have to integrate numerically along the whole real axis, at least in the region where a finite spectral weight of the spin excitation is present. However, there is a rich pole structure along this axis wherefore the mesh of the numerical integration has to be very fine which again intensifies the numerical effort. An important improvement is achieved with the transformation of the integration path given in appendix A.2.2.

3.3 Inelastic light scattering - Raman response

This section is devoted to the calculation of the Raman response. This is a spectroscopic method which uses inelastic light scattering. Since a photon carries an insignificant momentum the Raman response yields information about $\mathbf{q} = \mathbf{0}$ electron-hole excitations. But, nevertheless, it focuses on specific regions in the Brillouin zone adjusted by the polarization of the incoming and scattered photons. That means the $\mathbf{q} = \mathbf{0}$ electron-hole excitations contributing to the total response are specified by the light polarizations. Hence, the Raman response function provides precious momentum resolved information of electron-hole excitations.

First, we derive an approximation to the Raman response function by neglecting many-body corrections of the Raman vertex. But similar to the previous sections concerning the magnetic susceptibility we use the VCA normal and anomalous Green's functions to account for the full interacting physics at the one-particle level. In the subsequent section the bare Raman vertex will be approximated within the so-called effective mass approximation. For this the needed tensor of the effective mass is obtained from the quasi-particle dispersion calculated in the VCA.

The following section concerning the Raman response is based on Ref. (108).

3.3.1 *Dressed bubble approximation to the Raman response*

The Raman response function is defined as the effective density-density correlation function

$$S^R(\mathbf{q}, i\omega_m^b) = \int_0^\beta d\tau e^{i\omega_m^b \tau} \langle \tilde{\rho}(\mathbf{q}, \tau) \tilde{\rho}(-\mathbf{q}, 0) \rangle, \quad (3.89)$$

with the effective density operator

$$\tilde{\rho}(\mathbf{q}, \tau) = \sum_{\mathbf{k}, \sigma} \gamma^\nu(\mathbf{k}, \mathbf{q}) c_\sigma^\dagger(\mathbf{k} + \mathbf{q}, \tau) c_\sigma(\mathbf{k}, \tau). \quad (3.90)$$

The latter definition contains the bare scattering amplitude $\gamma^\nu(\mathbf{k}, \mathbf{q})$ which is determined from the Raman matrix elements as well as the polarization vectors of the incoming (i) and scattered (s) light (the ν is a group theoretical classification which is determined by the pair of polarization vectors)

$$\gamma^\nu(\mathbf{k}, \mathbf{q}) = \sum_{\alpha, \beta} \gamma_{\alpha\beta}(\mathbf{k}, \mathbf{q}) e_{\nu, i}^\alpha e_{\nu, s}^\beta. \quad (3.91)$$

The $e_{\nu, i/s}^\alpha$ is the α component of the polarization vector of the incoming/scattered light and the Raman matrix elements are

$$\gamma_{\alpha\beta}(\mathbf{k}, \mathbf{q}) = \delta_{\alpha, \beta} + \frac{1}{m} \sum_{\mathbf{k}'} \left[\frac{\langle \mathbf{k} + \mathbf{q} | p_s^\beta | \mathbf{k}' \rangle \langle \mathbf{k}' | p_i^\alpha | \mathbf{k} \rangle}{E_{\mathbf{k}} - E_{\mathbf{k}'} + \omega_i} + \frac{\langle \mathbf{k} + \mathbf{q} | p_i^\alpha | \mathbf{k}' \rangle \langle \mathbf{k}' | p_s^\beta | \mathbf{k} \rangle}{E_{\mathbf{k} + \mathbf{q}} - E_{\mathbf{k}'} - \omega_s} \right], \quad (3.92)$$

with $p_{i/s}^\alpha = p^\alpha e^{i\mathbf{q}_{i/s}\cdot\mathbf{r}}$ and p^α the α component of the momentum operator, $\omega_{i/s}$ the frequency of the incoming/scattered photon and m the electron mass.

The Raman response function can be expressed through the Raman susceptibility via the fluctuation-dissipation theorem

$$S^R(\mathbf{q}, \omega) = -\frac{1}{\pi}(1 + b(\omega))\text{Im}\chi^R(\mathbf{q}, \omega), \quad (3.93)$$

with $b(\omega) = \frac{1}{e^{\beta\omega} - 1}$ the Bose-Einstein distribution function.

Since we are interested in the scattering of light, we are allowed to consider the $\mathbf{q} = \mathbf{0}$ limit as the momentum of the photons is small against the momentum of the conduction electrons with which the photons interact $\mathbf{q} \ll \mathbf{k}_F$ (\mathbf{k}_F is the Fermi momentum). Making use of the Nambu formalism the Raman susceptibility in the superconducting phase can be formulated in a compact way

$$\chi^R(\mathbf{q} = \mathbf{0}, i\omega_m^b) = -2\frac{T}{N} \sum_{\mathbf{k}, n} \text{Tr} \left[\hat{\gamma}^\nu(\mathbf{k}) \hat{G}(\mathbf{k}, i\omega_n^f) \hat{\Gamma}(\mathbf{k}, i\omega_n^f, i\omega_m^b) \hat{G}(\mathbf{k}, i\omega_n^f + i\omega_m^b) \right], \quad (3.94)$$

where we used the definition $\hat{\gamma}^\nu(\mathbf{k}) = \boldsymbol{\sigma}^z \gamma^\nu(\mathbf{k})$, $\boldsymbol{\sigma}^z$ the z Pauli matrix. The Nambu Green's function \hat{G} combining the normal G and anomalous F Green's functions (109; 86; 87; 88; 89) reads

$$\hat{G}(\mathbf{k}, i\omega_n^f) = \begin{pmatrix} G_\uparrow(\mathbf{k}, i\omega_n^f) & F(\mathbf{k}, i\omega_n^f) \\ F^*(\mathbf{k}, i\omega_n^f) & -G_\downarrow(\mathbf{k}, -i\omega_n^f) \end{pmatrix}. \quad (3.95)$$

Furthermore, Eq. (3.94) contains the fully interacting Raman vertex $\hat{\Gamma}(\mathbf{k}, i\omega_n^f, i\omega_m^b)$ obeying a Bethe-Salpeter Equation

$$\begin{aligned} \hat{\Gamma}(\mathbf{k}, i\omega_n^f, i\omega_m^b) &= \hat{\gamma}^\nu(\mathbf{k}) + \\ &\underbrace{\frac{T}{N} \sum_{\mathbf{k}', n'} V_i(\mathbf{k} - \mathbf{k}', i\omega_n^f - i\omega_{n'}^f) \boldsymbol{\sigma}^i \hat{G}(\mathbf{k}', i\omega_{n'}^f) \hat{\Gamma}(\mathbf{k}', i\omega_{n'}^f, i\omega_m^b) \hat{G}(\mathbf{k}', i\omega_{n'}^f + i\omega_m^b) \boldsymbol{\sigma}^i}_{\text{vertex corrections}}, \end{aligned} \quad (3.96)$$

with the effective interaction V_i that determines the channel of the vertex corrections, e.g. $i = 0$ for the spin channel ($\boldsymbol{\sigma}^0$ will be the 2x2 identity matrix).

Neglecting the vertex corrections we approximate the interacting Raman vertex with the bare one. After some straightforward matrix operations we obtain the imaginary part of the Raman susceptibility

$$\begin{aligned} \text{Im}\chi^{R,\nu}(i\omega_m^b) &= -\frac{4}{N} \sum_{\mathbf{k}} (\gamma^\nu(\mathbf{k}))^2 \text{Im} \left[T \sum_n (G(\mathbf{k}, i\omega_n^f) G(\mathbf{k}, i\omega_n^f + i\omega_m^b) - \right. \\ &\quad \left. F(\mathbf{k}, i\omega_n^f) F^*(\mathbf{k}, -i\omega_n^f - i\omega_m^b)) \right]. \end{aligned} \quad (3.97)$$

We made explicit use of the fact, that $G_{\uparrow}(\mathbf{k}, i\omega_n^f) = G_{\downarrow}(\mathbf{k}, i\omega_n^f)$ for the relevant phases we are interested in. Further simplifications can be achieved by use of the spectral representations of the normal and anomalous Green's functions

$$G(\mathbf{k}, i\omega_n^f) = \int_{-\infty}^{\infty} d\omega' \frac{A(\mathbf{k}, \omega')}{i\omega_n^f - \omega'}, \quad (3.98)$$

$$F(\mathbf{k}, i\omega_n^f) = \int_{-\infty}^{\infty} d\omega' \frac{B(\mathbf{k}, \omega')}{i\omega_n^f - \omega'}, \quad (3.99)$$

$$\begin{aligned} \text{Im}\chi^{R,\nu}(i\omega_m^b) &= -\frac{4}{N} \sum_{\mathbf{k}} (\gamma^{\nu}(\mathbf{k}))^2 \text{Im} \left[T \sum_n \int_{-\infty}^{\infty} d\omega' \int_{-\infty}^{\infty} d\omega'' \right. \\ &\quad \left. \left(\frac{A(\mathbf{k}, \omega')}{i\omega_n^f - \omega'} \frac{A(\mathbf{k}, \omega'')}{i\omega_n^f + i\omega_m^b - \omega''} - \frac{B(\mathbf{k}, \omega')}{i\omega_n^f - \omega'} \frac{B(\mathbf{k}, \omega'')}{(-i\omega_n^f - i\omega_m^b)^* - \omega''} \right) \right]. \end{aligned} \quad (3.100)$$

With the technique of Matsubara sums (see appendix A.2.1) we make explicit use of the discrete pole structure. And the subsequent continuation from the bosonic Matsubara frequencies to the real axis renders

$$\begin{aligned} \text{Im}\chi^{R,\nu}(i\omega_m^b) &= -\frac{4}{N} \sum_{\mathbf{k}} (\gamma^{\nu}(\mathbf{k}))^2 \text{Im} \int_{-\infty}^{\infty} d\omega' \int_{-\infty}^{\infty} d\omega'' \\ &\quad \left[\left(\frac{A(\mathbf{k}, \omega')A(\mathbf{k}, \omega'')}{\omega' - \omega'' + \omega + i0^+} - \frac{B(\mathbf{k}, \omega')B(\mathbf{k}, \omega'')}{\omega' - \omega'' + \omega + i0^+} \right) (f(\omega') - f(\omega'')) \right], \end{aligned} \quad (3.101)$$

with $f(\omega)$ the Fermi distribution. Next, the imaginary part is calculated by the application of the Dirac identity: $\frac{1}{x-x_0 \pm i0^+} = P \frac{1}{x-x_0} \mp i\pi\delta(x-x_0)$, with P the principal value of the integral

$$\begin{aligned} \text{Im}\chi^{R,\nu}(\omega) &= \sum_{\mathbf{k}} (\gamma_{\mathbf{k}}^{\nu})^2 \int \frac{d\omega'}{4\pi} (f(\omega') - f(\omega + \omega')) \\ &\quad \times (A(\mathbf{k}, \omega + \omega')A(\mathbf{k}, \omega') - B(\mathbf{k}, \omega + \omega')B(\mathbf{k}, \omega')) . \end{aligned} \quad (3.102)$$

The normal and anomalous spectral functions occurring in the above expression are derived via a VCA calculation. This is similar to the approach presented in section 3.2.2. And, since we are interested in the ground state properties, we consider the $T = 0$ limit

$$\begin{aligned} \text{Im}\chi^{R,\nu,VCA}(\omega) &= \sum_{\mathbf{k}} (\gamma_{\mathbf{k}}^{\nu})^2 \int \frac{d\omega'}{4\pi} (\Theta(\omega + \omega') - \Theta(\omega')) \\ &\quad \times (A^{VCA}(\mathbf{k}, \omega + \omega')A^{VCA}(\mathbf{k}, \omega') - B^{VCA}(\mathbf{k}, \omega + \omega')B^{VCA}(\mathbf{k}, \omega')) . \end{aligned} \quad (3.103)$$

3.3.2 Effective mass approximation to the Raman vertex

This section is about an approximation to the bare Raman vertex $\gamma^{\nu}(\mathbf{k})$. The intermediate states in Eq. (3.92) are from the conduction band or from bands separated from the conduction

band. It can be shown, that the matrix elements in the first case are proportional to the momentum transferred by the photon. As this is a very small quantity the contributions to the sum originating from the intermediate states of the conduction band are by a factor of $(v_F/c)^2$ (v_F : Fermi velocity; c : speed of light) smaller compared to the contributions of others than the conduction band. Therefore, the former contributions are negligible. If we assume in addition $\omega_{i/s} \ll E_{\mathbf{k}'} - E_{\mathbf{k}}$, Eq. (3.92) recovers the effective mass of the quasi-particle band (110)

$$\gamma^\nu(\mathbf{k}) \approx \sum_{\alpha,\beta} \gamma_{\alpha\beta}(\mathbf{k}, \mathbf{q} \rightarrow \mathbf{0}) e_{\nu,i}^\alpha e_{\nu,s}^\beta = \sum_{\alpha,\beta} \frac{\partial^2 \varepsilon(\mathbf{k})}{\partial k_\alpha \partial k_\beta} e_{\nu,i}^\alpha e_{\nu,s}^\beta, \quad (3.104)$$

with $\varepsilon(\mathbf{k})$ the quasi-particle dispersion. Since we perform our calculations using the one-band Hubbard model on a square lattice in two dimensions, we consider for the effective mass approximation a tight-binding dispersion. We use an expansion up to 4th nearest neighbor hopping:

$$\varepsilon(\mathbf{k}) = \sum_{i=0}^4 \varepsilon^{(i)}(\mathbf{k}) \quad (3.105)$$

$$\varepsilon^{(0)}(\mathbf{k}) = t_0 \quad (3.106)$$

$$\varepsilon^{(1)}(\mathbf{k}) = 2t_1 (\cos(k_x) + \cos(k_y)) \quad (3.107)$$

$$\varepsilon^{(2)}(\mathbf{k}) = 4t_2 \cos(k_x) \cos(k_y) \quad (3.108)$$

$$\varepsilon^{(3)}(\mathbf{k}) = 2t_3 (\cos(2k_x) + \cos(2k_y)) \quad (3.109)$$

$$\varepsilon^{(4)}(\mathbf{k}) = 4t_4 (\cos(2k_x) \cos(k_y) + \cos(k_x) \cos(2k_y)) \quad (3.110)$$

As we will discuss later, our main interest is in the Raman response for B1g and B2g group symmetries. The polarization vectors for these group symmetries are:

$$\begin{aligned} \mathbf{e}_{B1g,i} &= \frac{1}{\sqrt{2}} \begin{pmatrix} 1 \\ 1 \end{pmatrix} ; \mathbf{e}_{B1g,s} = \frac{1}{\sqrt{2}} \begin{pmatrix} -1 \\ 1 \end{pmatrix} \\ \mathbf{e}_{B2g,i} &= \begin{pmatrix} 1 \\ 0 \end{pmatrix} ; \mathbf{e}_{B2g,s} = \begin{pmatrix} 0 \\ 1 \end{pmatrix} \end{aligned} \quad (3.111)$$

With this we are able to derive the vertex functions for these two symmetries

$$\begin{aligned} \gamma^{B1g}(\mathbf{k}) &\approx t_1 (\cos(k_x) - \cos(k_y)) \\ &\quad + 4t_3 (\cos(2k_x) - \cos(2k_y)) \end{aligned} \quad (3.112)$$

$$\begin{aligned} \gamma^{B2g}(\mathbf{k}) &\approx 4t_2 \sin(k_x) \sin(k_y) + \\ &\quad 8t_4 (\sin(2k_x) \sin(k_y) + \sin(k_x) \sin(2k_y)) . \end{aligned} \quad (3.113)$$

To make a consistent calculation, we obtain the parameters t_0, \dots, t_4 by fitting the tight-binding energy dispersion to the quasi-particle band gained from the VCA calculation.

3.4 Exact Diagonalization using the (Block-)Lanczos algorithm

The whole techniques explained in this chapter are based essentially on the information gained from the solution of an isolated cluster which is a well-defined problem. A set of basis states $\{|\alpha\rangle\}$ can be defined with which the hamiltonian is representable as a matrix $H_{\alpha\beta} = \langle\alpha|H|\beta\rangle$. In principle, it is possible to fully diagonalize this matrix and to obtain the eigenstates and eigenenergies. However, this leads to numerical problems as the size of the Hilbertspace \mathcal{H} grows exponentially with the number of cluster sites (size of $\mathcal{H} : s^{L_c}$, with s the states per site). And even clusters with more than about six sites lead already to insuperable problems concerning the runtime and the memory allocation by use of standard computers for the full diagonalization procedure.

In the following we will explain the so-called (Block-)Lanczos algorithm (we closely follow Refs. (63; 90; 111)), which is an approximation to the full diagonalization as only a certain number of the lowest eigenstates and eigenenergies are calculated. Furthermore, these lowest states are not exact but the lower the eigenenergy the more accurate the approximation will be. Also enlarging the number of states calculated within a Lanczos procedure will emend the accuracy of the lower eigenstates and eigenenergies. The Lanczos algorithm is also called Exact Diagonalization in the literature which is the reason for the term full diagonalization we choose for standard direct methods. The restriction to only low-energy states is justified as we are interested in the ground state properties of the considered system for which the low-energy states account mostly.

To depict the simplification the Lanczos algorithm offers, we consider an 8 site Hubbard-cluster at half-filling without superconductivity. As the dimension of the Hilbertspace is given by the following expression

$$\dim(\mathcal{H}) = \binom{L_c}{N_{\uparrow}} \binom{L_c}{N_{\downarrow}} \quad (3.114)$$

(where N_{\uparrow} is the number of electrons with spin up while N_{\downarrow} is the number of electrons with spin down), the according Hilbertspace is of the dimension 4900, which means for a direct method a full diagonalization of a 4900×4900 matrix. By use of the Lanczos algorithm we only take for example the lowest 100 states into account, which recovers at least the low-energy physics very well.

3.4.1 Krylov space

The basic idea of the Lanczos method is the concept of invariant subspaces explained in the following. Assuming a $(N \times N)$ Hamilton matrix \mathbf{H} we consider a M -dimensional subspace \mathcal{G} spanned by the vectors $\{|g_i\rangle\}_{i=1,\dots,M}$ with $M < N$. \mathcal{G} will be called an invariant subspace of \mathbf{H} if

$$|\phi\rangle \in \mathcal{G} \longrightarrow \mathbf{H}|\phi\rangle \in \mathcal{G} \quad (3.115)$$

holds for any $|\phi\rangle$ of \mathcal{G} . As a special case, each eigenstate of \mathbf{H} represents an invariant subspace. With the definition of the $N \times M$ matrix \mathbf{G} whose columns are the vectors $\{|g_i\rangle\}_{i=1,\dots,M}$ we obtain

$$\begin{aligned} \mathbf{H}\mathbf{G} &= \left(\mathbf{H}|g_1\rangle \left| \mathbf{H}|g_2\rangle \right| \dots \left| \mathbf{H}|g_M\rangle \right. \right) \\ &= \left(\sum_{i=1}^M \bar{H}_{i1}|g_i\rangle \left| \sum_{i=1}^M \bar{H}_{i2}|g_i\rangle \right| \dots \left| \sum_{i=1}^M \bar{H}_{iM}|g_i\rangle \right. \right) = \mathbf{G}\bar{\mathbf{H}}, \end{aligned} \quad (3.116)$$

with the $M \times M$ matrix \bar{H}_{ij} . If we are able to solve the eigenvalue problem

$$\bar{\mathbf{H}}|\psi\rangle = \lambda|\psi\rangle, \quad (3.117)$$

a solution to the eigenvalue problem of \mathbf{H} can be constructed:

$$\mathbf{H}[\mathbf{G}|\psi\rangle] = \mathbf{G}\bar{\mathbf{H}}|\psi\rangle = \mathbf{G}\lambda|\psi\rangle = \lambda[\mathbf{G}|\psi\rangle] \quad (3.118)$$

This very important result means that eigenstates and eigenvalues of \mathbf{H} can be found by solving the eigenvalue problem of lower-dimensional matrix $\bar{\mathbf{H}}$.

The crucial point of finding an appropriate invariant subspace of \mathbf{H} to get the low-energy eigenstates of \mathbf{H} leads to the construction of the so-called Krylov space \mathcal{K}_M which is the linear span of the vectors

$$\{|\phi_0\rangle, \mathbf{H}|\phi_0\rangle, \mathbf{H}^2|\phi_0\rangle, \dots, \mathbf{H}^{M-1}|\phi_0\rangle\}, \quad (3.119)$$

with $|\phi_0\rangle$ a normalized random initial vector. Applying the hamiltonian \mathbf{H} to the above set of vectors renders an new set which are all elements of \mathcal{K}_M except the last one

$$\{\mathbf{H}|\phi_0\rangle, \mathbf{H}^2|\phi_0\rangle, \mathbf{H}^3|\phi_0\rangle, \dots, \mathbf{H}^M|\phi_0\rangle\}. \quad (3.120)$$

Next, we consider the last element of the set of vectors spanning the Krylov space and expand the initial vector into the eigenstates $\{|\Psi_i\rangle\}$ of \mathbf{H}

$$\begin{aligned} \mathbf{H}^{M-1}|\phi_0\rangle &= \mathbf{H}^{M-1} \sum_{i=0}^{N-1} \mu_i |\Psi_i\rangle = \sum_{i=0}^{N-1} \mu_i \epsilon_i^{M-1} |\Psi_i\rangle \\ &= \mu_0 \epsilon_0^{M-1} \left(|\Psi_0\rangle + \sum_{i=1}^{N-1} \frac{\mu_i}{\mu_0} \left(\frac{\epsilon_i}{\epsilon_0} \right)^{M-1} |\Psi_i\rangle \right). \end{aligned} \quad (3.121)$$

Assuming the initial vector to have a non-vanishing overlap with the exact ground state of \mathbf{H} ($\langle\Psi_0|\phi_0\rangle \neq 0$), the vector $\mathbf{H}^{M-1}|\phi_0\rangle$ converges to the ground state for large enough M as $|\epsilon_0| > |\epsilon_i|$. Hence, $\mathbf{H}^M|\phi_0\rangle$ is approximately proportional to $\mathbf{H}^{M-1}|\phi_0\rangle$ and the Krylov space \mathcal{K}_M an approximate invariant subspace of \mathbf{H} . If $\langle\Psi_0|\phi_0\rangle = 0$, the vector $\mathbf{H}^M|\phi_0\rangle$ converges to the lowest eigenstate of \mathbf{H} with which the initial vector has a non-vanishing overlap. As we are interested in ground-state properties, we have to omit initial vectors with $\langle\Psi_0|\phi_0\rangle = 0$. But in practical applications a random start vector obeys this condition virtually always. And, in addition, if informations about the ground state such as particle number or spin are available, it is advantageous to use initial states belonging to the subspace of these quantum numbers.

3.4.2 (Block-)Lanczos

After the theoretical considerations above, the practical construction of basis vectors spanning a Krylov space is explained in the following. With a given basis vector $|\phi_n\rangle$ of the Krylov space, we create a further orthonormal basis vector

$$|\tilde{\phi}_{n+1}\rangle = \mathbf{H}|\phi_n\rangle - \alpha_n|\phi_n\rangle - \beta_n|\phi_{n-1}\rangle, \quad (3.122)$$

$$|\phi_{n+1}\rangle = \frac{|\tilde{\phi}_{n+1}\rangle}{\| \tilde{\phi}_{n+1} \|}, \quad (3.123)$$

where the coefficients α_n and β_n are overlap integrals

$$\alpha_n = \langle \phi_n | \mathbf{H} | \phi_n \rangle, \quad (3.124)$$

$$\beta_n = \langle \phi_{n-1} | \mathbf{H} | \phi_n \rangle. \quad (3.125)$$

The coefficients β_n can be shown to be real numbers

$$\begin{aligned} \beta_n^* &= \langle \phi_n | \mathbf{H} | \phi_{n-1} \rangle = \langle \phi_n | \tilde{\phi}_n \rangle + \alpha_{n-1} \langle \phi_n | \phi_{n-1} \rangle + \beta_{n-1} \langle \phi_n | \phi_{n-2} \rangle \\ &= \| \tilde{\phi}_n \| \in \mathbb{R}. \end{aligned} \quad (3.126)$$

The resulting matrix $\bar{\mathbf{H}}$ represented in the Krylov basis is of a tridiagonal form

$$\bar{\mathbf{H}} = \begin{pmatrix} \alpha_0 & \beta_1 & & & & & \\ \beta_1 & \alpha_1 & \beta_2 & & & & \\ & \beta_2 & \alpha_2 & \ddots & & & \\ & & \ddots & \ddots & \ddots & & \\ & & & \ddots & \ddots & \ddots & \\ 0 & & & & \alpha_{M-2} & \beta_{M-1} & \\ & & & & \beta_{M-1} & \alpha_{M-1} & \end{pmatrix}. \quad (3.127)$$

Solving the eigenvalue problem $\bar{\mathbf{H}}|\psi_i\rangle = \lambda_i|\psi_i\rangle$ we obtain the approximated eigenstates $|\Phi_i\rangle$ of \mathbf{H} to an eigenvalue λ_i via

$$|\Phi_i\rangle = \mathbf{G}|\psi_i\rangle, \quad (3.128)$$

with \mathbf{G} the $N \times M$ matrix whose columns are the vectors $\{|\phi_i\rangle\}_{i=0,\dots,M-1}$. As discussed above the eigenvalues λ_i and eigenstates $|\psi_i\rangle$ converge to the exact eigenvalues ϵ_i and eigenstates $|\Psi_i\rangle$ for large M .

In contrast to the standard Lanczos algorithm the Block-Lanczos method uses $p > 1$ initial vectors which leads to the Block-Krylov space

$$\{|\phi_0^1\rangle, \dots, |\phi_0^p\rangle, \mathbf{H}|\phi_0^1\rangle, \dots, \mathbf{H}|\phi_0^p\rangle, \mathbf{H}^2|\phi_0^1\rangle, \dots, \mathbf{H}^2|\phi_0^p\rangle, \dots, \mathbf{H}^{M-1}|\phi_0^1\rangle, \dots, \mathbf{H}^{M-1}|\phi_0^p\rangle\}. \quad (3.129)$$

Similar to the standard Lanczos method the orthonormal basis will be produced iteratively. The important difference is in the occurrence of linear dependent vectors. In case of $p = 1$ this happens after $M + 1$ iterations wherefore the M preceding vectors are a complete orthonormal

4

Magnetic correlations in high- T_c superconductors

Two-particle excitations and their corresponding magnetic, charge, optical and pairing susceptibilities are fundamental for obtaining a microscopic understanding of the high- T_c cuprate superconductor physics, complementing single-particle (such as Angle-Resolved Photoemission-Spectroscopy (ARPES), etc.) experiments. A key example is provided by the magnetic excitations:

When entering the superconducting state, a resonant peak at the wave vector $\mathbf{q}_{AF} = (\pi, \pi)$ emerges in the cuprate compounds (34; 35; 36; 37; 38; 39). Being a universal feature also in electron-doped cuprates (43), this magnetic mode is a promising candidate for the *pairing glue*. This means a bosonic excitation which mediates a retarded pairing mechanism in contrast to an instantaneous mechanism via the exchange coupling J . The doping dependence of the resonance mode's frequency $\omega_{\text{res}}(\mathbf{q}_{AF})$ follows the doping dependence of T_c and, hence, further affirms theories which consider the resonance mode to be crucial for the mechanism of superconductivity.

As the resonance lies within the superconducting gap, it was proposed to identify this mode with a $S=1$ spin exciton. Apart from the peak at \mathbf{q}_{AF} INS experiments observed a downward and an upward *hourglass*-like dispersion in several hole-doped compounds (36), with the upward dispersion being strongly damped as it extends into the continuum of single spin-flip excitations. In case of electron-doped cuprates only the resonance peak is detected as an universal feature so far (43).

Besides the important question of a possible *pairing glue* a variety of experiments in the HTSC, such as ARPES, Optical and Tunneling Spectroscopies, have been interpreted as evidence of interactions of electrons with this mode (44; 45; 46). As a consequence, a theoretical description of cuprate superconductivity must include and explain also this prominent resonance

mode and its properties.

A spin excitonic bound state has previously been suggested on the basis of an itinerant picture, most frequently invoking a weakly correlated RPA-like form of the dynamic spin susceptibility (e.g. Ref. (70)). As a weak-coupling form it leads to a Fermi-liquid like $\chi(\mathbf{q}, \omega)$, which is in contrast to some of the anomalous dynamics found in neutron scattering experiments (34; 35; 36; 37; 38; 39). On the other hand, when the two-particle interaction and the superconducting gap are used as adjustable parameters, it qualitatively accounts for the mode behavior near optimal and overdoped regimes (70). In the following chapter we apply our two-particle approach developed in section 3.2 to the one-band Hubbard model to gain information about the magnetic spectrum. As the *hourglass* structure is only observed in hole-doped cuprates we focus our investigation on this part of the phase diagram. To render a consistent picture we first analyze the antiferromagnetic phase which also serves as a test case for our new approach. For this reason section 4.2 contains a detailed discussion about finite-size effects. The main results are then provided in section 4.3, where the superconducting phase is explored and related to experimental findings. But first of all, in section 4.1 we briefly review the phase diagram and results on one-particle excitation of the Hubbard model using the VCA. This review mainly follows the publications (61; 64; 65; 66; 67; 68; 69; 3). Also the choice of the reference clusters will be discussed (section 4.1.1). The present chapter closes with section 4.4 providing a discussion of the meaning and importance of the self-consistently obtained controlling constant α introduced in section 3.2.4.

We use the one-band Hubbard model with $t' = -0.3t$ and $U = 8t$ as standard values for the description of HTSC cuprates and we set $t = 1$ to fix the energy scale. Since the grand canonical ensemble is used, all one-particle energies are the difference to the chemical potential. A broadening of $0.05t$ is used to display the results.

4.1 Preliminaries to the Hubbard model within the VCA

It has been shown that the VCA correctly reproduces salient features of the one-particle properties of the HTSC (61; 64; 65; 66; 67; 68; 69; 3). First of all, we inspect the hole-doped phase diagram (Fig. 4.1) for the two-dimensional one-band Hubbard model calculated in the VCA by use of the $\sqrt{10} \times \sqrt{10}$ cluster. It is plotted the antiferromagnetic as well as the superconducting order parameter against the doping. For a better orientation the phase diagram is given in different colors. At small doping an antiferromagnetic + superconducting phase emerges, in which both the antiferromagnetic as well as the superconducting order ($m > 0$ and $\Delta > 0$) microscopically and coherently coexist (*blue* regime). A homogeneous phase with a pure superconducting order ($m = 0$ and $\Delta > 0$) is obtained for larger dopings (*green* regime). In between a *red* regime occurs, i.e. a phase separation region, where the homogeneous solutions antiferromagnetism + superconductivity and superconductivity become unstable and the system prefers to separate into a mixture of two densities n_1 and n_2 . In this regime there

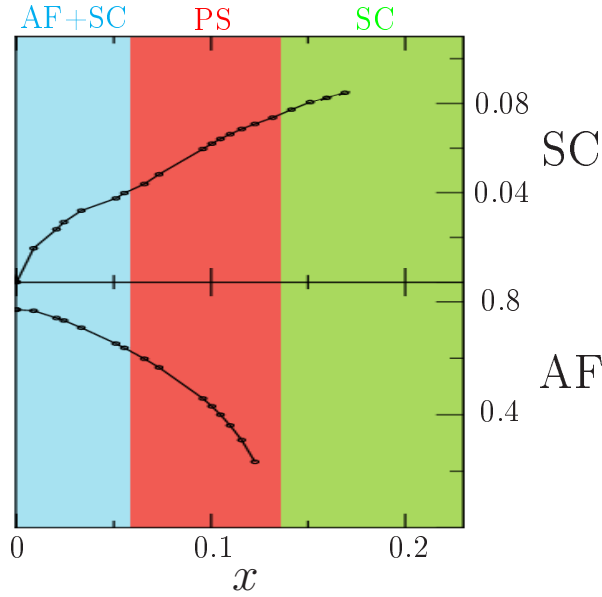


Figure 4.1: Phase diagram of the hole-doped Hubbard model obtained from a VCA calculation using the $\sqrt{10} \times \sqrt{10}$ cluster (taken from (2)).

is tendency towards the formation of inhomogeneities, such as stripes, checkerboard patterns, etc.. At half-filling the system shows an pure antiferromagnetic phase. Hence, the Hubbard model in the VCA recovers both the antiferromagnetism and the superconductivity. Although not shown here, we like to mention that the VCA calculations in the Hubbard model also account for the electron-hole asymmetry in the phase diagram (67). This means the much smaller doping range of antiferromagnetism at hole-doping compared to electron doping.

As a further very important outcome the VCA treatment of the Hubbard revealed the prominent dichotomy of nodal and antinodal superconducting gaps discovered in Raman (77; 78) and ARPES (79; 80; 81) experiments (3). This will be detailed and compared to our results on the Raman response in chapter 5.

4.1.1 Choice of the reference clusters

All the clusters considered in the present thesis are depicted in Fig. 4.2. The choice which of these should be employed as a reference cluster for a VCA calculation is a very subtle one. Principally, it seems plausible to use the largest cluster that can be calculated with respect to a given CPU power as well as main memory. Unfortunately, in practical computations we are restricted to cluster sizes of about 10 sites which is not large enough to obtain converged results. It is meant that the outcome of a VCA calculation is not independent of the cluster size and geometry. This problem can only be handled by an intelligent choice of the underlying cluster depending on the phase that should be analyzed. The phase diagram in Fig. 4.1 is obtained with the $\sqrt{10} \times \sqrt{10}$ cluster but is qualitatively the same for the 2×2 and 4×2

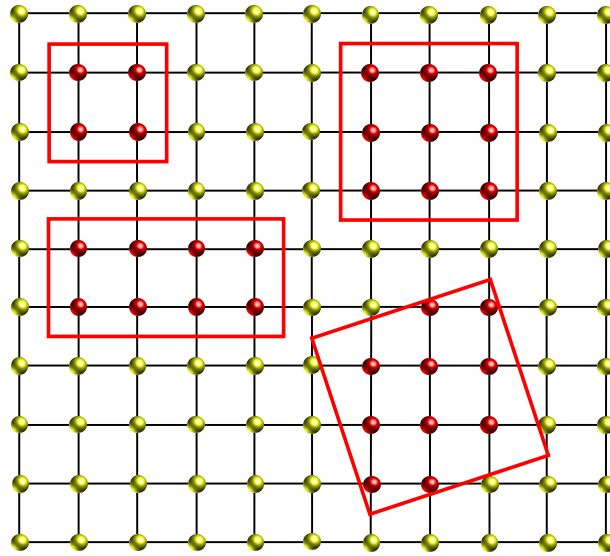


Figure 4.2: Geometry of the clusters used in our calculations: 2×2 , 3×3 , 4×2 and $\sqrt{10} \times \sqrt{10}$

clusters. Hence, the order parameter seems to be robust against the cluster size. But if some more specific details of the superconducting phase are investigated these clusters with an even site turn out to be not appropriate. Such details are for example the mentioned gap dichotomy discussed in chapter 5 and (3) or the magnetic correlations presented in this chapter. For these issues the 3×3 is employed and works best. The deeper reason is twofold and is based on the cluster size and geometry:

It turns out that even at relative large doping $x > 0.1$ the reference clusters with an even number of sites are only at about $x \simeq 0.05$ doping. And as the correlated physics stems from the cluster level, it is obvious, that this discrepancy between the doping of the physical system and the reference clusters make these even site clusters inappropriate. In case of 3×3 sites the cluster shows an intrinsic doping of $x = \simeq \frac{1}{9}$. The reason is that the ground state of the Hubbard model tends to be in the $S^z = 0$ state which is only possible for an even number of electrons, i.e. 8 electrons for the 3×3 cluster. Hence, the dopings of the physical system is for $x > 0.1$ comparable to the doping of the reference system. The same argumentation rules out the 3×3 clusters for the description at small doping.

The other reason which favors the 3×3 cluster for the superconducting phase is its geometry. The even site 2×2 and 4×2 clusters are adequate for the description of antiferromagnetism since they allow for a antiferromagnetic symmetry breaking. But these clusters tend to overestimate the antiferromagnetic correlations even in the pure superconducting phase. The 3×3 overcomes this problem for reason of the odd number of sites per dimension. Again, this argumentation rules out the 3×3 clusters for the description of antiferromagnetism at small doping.

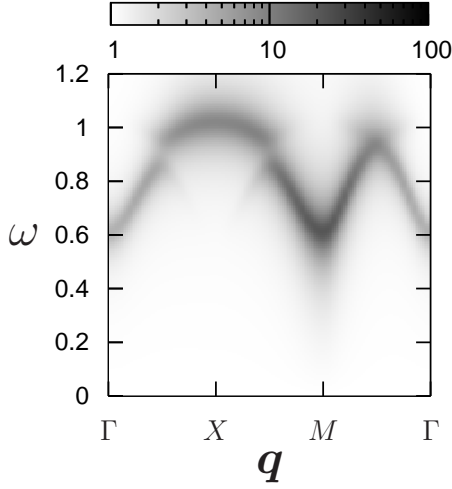


Figure 4.3: Density plot of $\text{Im}\chi^\pm(\mathbf{q}, \omega)$ at half-filling in the antiferromagnetic phase using the 2×2 cluster.

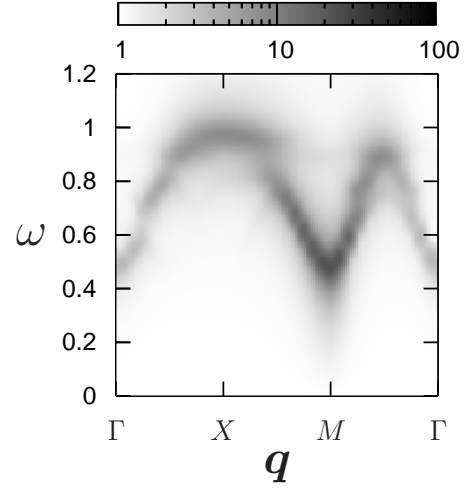


Figure 4.4: Density plot of $\text{Im}\chi^\pm(\mathbf{q}, \omega)$ at half-filling in the antiferromagnetic phase using the 4×2 cluster.

The dependence of the employed cluster can be seen in our results. Comparison of Fig. 4.13 with the Figs. 4.21,4.22 discloses the even site clusters to be inappropriate to reveal the magnetic structures in the pure superconducting phase. Rather, slight remnants of the magnonic dispersion are visible, at least in the 2×2 case. The reason is the small cluster doping and the cluster geometry, both overestimating antiferromagnetic correlations. In addition, the small size of the 2×2 cluster results in a certain mean-field character of the cluster approach which also overestimates antiferromagnetic correlations.

We also mention that clusters should be preferred which conserve the rotational symmetry of the original lattice as the 2×2 and 3×3 clusters do. This can be clearly seen in the Figs. 4.4,4.10,4.5,4.11. compared to Figs. 4.3,4.9,4.7. The latter ones showing the 2×2 results provide a much more pronounced magnonic dispersion.

4.2 Antiferromagnetic phase

In this section the *blue* regime in Fig. 4.1 is explored by use of the even site clusters depicted in Fig. 4.2. First, we focus on the half-filled case, i.e. in the pure antiferromagnetic phase. Fig. 4.3 displays the result for the imaginary part of the transverse magnetic susceptibility $\text{Im}\chi^\pm(\mathbf{q}, \omega)$ on the basis of the 2×2 cluster. The dispersion follows the usual antiferromagnetic spin wave pattern with the maximum weight around $\mathbf{q}_{AF} = (\pi, \pi)$. Here, a gap appears, which rapidly and continuously diminishes with increasing cluster sizes as indicated by the Figs. 4.4 and 4.5 showing the results for the 4×2 and $\sqrt{10} \times \sqrt{10}$ cluster, respectively. Hence, this gap is identified as a finite-size effect proved by Fig. 4.6 displaying the imaginary part of the

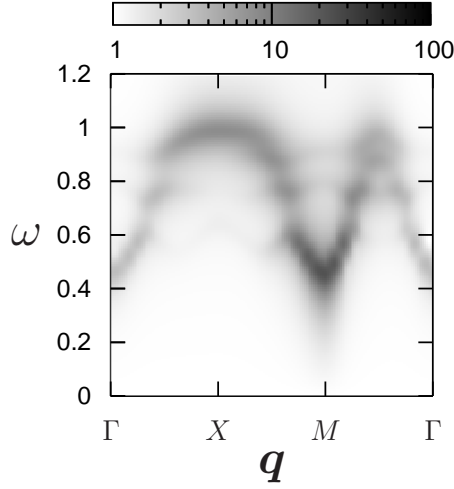


Figure 4.5: Density plot of $\text{Im}\chi^\pm(\mathbf{q}, \omega)$ at half-filling in the antiferromagnetic phase using the $\sqrt{10} \times \sqrt{10}$ cluster.

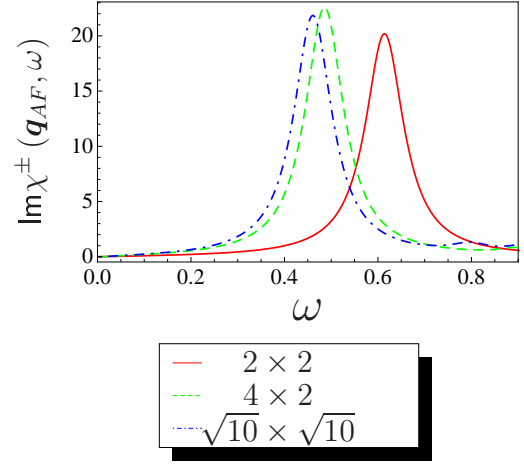


Figure 4.6: Plot of $\text{Im}\chi^\pm(\mathbf{q}_{AF}, \omega)$ at half-filling using various clusters.

transverse susceptibility at the antiferromagnetic wave vector $\text{Im}\chi^\pm(\mathbf{q}_{AF} = (\pi, \pi), \omega)$ for the three different cluster sizes. Clearly, the finite-size gap closes continuously as a function of the cluster size.

Upon doping the mixed antiferromagnetic + superconducting phase is entered. The corresponding 2×2 result for $\text{Im}\chi^\pm(\mathbf{q}, \omega)$ at $x = 0.06$ doping is given in the Fig. 4.7 revealing the finite-size gap being obviously diminished. To further analyze this doping dependence we examine the 2×2 cluster $\text{Im}\chi^\pm(\mathbf{q}_{AF} = (\pi, \pi), \omega)$ at three different dopings, i.e. $x = 0.0$, $x = 0.04$ and $x = 0.06$. Indeed, Fig. 4.8 displays a rapid and continuous closure of the gap. We attribute this to a screening effect, which renders the two-particle vertex Γ significantly more short-ranged, i.e. more local. This means that it can accurately be extracted from the diagonalization of already small clusters.

Further support for this argument is provided by the analysis of $\text{Im}\chi^\pm(\mathbf{q}, \omega)$ using the 2×2 , 4×2 and $\sqrt{10} \times \sqrt{10}$ at small ($x = 0.04$) doping. The corresponding results for $\text{Im}\chi^\pm(\mathbf{q}, \omega)$ at $x = 0.04$ doping are given in the Figs. 4.9, 4.10 and 4.11 which reveal the finite-size effects being of minor importance compared to the half-filled case. The gap is clearly smaller for all cluster sizes and, furthermore, the dependence of the gap size on the cluster size is even smaller as depicted in Fig. 4.12. Here, the $\sqrt{10} \times \sqrt{10}$ breaks ranks which we definitely address to the shape of the cluster that does not conserve the rotational symmetry of the original lattice. As already discussed in section 4.1.1 this broken rotational symmetry has also an effect on the shape of the dispersion. Fig. 4.11 exemplifies this impressively.

Our two-particle approach also allows for a realistic calculation of the spin-flip electron-hole continuum, as the fully dressed one-particle propagators enter the $\chi_0^{\pm, VCA}(q, \omega)$ (see

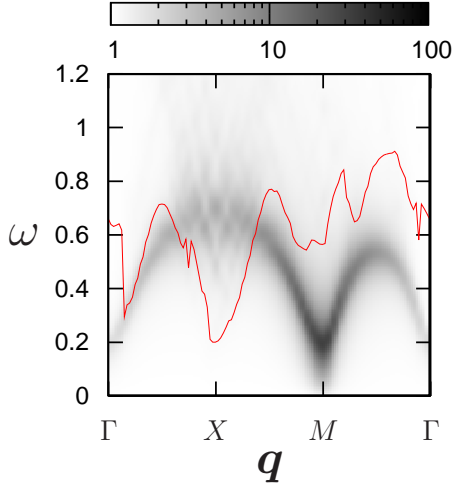


Figure 4.7: Density plot of $\text{Im}\chi^\pm(\mathbf{q}, \omega)$ at $x = 0.06$ doping in the mixed antiferromagnetic + superconducting phase using the 2×2 cluster. The red line denote the lower boundary of the spin-flip electron-hole continuum (extracted from Eq. (3.69)).

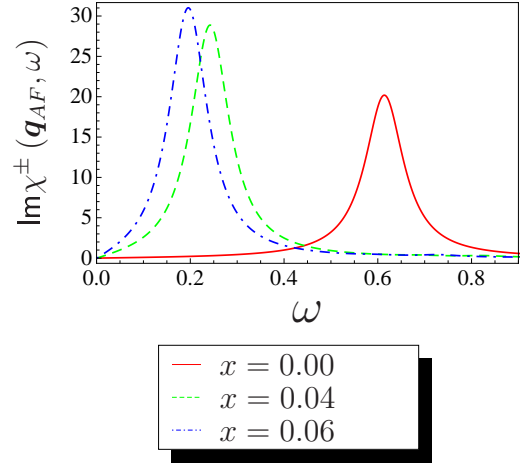


Figure 4.8: Plot of $\text{Im}\chi^\pm(\mathbf{q}_{AF}, \omega)$ at various dopings using the 2×2 cluster.

Eq. (3.64)). Indeed, Fig. 4.9 and Fig. 4.7 display the magnonic dispersion diving into this continuum around the X -point and getting decayed. In addition, the latter figure depicts as the red line the lower boundary of the continuum extracted from $\chi_0^{\pm, VCA}(q, \omega)$. To find this borderline, we sweep at each of the \mathbf{q} -points along the ω axis starting from $\omega = 0$ until $\chi_0^{\pm, VCA}(q, \omega)$ adopts a certain threshold. Finding the appropriate threshold for the Lorentzian declining peaks is, of course, not straight forward and requires some trying. It turns out that a value of about 0.005 for the threshold works best.

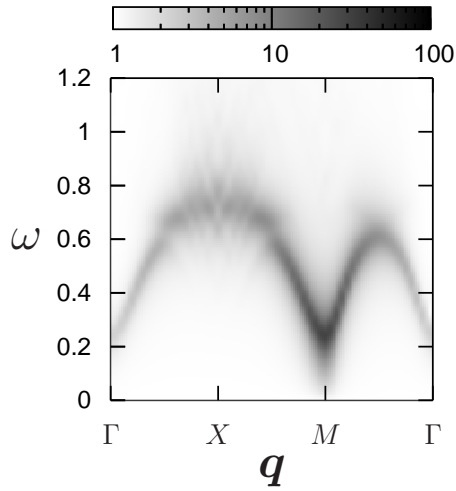


Figure 4.9: Density plot of $\text{Im}\chi^\pm(\mathbf{q}, \omega)$ at $x = 0.04$ doping in the mixed antiferromagnetic + superconducting phase using the 2×2 cluster.

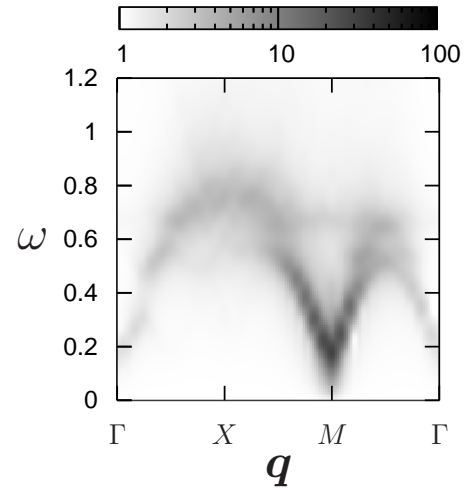


Figure 4.10: Density plot of $\text{Im}\chi^\pm(\mathbf{q}, \omega)$ at $x = 0.04$ doping in the mixed antiferromagnetic + superconducting phase using the 4×2 cluster.

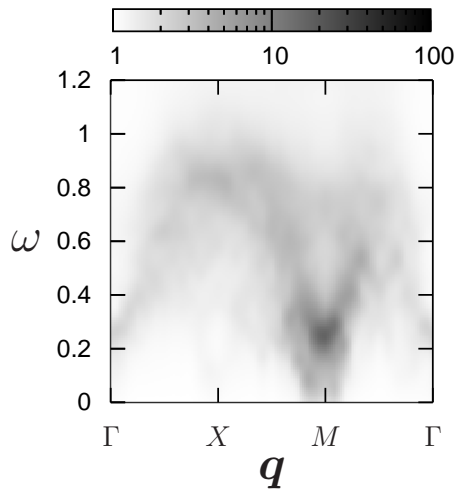


Figure 4.11: Density plot of $\text{Im}\chi^\pm(\mathbf{q}, \omega)$ at $x = 0.04$ doping in the mixed antiferromagnetic + superconducting phase using the $\sqrt{10} \times \sqrt{10}$ cluster.

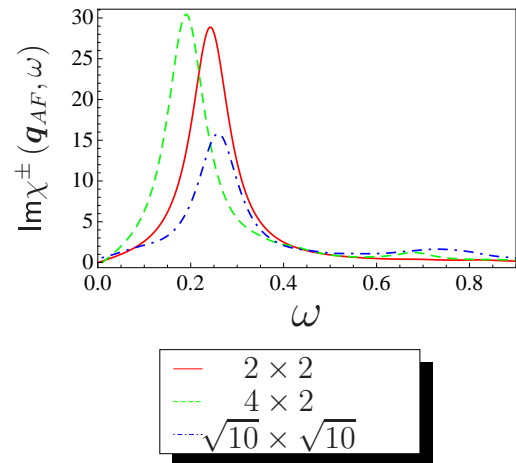


Figure 4.12: Plot of $\text{Im}\chi^\pm(\mathbf{q}_{AF}, \omega)$ at $x = 0.04$ doping using various clusters.

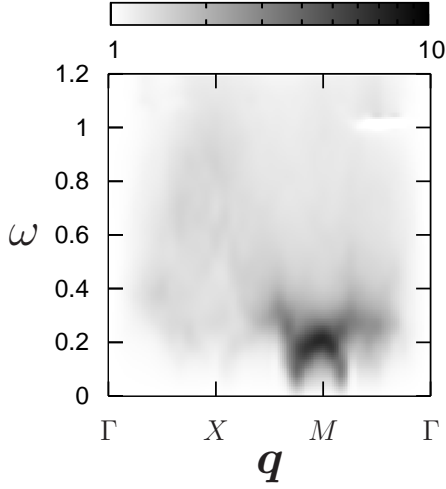


Figure 4.13: Density plot of $\text{Im}\chi^\pm(\mathbf{q}, \omega)$ at $x = 0.18$ doping in the superconducting phase using the 3×3 cluster.

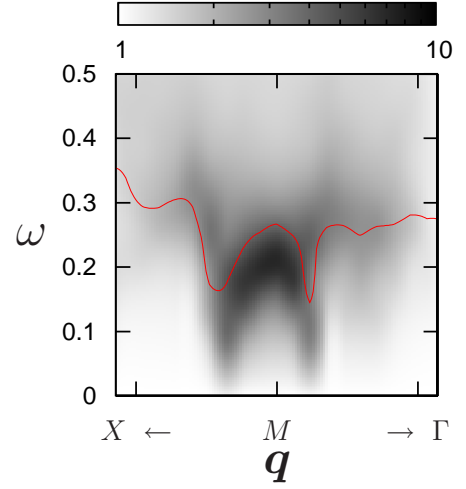


Figure 4.14: Same as 4.13 but focusing on the hourglass structure. The red line denote the lower boundary of the spin-flip electron-hole continuum (extracted from Eq. (3.69)).

4.3 Superconducting phase

We enter in this section the most interesting, namely the pure superconducting state and its magnetic response properties. Fig. 4.13 contains a two-dimensional intensity plot of our results (using a 3×3 reference cluster) for the imaginary part of the transversal magnetic susceptibility $\text{Im}\chi^\pm(\mathbf{q}, \omega)$ at $x=0.18$ doping. The only spin spectral weight appears around the M point on an energy scale of about 0.2 yielding the celebrated resonance mode. Focusing on this resonance in Fig. 4.14 it is also displayed the lower boundary of the spin-flip electron-hole continuum extracted from $\chi_0^{\pm, VCA}(\mathbf{q}, \omega)$ (see the latter section for explanation). Hence, this figure reveals the resonance emerging in the superconductivity-induced gap of ($S=1$) electron-hole excitations when entering this superconducting doping regime. We note, that like in the experiments (see, in particular, Ref. (36)), the resonance has an *hourglass* shape with its maximum spectral weight confined to a region close to $M \equiv \mathbf{q}_{AF} = (\pi, \pi)$ and a dramatic intensity reduction around $\simeq 0.8(\pi, \pi)$. Therefore, our results impressively recover the experimentally found prominent *hourglass* structure.

Our results can indeed consistently be summarized along the experimental findings of Ref. (36). As shown in Fig. 4.15, again in an intensity plot, we find for the doping ($x=0.18$) considered in Fig. 4.13 and 4.14 a typical Fermi surface closed around (π, π) . Fig. 4.16 plots the corresponding spin-flip electron-hole continuum along the Brillouin zone diagonal, obtained from $\chi_0^{\pm, VCA}(\mathbf{q}, \omega)$. Only collective modes (i.e. $S=1$, spin-flip electron-hole excitations) below the electron-hole continuum (i.e. below the red line in Fig. 4.16 and 4.14) can actually be

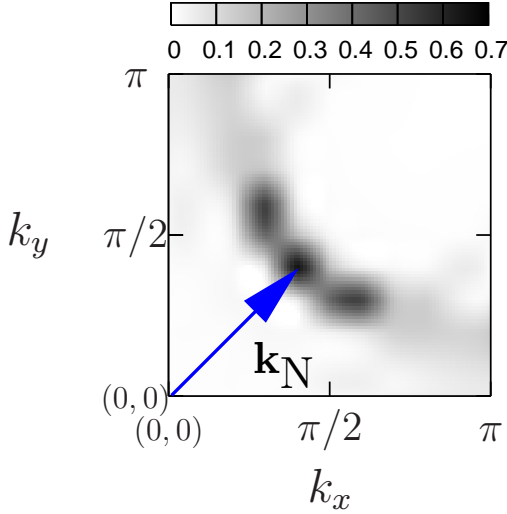


Figure 4.15: Density plot of the low-energy spectral weight obtained from the corresponding VCA calculation for the one-particle Green's function displaying the Fermi surface with the nodal scattering vector $2\mathbf{k}_N \simeq 0.8(\pi, \pi)$.

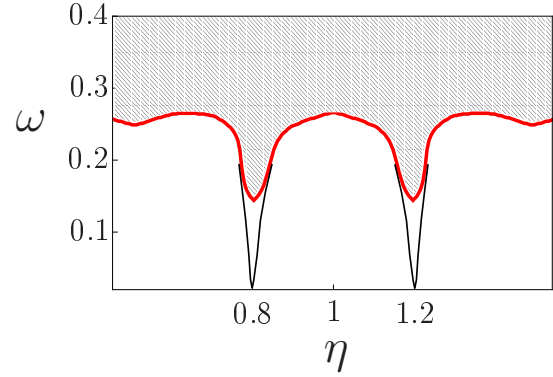


Figure 4.16: Lower boundary of the spin-flip electron-hole continuum in the superconducting phase at $x = 0.18$ doping. The plot follows a path along $\mathbf{q} = \eta(\pi, \pi)$ revealing a minimum at $2\mathbf{k}_N \simeq 0.8(\pi, \pi)$. The red line is extracted from Eq. (3.69), while the hatched area is only for reason of visualization.

detected, because modes within the continuum are Landau damped and, thus, weak. This electron-hole continuum corresponds to Fig. 4b in Ref. (36). The continuum threshold exhibits also in our case a pronounced minimum in the vicinity of the wave vector $2\mathbf{k}_N \simeq 0.8(\pi, \pi)$, which corresponds to scattering between nodes of the d-wave gap function (Fig. 4.15 gives just one quadrant of the Brillouin zone). The minimum in our calculation is, however, not so steep as in the idealistic situation in Fig. 4c of Ref. (36). The reason is the broadening of $\eta = 0.05t$ used in our calculations.

We would like to emphasize that a similar picture has been put forward in RPA-like descriptions of the neutron resonance (see, for example, Ref. (70)). Here, however, the d-wave gap amplitude as well as the magnitude of the effective two-particle interaction are parameters. They are used to reproduce the experimental energy positions of the resonance mode at (π, π) and the electron-hole threshold around $0.8(\pi, \pi)$ in (70). There is an additional difference to our parameter-free theory: we find in Fig. 4.14 the resonant magnetic excitation to have also an upward dispersing branch originating at \mathbf{q}_{AF} . In Ref. (70) this branch is missing. Instead, it appears with very little weight only at momenta less than $\mathbf{k}_N \simeq 0.8(\pi, \pi)$

Figs. 4.17, 4.18 and 4.19 give additional comparisons of our calculations with salient features

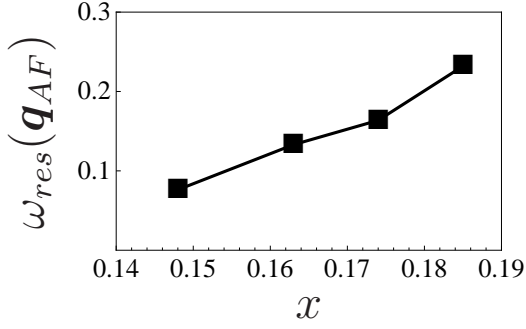


Figure 4.17: $\omega_{\text{res}}(\mathbf{q}_{AF})$ as a function of doping.

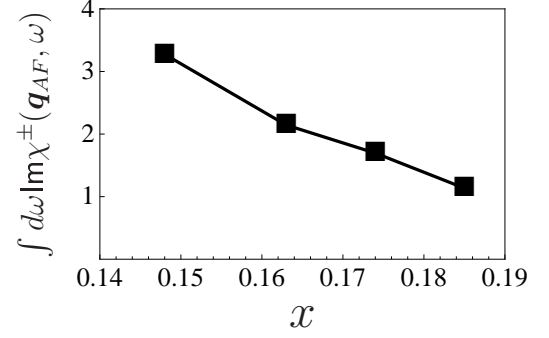


Figure 4.18: Doping dependence of the ω -integrated spin-spectral weight at \mathbf{q}_{AF} .

of the INS experiments in underdoped $YBa_2Cu_3O_{6+x}$ (112):

Fig. 4.17 exhibits the energy of the magnetic resonance peak in the underdoped regime, which increase as a function doping. This trend is also observed in the INS experiments as showed in the Fig. 11.c) of Ref. (112).

The energy-integrated spin spectral weight at \mathbf{q}_{AF} obtained at various dopings in the superconducting regime given in Fig. 4.18 follows again the experimental findings displayed in Fig. 11.b) of Ref. (112).

Finally, Fig. 4.19 reproduces the difference of the transversal magnetic susceptibility at \mathbf{q}_{AF} in the superconducting and *normal* states at $x = 0.17$ doping $\text{Im}\Delta\chi^\pm(\mathbf{q}_{AF}, \omega)$. The comparison with Fig. 10.b) of (112) can only be a qualitative one, since we are at $T=0$, and our *normal* state solutions are done without allowing for U(1) symmetry breaking in the variational procedure. Hence, we employ this paramagnetic state to *simulate* the *normal* state occurring for $T > T_c$. The corresponding result is displayed in Fig. 4.20 and reveals the resonance mode to be vanished except for slight remnants. Nevertheless, qualitatively, our calculations reproduce the experimental finding, that the enhancement of the spectral weight around the resonance peak energy is accompanied by a reduction of the spectral weight over a limited energy range both above and below $\omega_{\text{res}}(\mathbf{q}_{AF})$.

We need to provide some explanation concerning the comparison of the doping dependence in our results with the experimental findings. The doping in the experiments does only correspond to our theoretical doping in the sense that both are at a typical underdoped situation. Although we provide results up to $x = 0.18$ doping the reference cluster is still at $x \leq 0.15$. This is again the already discussed discrepancy between the doping of the physical and the reference system (see section 4.1.1). Hence, our results in the superconducting phase incorporate the correlated physics of a cluster in the underdoped regime.

In summary, the calculated doping dependence of $\omega_{\text{res}}(\mathbf{q}_{AF})$, the *hourglass* dispersion of the resonance and its rapid decrease around a characteristic wave vector $2\mathbf{k}_N \simeq 0.8(\pi, \pi)$, which coincides with the distance between nodal points on the Fermi surface, are qualitatively consis-

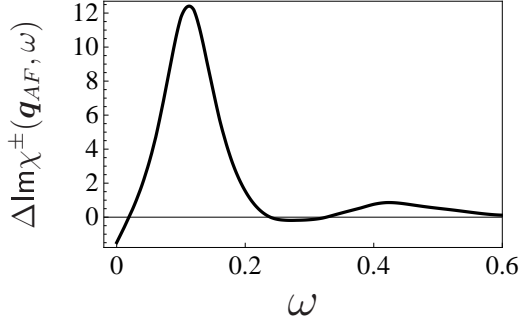


Figure 4.19: Difference between $\text{Im}\chi(\mathbf{q}_{AF}, \omega)$ in the superconducting and normal states at $x = 0.17$ doping.

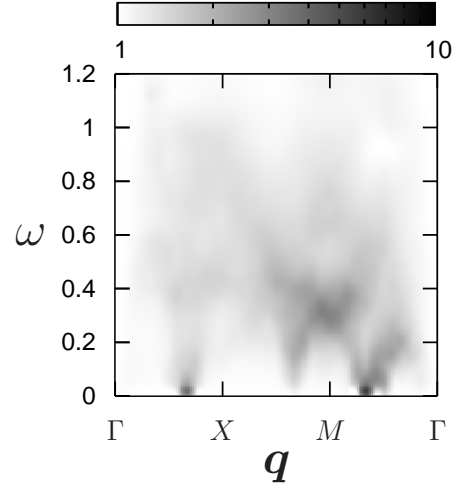


Figure 4.20: Density plot of $\text{Im}\chi^\pm(\mathbf{q}, \omega)$ at $x = 0.18$ doping in the normal state using the 3×3 cluster.

tent with the experiment and support the $S=1$ magnetic exciton scenario. Some of these results have been obtained before in weak-coupling, however, by fitting the two-particle interaction to the experiment. In contrast, our results are obtained in the appropriate strong-correlation regime and contain no adjustable parameters. Thus, when taken together with earlier results on the phase diagram and single-particle excitations, this constitutes a rather strong support for Hubbard model description of HTSC.

This section closes with the imaginary part of the transversal magnetic susceptibility $\text{Im}\chi^\pm(\mathbf{q}_{AF}, \omega)$ in the superconducting phase using the 2×2 and $\sqrt{10} \times \sqrt{10}$ cluster. The corresponding results are given Fig. 4.21 and Fig. 4.22, respectively. For the reasons explained in section 4.1.1, these even site clusters fail to describe the magnetic properties in the superconducting phase. Rather, there are remnants of the antiferromagnetic correlation visible, at least in case of the 2×2 cluster which strongly overestimates these.

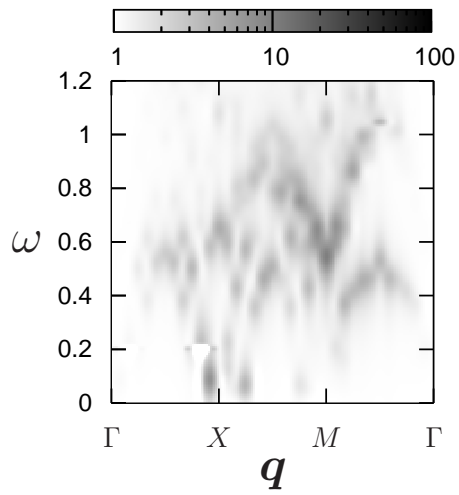


Figure 4.21: Density plot of $lm\chi^\pm(\mathbf{q}, \omega)$ at $x = 0.15$ doping in the superconducting phase using the 2×2 cluster.

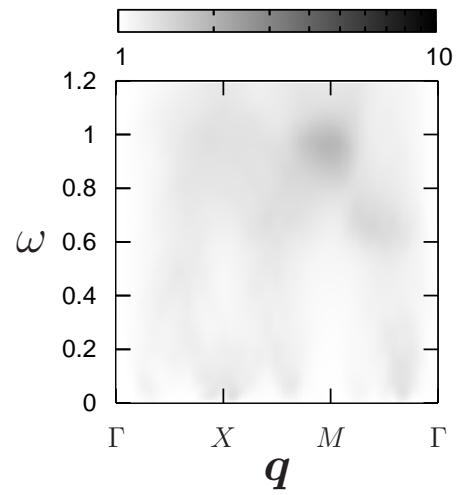


Figure 4.22: Density plot of $lm\chi^\pm(\mathbf{q}, \omega)$ at $x = 0.15$ doping in the superconducting phase using the $\sqrt{10} \times \sqrt{10}$ cluster.

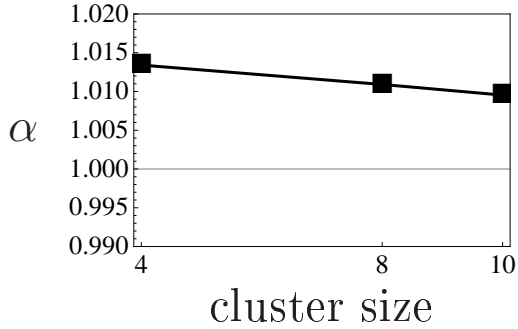


Figure 4.23: Dependence of the controlling constant on the cluster size at half-filling.

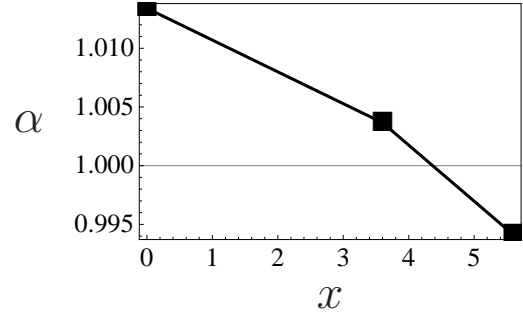


Figure 4.24: Doping dependence of the controlling constant α for the 2×2 cluster.

4.4 Controlling constant α

The self-consistently obtained controlling constant α introduced in section 3.2.4 serves as a fine-tuning of the effective vertex Γ_{eff} as well as a quality indicator for our two-particle approach. The underlying assumption of this approach and also the VCA is a relative local vertex, respectively self-energy. Only then, we are allowed to employ already small clusters for the calculation of these quantities. The constant α can be consulted to judge the justification of the locality assumption. In case of a constant α deviating only small from $\alpha = 1$ the sumrule is fulfilled with nearly no fine-tuning. This hints at a justification of our cluster approach. And, indeed, Tab. 4.1 reveals the values of α being absolutely close to $\alpha = 1$ and deviating only of the order of 1% for the calculations in the antiferromagnetic and mixed antiferromagnetic + superconducting phase presented in section 4.2.

	2×2	4×2	$\sqrt{10} \times \sqrt{10}$
$x = 0.00$	1.01	1.01	1.01
$x = 0.04$	1.00	1.00	1.00
$x = 0.06$	0.99	—	—

Table 4.1: Values of the controlling constant α for clusters and dopings discussed in section 4.2.

Fig. 4.23 renders the constant α continuously decreasing towards $\alpha = 1$ as a function of increasing cluster size at half-filling. This further supports our two-particle approach being controlled by the cluster size. The doping dependence of α by use of the 2×2 cluster is given in Fig. 4.24. We discover the value of α decreasing continuously with increasing doping. Interestingly, it decreases even below $\alpha = 1$. This behavior holds also in the superconducting phase using the 3×3 cluster discussed in section 4.3, for which we find values of $\alpha \simeq 0.95$, while in the paramagnetic phase at the same doping and cluster we find mostly $\alpha \simeq 0.92$ (see Tab. 4.2). These values are still close enough to $\alpha = 1$ to justify our two-particle approach.

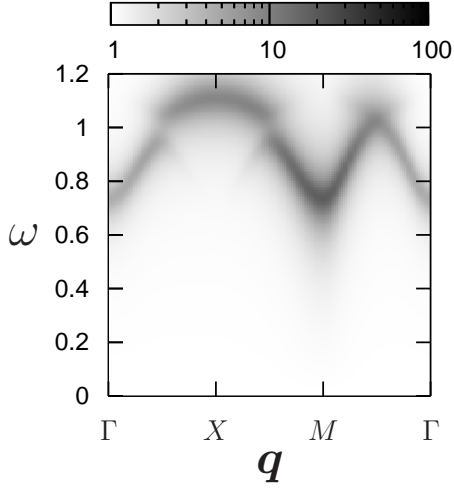


Figure 4.25: Density plot of $lm\chi^\pm(\mathbf{q}, \omega)$ at half-filling in the antiferromagnetic phase using the 2×2 cluster with a fixed $\alpha = 1$.

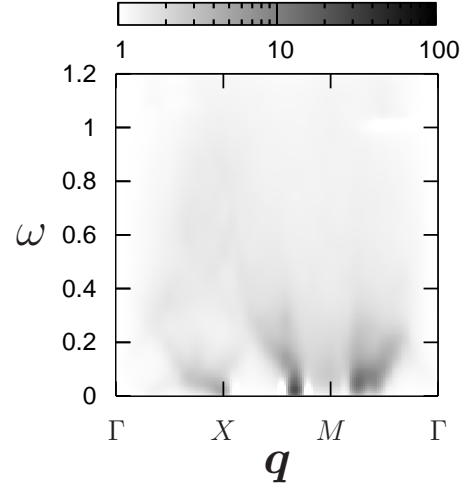


Figure 4.26: Density plot of $lm\chi^\pm(\mathbf{q}, \omega)$ at $x = 0.18$ doping in the superconducting phase using the 3×3 cluster with a fixed $\alpha = 1$.

With a value of $\alpha = 0.69$ at $x = 0.15$ doping the $\sqrt{10} \times \sqrt{10}$ breaks ranks which we address to the shape and doping of the cluster being improper to render the magnetic properties of the system in the superconducting phase as already discussed in section 4.1.1. Interestingly, the value of $\alpha = 0.88$ for the 2×2 at $x = 0.15$ doping is not such bad although the calculations do not render the correct magnetic spectrum.

	3×3	$3 \times 3, sc = 0$	2×2	$\sqrt{10} \times \sqrt{10}$
$x = 0.15$	0.96	0.88	0.88	0.69
$x = 0.16$	0.96	0.92	—	—
$x = 0.17$	0.95	0.92	—	—
$x = 0.18$	0.93	0.92	—	—

Table 4.2: Values of the controlling constant α for clusters, dopings and phases discussed in section 4.3.

4.4.1 Results with $\alpha = 1$

The importance of α as a fine-tuning of the effective vertex Γ_{eff} can easily be analyzed by setting $\alpha = 1$ in our calculations. First, the effect on the magnetic structures in the antiferromagnetic phase is inspected in Fig. 4.25 in comparison with Fig. 4.3 displaying the results with the self-consistently determined α . The overall dispersion is nearly unchanged compared to the calculation with the α self-consistently determined. Only the finite-size gap is slightly reduced. Further investigations show, that $\alpha > 1$ leads to a slight reducing of the finite-size

gap while $\alpha < 1$ lets the finite-size gap slightly increase.

In the superconducting phase the controlling constant adopts unlike more importance since it turns out that the *hourglass* structure is much more sensitive to the change in Γ_{eff} effected by α . Fig. 4.26 displays the corresponding $\alpha = 1$ result revealing the *hourglass* completely vanished (compare to Fig. 4.13). Hence, to obtain the sophisticated small structures concerning the resonance mode at small energy scales it is absolutely necessary to include the constant α for the fine-tuning of Γ_{eff} .

5

Raman response in high- T_c superconductors

Raman (77; 78) and ARPES (79; 80; 81) experiments recently revealed a quite different behavior of the superconducting gap of HTSC cuprates near the nodal $(\pi/2, \pi/2)$ compared to the antinodal point $(\pi, 0)$. The gap was found to increase with decreasing doping at the antinodal point which, previously, was believed to be the generic doping dependence of the superconducting gap (113; 114). However, near the nodal point the gap displays an even qualitatively different doping dependence, where the gap decreases with decreasing doping. While these experiments were so far interpreted as being due to two physical distinct mechanisms, VCA calculations showed, that this phenomenon can naturally be explained within the Hubbard model as a different doping dependence of the spin-fluctuation mediated pairing strength (3). In order to shed more light on this question of the gap dichotomy, we analyze the doping dependence of the superconducting gap in yet another approach, i.e. the Raman response.

Employing the technique described in section 3.3 allows us to work out the gap features in the Raman response. Using the B1g and B2g symmetries we can focus on the antinodal (B1g) and nodal (B2g) region of the Brillouin zone. We also analyze the Raman response in the paramagnetic phase to gain information about the *normal* state pseudogap observed in the HTSC cuprates at $T > T_c$. This will be related to the results derived in the superconducting phase. In addition, the question of an origin of the gap in the superconducting phase apart from superconductivity is addressed by switching off the anomalous part of the self-energy $\Sigma^{SC}(\omega) = 0$ in our calculation.

We use the one-band Hubbard model with $t' = -0.3t$ and $U = 8t$ as standard values for the description of HTSC cuprates and we set $t = 1$ to fix the energy scale. Since the grand canonical ensemble is used, all one-particle energies are the difference to the chemical potential. Our main interest is in properties related to superconductivity, wherefore we employ the 3×3

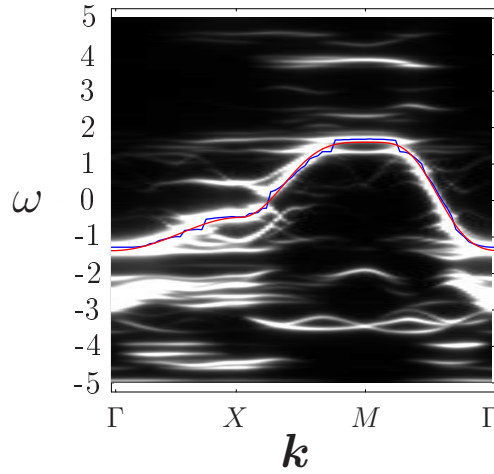


Figure 5.1: Exemplary plot of the spectral function calculated within the VCA at $x = 0.11$ hole-doping in the superconducting phase (white areas mean higher spectral weight). blue: numerically found quasi-particle dispersion ; red: fitted tight-binding dispersion up to 4th nearest neighbors

cluster for our calculations like we do in section 4.3. A broadening of $0.04t$ is used to display the results.

5.1 Raman vertex in the effective mass approximation

First, Fig. 5.1 exemplifies the one-particle spectral-function as a density plot with the numerically found dispersion as the blue curve and the fitted tight-binding dispersion up to 4th nearest neighbors as the red curve at $x = 0.11$ hole-doping in the superconducting phase. More generally, Fig. 5.2 shows the doping dependence of the fit-parameters at six different fractions of hole-doping from $x = 0.07$ to $x = 0.17$, all in the superconducting regime. To compare, Fig. 5.3 yields the doping dependence in the paramagnetic phase at five different fractions of hole-doping from $x = 0.06$ to $x = 0.12$.

Given the fit-parameters we are able to evaluate Eq. 3.112 and 3.113 for obtaining the Raman vertex in the effective mass approximation. Density plots of the squared vertex-functions $(\gamma^\nu(\mathbf{k}))^2$ at $x = 0.11$ hole-doping in the superconducting phase are shown in Fig. 5.4, with the vertices in the right column are obtained from calculations based on the dispersion up to the 4th nearest neighbor hopping while for the ones in the left column the dispersion was limited up to next-nearest neighbor hopping. It turns out, that including higher order terms yields a stronger focusing within the Brillouin zone. As can be seen in the upper row, the vertex in the B1g symmetry points out the antinodal while in the B2g symmetry the nodal region of the Brillouin zone.

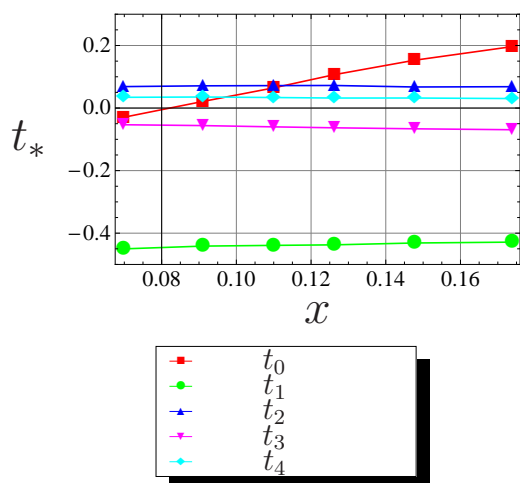


Figure 5.2: Doping dependence of the fit parameter within a fit procedure of a tight-binding dispersion to the quasi-particle band up to 4th nearest neighbors in the superconducting phase.

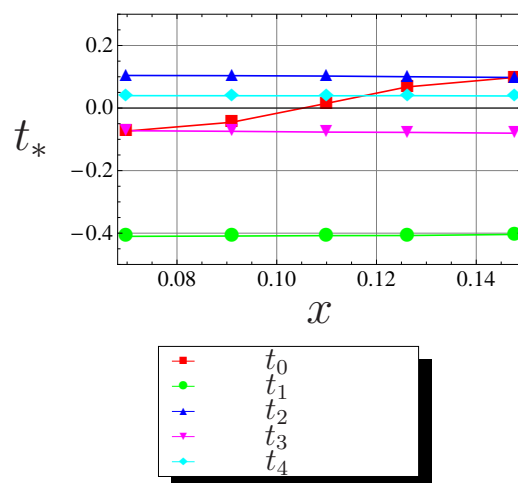


Figure 5.3: Doping dependence of the fit parameter within a fit procedure of a tight-binding dispersion to the quasi-particle band up to 4th nearest neighbors in the paramagnetic phase.

The superconducting gap and the pseudogap can be extracted in the following sections from the Raman spectrum as the position of the lowest peak in energy. But note that the gap out of the Raman spectrum is twice the superconducting gap measured from $\mu = 0$ symmetrically: $\Delta[\text{Raman}] = 2 * \Delta[\text{SC}]$.

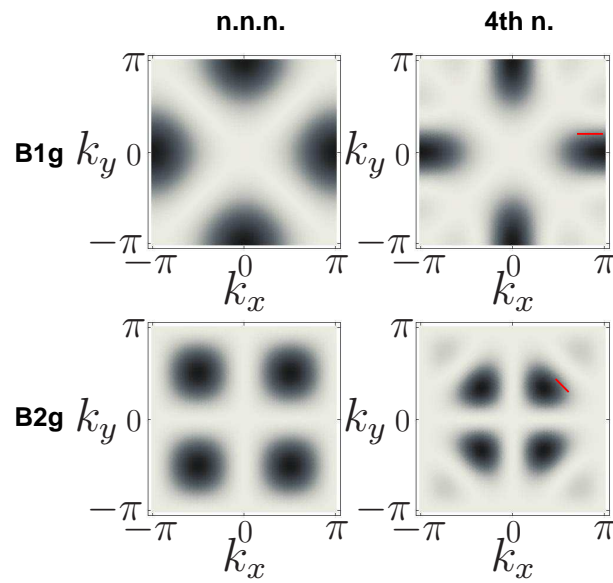


Figure 5.4: Density plot of $(\gamma^\nu(\mathbf{k}))^2$ for the B1g and B2g Raman symmetries in the superconducting phase at $x = 0.11$ hole-doping (black area means higher value). The results shown in the left column are obtained from a fitted dispersion up to next-nearest neighbor hopping while the results in the right column stem from a fitted dispersion up to 4th nearest neighbor hopping. The red lines indicate the paths which are used to extract the antinodal (upper row) and near-nodal (lower row) gaps out of the one-particle spectral-function (taken from (3)).

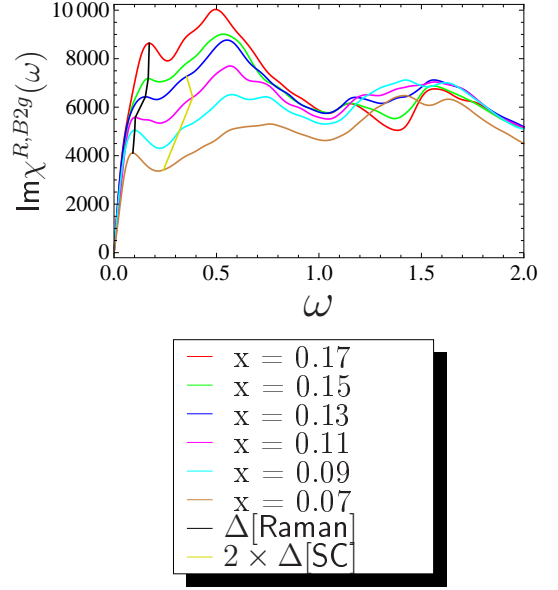
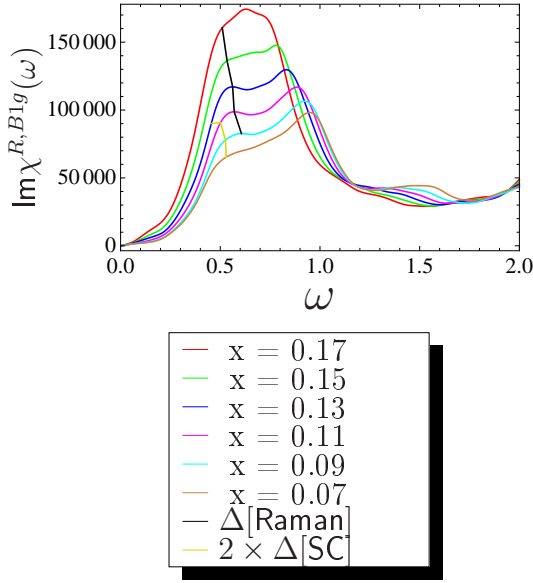


Figure 5.5: Plot of the B1g Raman spectrum for various hole-dopings in the superconducting phase. $\Delta[\text{Raman}]$ and $2 \times \Delta[\text{SC}]$ are guides to the eye (black: gap extracted from the Raman response; yellow: gap extracted from the one-particle spectral function, taken from (3)).

Figure 5.6: Plot of the B2g Raman spectrum for various hole-dopings in the superconducting phase. $\Delta[\text{Raman}]$ and $2 \times \Delta[\text{SC}]$ are guides to the eye (black: gap extracted from the Raman response; yellow: gap extracted from the one-particle spectral function, taken from (3)).

5.2 Superconducting phase

The main results of our calculation in the superconducting phase are given in the Figs. 5.5, 5.6 and Fig. 5.7. The Figs. 5.5 and 5.6 display the Raman response for the B1g and the B2g symmetry in the doping range described above. The first yields information about the antinodal and the latter about the nodal region. The black curve connecting the lowest lying peaks serves as a guide to the eye for a better visualization of the doping dependence. The yellow curve pursues the same intention but the data are gained from the gap extracted from the one-particle spectral-function (3). We find that the gap in the Raman response at the antinodal point increases with decreasing doping, while near the nodal point it slightly decreases. The plot of the doping dependence of the gap (Fig. 5.7) makes this behavior even clearer.

These Raman results can be reconciled with the ones derived from the one-particle spectral-function (3), both of which are shown in Fig. 5.7 and Fig. 5.8 for comparison. Both, the Raman and the one-particle data show qualitatively the same doping dependence of the gaps. However, the data derived from the Raman calculation reveal an energy shift depending on

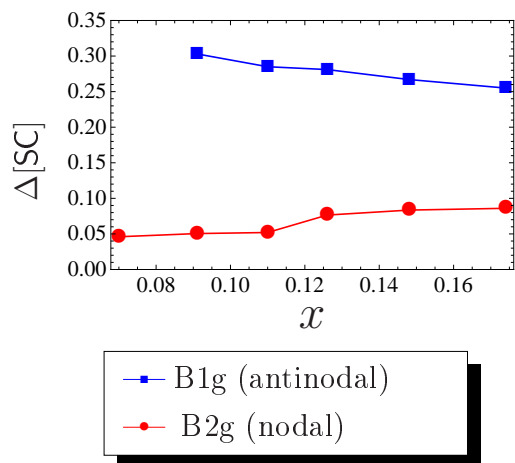


Figure 5.7: Doping dependence of the superconducting gap at the antinodal and near-nodal points extracted from the B1g and B2g Raman spectra.

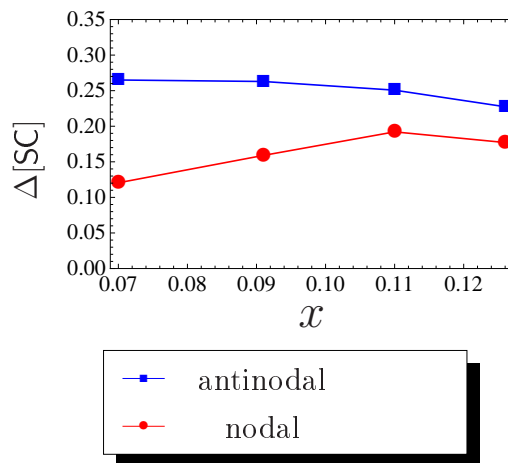


Figure 5.8: Doping dependence of the superconducting gap at the antinodal and near-nodal points extracted from the spectral function (taken from (3)).

the Raman vertex symmetry (see the yellow and black peak interpolation in Figs. 5.5 and 5.6). In the B1g symmetry (i.e., antinodal case) the Raman gap is slightly larger than the single-particle gap, while in the B2g case (i.e., near-nodal case) a gap of approximately half the size compared to the gap in the spectral-function is found. This shift in the Raman data to higher energies in the B1g case and to lower energies in the B2g case can be explained by a closer inspection of the vertex functions $(\gamma^\nu(\mathbf{k}))^2$ shown in the right plots of Fig. 5.4. These vertex functions act as a weighting factor in momentum space for the electron-hole excitations which are added up in Eq. (3.103).

In case of the B1g symmetry the vertex function $(\gamma^{B1g}(\mathbf{k}))^2$ is largest directly at $(\pi, 0)$. Therefore, the electron-hole excitations in this region enter Eq. (3.103) with a strong weight. Furthermore, these electron-hole excitations near (and not directly at) the antinodal gap are higher in energy compared to the excitations directly at the antinodal gap (see Fig. 5.1). This is the reason why the gap extracted from the Raman response is larger than the gap extracted from the spectral function by use of the path indicated as the red line in the upper right plot in Fig. 5.4. But as this is a deviation from the already large antinodal gap, we get a small relative shift.

In case of the B2g symmetry the vertex function $(\gamma^{B2g}(\mathbf{k}))^2$ is largest at a spot near $(\pi/2, \pi/2)$. Therefore, the gapless electron-hole excitations with zero energy in this region (the Brillouin zone diagonal) enter Eq. (3.103) with a strong weight. This is the reason why the gap extracted from the Raman response is smaller than the gap extracted from the spectral function which uses a path along the Fermi surface which, on average, is further away from the nodal point $(\pi/2, \pi/2)$ than the Raman response (this path is indicated as the red line in the lower right

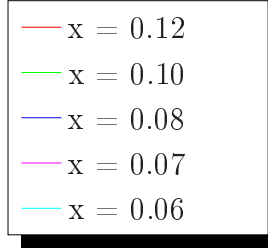
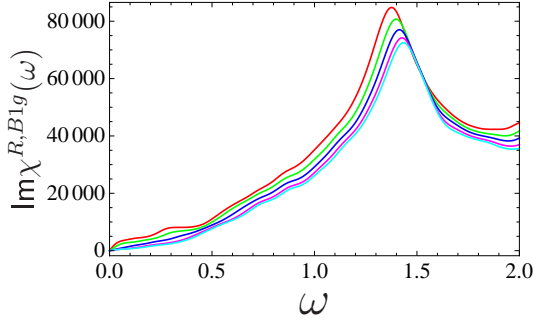


Figure 5.9: Plot of the B1g Raman spectrum for various hole-dopings in the paramagnetic phase.

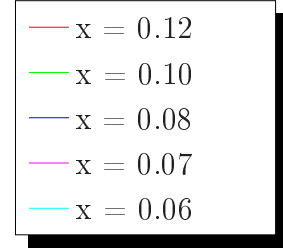
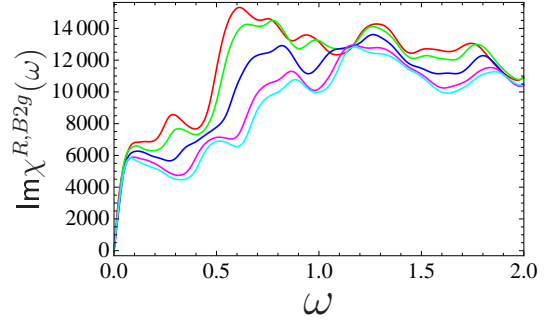


Figure 5.10: Plot of the B2g Raman spectrum for various hole-dopings in the paramagnetic phase.

plot in Fig. 5.4). And as this is a deviation from the very small near-nodal gap we get a large relative shift of the near-nodal gap size.

5.3 Normal state - Paramagnetic phase

Some calculations revealed the Hubbard model to show a pseudogap behavior in the *normal* state above T_c (115; 116). Hence, we are also interested in analyzing this state in order to find a gap in the Raman spectrum. However, we are limited with our cluster solver to $T = 0$ and can not investigate the Raman response at finite temperature. But a suitable method for *simulating* the *normal* state occurring for $T > T_c$ is to do not allow for U(1) symmetry breaking in the variational procedure. We employ therefore this paramagnetic phase for our Raman calculation to gain information about a possible pseudogap. Figs. 5.9 and 5.10 show the results for the B1g and the B2g channel, respectively.

Indeed, we find near $(\pi, 0)$ a pseudogap being larger compared to the superconducting gap at the antinodal region but following the same doping dependence. With decreasing doping the pseudogap increases. Again, this can be reconciled with the findings in (3). Furthermore, the doping dependence agrees qualitatively with finite- T QMC simulations (116) and also ARPES experiments (113; 114; 81).

An interesting question is, whether the origin of the *normal* state pseudogap survives in the

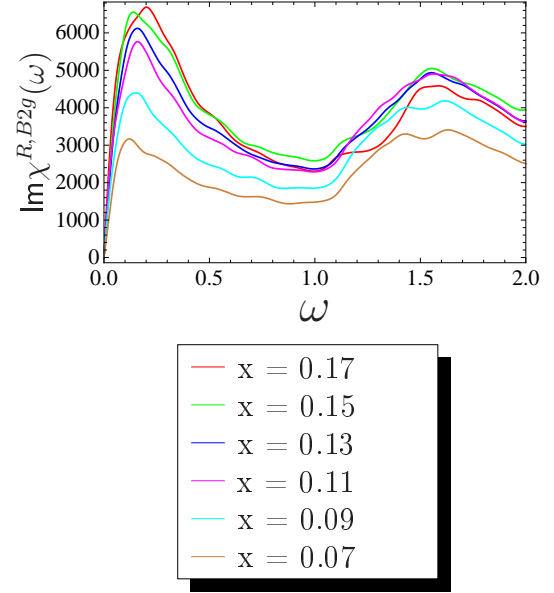
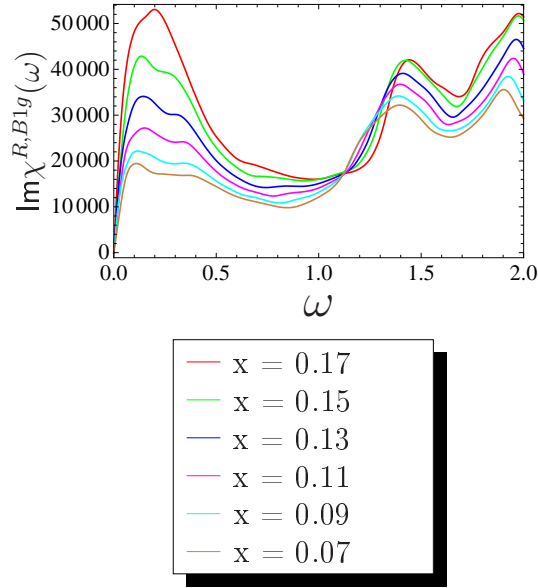


Figure 5.11: Plot of the B1g Raman spectrum for various hole-dopings in the superconducting phase with $\Sigma^{SC} = 0$.

Figure 5.12: Plot of the B2g Raman spectrum for various hole-dopings in the superconducting phase with $\Sigma^{SC} = 0$.

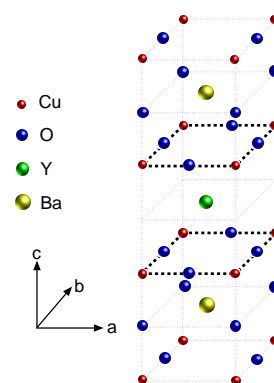
superconducting state. For this issue we switch off the anomalous part of the self-energy $\Sigma^{SC}(\omega) = 0$ in our Raman calculation in the superconducting state. The according results displayed in the Figs. 5.11 and 5.12 do not reveal any gap and therefore rule out a *normal* state origin of the gap in the U(1) symmetry-broken superconducting phase. These results as well as the one-particle results in (3) show, that with the onset of a U(1) symmetry breaking, the *normal* state origin of the pseudogap is replaced with a completely superconductivity based origin of the superconducting gap.

Our results on the Raman response combined with the results given in (3) strongly support the Hubbard model description of the gap behavior and the microscopic mechanisms of HTSC cuprates.

6

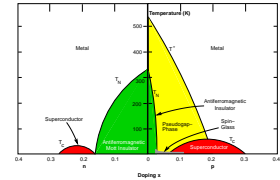
Summary

The physics of cuprate high-temperature superconductors is still an unsolved riddle. But in more than 20 years a remarkable progress was achieved on the experimental as well as on the theoretical side. Nearly no one in the community of strongly correlated physics doubts about the d-wave order parameter of the superconducting gap, the proximity of the antiferromagnetic Mott insulator being probably crucial for the understanding of the materials and, related to that, the magnetic origin of the underlying pairing mechanism. There is still a great number of open questions, maybe even more than 20 years ago, but these are much more concise and aiming at more detailed topics. Such a question is the character of the magnetic originated pairing. Is it instantaneous via the exchange coupling J or mediated by a retarded bosonic mode comparable to the phononic induced pairing in conventional BCS-type superconductors? A further question aims at properties of the gap in the superconducting as well as in the pseudogap state. Is the dichotomy of the antinodal and near-nodal gaps in the superconducting state, which was found in ARPES and Raman experiments, arising from distinct mechanisms or from different doping dependencies of the spin-fluctuation mediated pairing strength? And the nature of the pseudogap state is also one of the most important topics in cuprate superconductivity. To shed light on the cuprate riddle it is necessary to analyze two-particle excitations complementing the one-particle data.

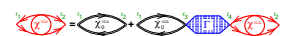
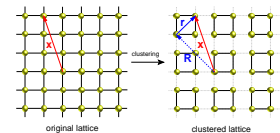
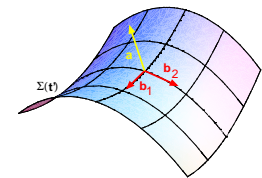


The magnetic susceptibility takes on a special position in this context as it renders information about the magnetic excitation spectrum which is believed to be directly related to the mechanism of superconductivity. And, indeed, INS experiments revealed a promising candidate for a bosonic mode possibly being the desired *pairing glue*. It is meant the resonance mode occurring as a general feature in the under- and optimal-doped cuprates at the wave vector $\mathbf{q}_{AF} = (\pi, \pi)$ being characteristic for the antiferromagnetism of the parent compound. In addition to this *fingerprint* of antiferromagnetism in the superconducting phase, a *hourglass-like* upward and downward dispersion emanating from \mathbf{q}_{AF} is obtained. Besides the role of the resonance mode as a mediator for the pairing, some of the salient features of the cuprates maybe described by interactions of the itinerant electrons with this mode.

Concerning the gap dichotomy Raman experiments yield worthy information as results from focussed regions of the Brillouin zone can be obtained. The position in energy of the first peak in the Raman spectrum is related to the gap in the density of states.



The present thesis provides a detailed treatment of magnetic excitations and Raman spectra in the two-dimensional one-band Hubbard model for the cuprate high-temperature superconductors. This model is believed to cover the essential microscopic degrees of freedom producing the macroscopic properties. As the core technical development, we derive a non-perturbative, $T = 0$ cluster approach for two-particle correlation functions from the general Bethe-Salpeter equation. This new approach contains no free adjustable parameters besides the model parameters for which the standard high- T_c values are used. As the self-energy in the Variational Cluster Approach (VCA, an embedded cluster method) for the one-particle Green's function we also obtain an effective electron-hole vertex from an isolated cluster. Combined with a fully dressed *bubble* susceptibility χ_0 which contains the one-particle VCA Green's function our new approach is only controlled by the cluster sizes and becomes exact in the limit of infinite sized clusters. We also introduce a controlling constant α effecting a fine-tuning of the vertex to account for finite-size effects. As we are restricted to clusters up to 10 sites for numerical reasons this is necessary to exhibit the small magnetic structures at small energy scales in the superconducting phase.



The constant α serves, in addition, as a quality indicator for our approach.

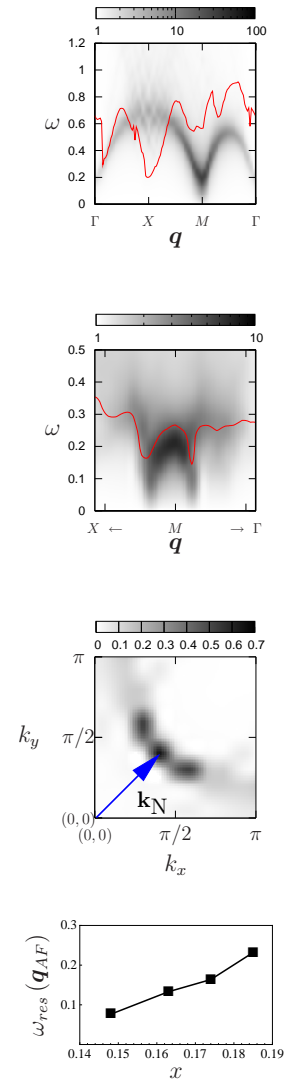
A similar approach is explained for the Raman response. However, due to the more complicated \mathbf{k} -structure of the Raman vertex we employ the so-called effective mass approximation for this.

The application of our two-particle approach to the antiferromagnetic phase of the hole-doped Hubbard model exhibits the expected spin-wave dispersion with the maximum weight around $\mathbf{q}_{AF} = (\pi, \pi)$. However, due to the limited number of cluster sites a finite-size gap occurs which decreases with increasing cluster size. Furthermore, for reason of screening effects, these finite-size effects are of minor importance for increased doping. The vertex becomes more short-ranged and can be extracted from already small clusters.

Upon further doping the most interesting phase, namely the superconducting is reached. Our results recover the celebrated resonance mode with its *hourglass*-like dispersion occurring in the superconductivity-induced gap of spin-flip electron-hole excitations. The upward branch of the *hourglass* is strongly damped as it extends into this continuum. A dramatic intensity reduction around $\simeq 0.8(\pi, \pi)$ is observed and addressed to the minimum in the spin-flip electron-hole continuum at exactly the wave vector connecting nodal points of the Fermi surface.

Further salient features obtained in our calculations are in qualitative accord with INS experiments. We find the energy of the resonance mode $\omega_{\text{res}}(\mathbf{q}_{AF})$ increasing as a function of doping, while the energy-integrated spin spectral weight at $\mathbf{q} = (\pi, \pi)$ decreases. And also the difference of the imaginary part of the susceptibility in the superconducting and *normal* states $\text{Im}\Delta\chi^{\pm}(\mathbf{q}_{AF}, \omega)$ can be reconciled with the experiments.

In summary, the calculated doping dependence of $\omega_{\text{res}}(\mathbf{q}_{AF})$, the *hourglass* dispersion of the resonance and its rapid decrease around a characteristic wave vector $2\mathbf{k}_N \simeq 0.8(\pi, \pi)$ are qualitatively consistent with the experiment and support the S=1 magnetic exciton scenario for the resonance mode. Some of these results have been obtained before in weak-coupling, however, by fitting the two-particle interaction to the experiment. In contrast, our results are obtained in the appropriate strong-correlation regime and contain no adjustable parameters.

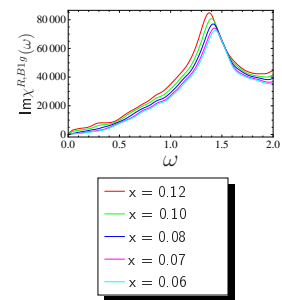
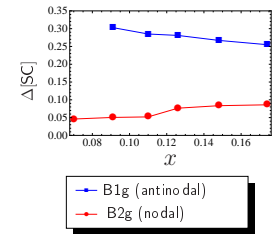


ARPES and Raman experiments revealed the gap in the superconducting state having a quite different behavior at the antinodal compared to the near-nodal region. Concerning the first, the gap increases with decreasing doping which was so far the believed characteristic doping dependence of the gap in the cuprates. But in case of the near-nodal region the gap exhibits the opposite dependence. So far, two distinct mechanism were proposed to explain this dichotomy of the gap but VCA calculation in combination with Quantum Monte Carlo results explain the different behavior as stemming from the doping dependence of the spin-fluctuation mediated pairing.

Within our approach to the Raman response, we verify the Hubbard model to cover the gap dichotomy seen in the experiments and found already via the spectral function analysis in a VCA calculation. Furthermore, by analyzing the effect of the anomalous self-energy on the gap in the superconducting state we proved its roots to be solely in superconductivity. In addition, our results in the *normal* state reveal a large pseudogap following the doping dependence of the antinodal gap.

Our cluster approach to two-particle excitations proves itself being appropriate to work out salient features of the cuprate high- T_c superconductors on the basis of the one-band Hubbard model. When taken together with the VCA results on the phase diagram and single-particle excitations a rather strong support for the Hubbard model description of HTSC materials is constituted.

As an outlook we like to suggest further improvements of the technique developed in the present thesis. To better control the doping of the physical system compared to the reference cluster, additional bath sites should be included. One-particle VCA calculations including such bath sites seem to be promising, so far. This would, of course, enlarge the corresponding Hilbert spaces, wherefore more numerical effort is required. One solution can be the parallelization of the programming code with a subsequent migration to supercomputer architectures. Another way can be the employment of an other cluster solver than Lanczos. Quantum Monte Carlo techniques, for example, can be used. This also would allow for calculations at finite temperatures.



A

Appendix

A.1 Restoring the translational invariance

At the end of section 3.1.3 we argued that the k -space dependence of the VCA Green's function is fully captured by \mathbf{k} as a continuous element of the original Brillouin zone. For an illustration we consider an one-dimensional example.

After tiling up the original lattice with the lattice constant a into N_c clusters with L_c sites each, the elementary unit of the superlattice consists of L_c sites. Therefore we obtain a in principle continuous (N_c is a large number)

$$\mathbf{k} \in \left[-\frac{\pi}{L_c a}, \frac{\pi}{L_c a}\right], \quad (\text{A.1})$$

with a periodicity $P = \frac{2\pi}{L_c a}$. However, \mathbf{K} is not continuous and obeys

$$\mathbf{K} \in \left[-\frac{\pi}{a}, \frac{\pi}{a}\right], \quad (\text{A.2})$$

with the periodicity is $P = \frac{2\pi}{a}$. The smallest discrete step which \mathbf{K} can take is $\Delta\mathbf{K} = \frac{2\pi}{L_c a}$. This is exactly the periodicity of the \mathbf{k} -lattice, wherefore $\mathbf{k} + \mathbf{K} \equiv \mathbf{k}$.

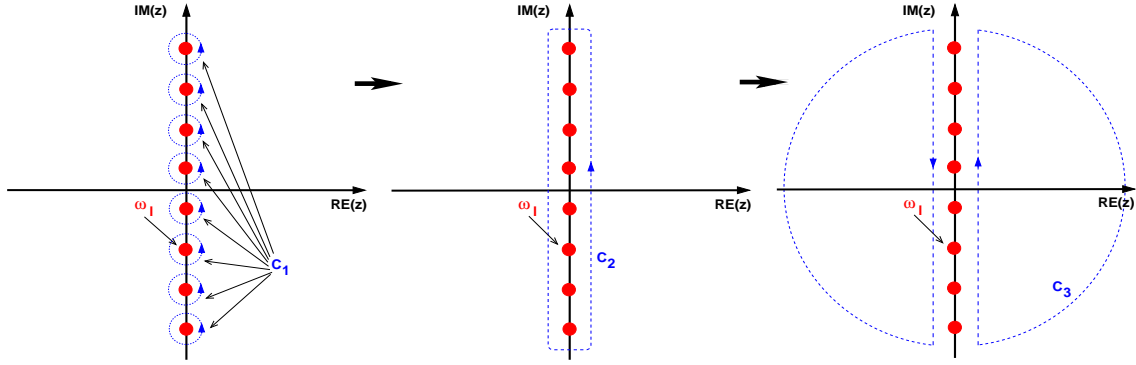


Figure A.1: Contour deforming from path C_1 over C_2 to C_3 in the complex plane for an analytical summation over Matsubara frequencies of a function with an explicitly known pole structure. Note, that we have to sum over a , in principle, infinite number of Matsubara frequencies. The finite number of paths C_1 and the finite range of the paths C_2 and C_3 is only for reason of visualization.

A.2 Matsubara frequency sums

In chapter 3 we make intense use of the Matsubara formalism for Green's functions. Within the calculations we often have to perform sums over Matsubara frequencies. For example, in the sections 3.1.5, 3.2.2 and 3.3.1 we need to sum up a function over fermionic Matsubara frequencies with the poles of the function explicitly known. In 3.2.4 the susceptibility at all bosonic Matsubara frequencies has to be summed up numerically as the pole structure is not given explicitly. An important easement is achievable by use of the pole structure of the Fermi- and the Bose-function (86; 87; 88; 89). The former has first order poles at the fermionic and the latter at the bosonic Matsubara frequencies. An explicitly known pole structure of the function that has to be summed up enables us to evaluate the sum analytically. If only the region where the considered function shows poles is known, we can achieve at least an easier and better converging numerical summation. Both cases are based on an intelligent deformation of paths used in contour integrals. Of course, it is still an ambitious task to find the ideal path.

A.2.1 Analytic evaluation of the $i\omega$ -sum

Evaluations of fermionic Matsubara sums such as in the function $\Xi_{st}(\mathbf{q}, \mathbf{k}, i\omega_m^b)$ (Eq. (3.65)) will be explained generally. We consider the following sum

$$S = T \sum_l F(i\omega_l), \quad (\text{A.3})$$

with $i\omega_l = (2l + \frac{1-\epsilon}{2})\pi T$ and $\epsilon = -1$ in case of a fermionic while $\epsilon = 1$ in case of a sum over bosonic Matsubara frequencies. With a function $\frac{1}{e^{\beta z} - \epsilon}$ having first order poles at the frequencies $z = i\omega_l = (2l + \frac{1-\epsilon}{2})\pi iT$ and assuming the function $F(z)$ not having poles at

these frequencies the sum S can be obtained as a sum over the contour integrals C_1 (see Fig. A.1). Each of these C_1 encircles one Matsubara frequency.

$$S = \frac{\epsilon}{2\pi i} \sum_{C_1} \int_{C_1} dz \frac{F(z)}{e^{\beta z} - \epsilon} \quad (\text{A.4})$$

The proof of the latter expression is easily accomplished by use of the residue theorem. Assuming the function $F(z)$ not having poles at the whole imaginary axis, the paths C_1 can be deformed and merged together yielding the path C_2 visualized in Fig. A.1. The vertical parts are infinitesimal close to the imaginary axis.

$$S = \frac{\epsilon}{2\pi i} \int_{C_2} dz \frac{F(z)}{e^{\beta z} - \epsilon} \quad (\text{A.5})$$

If the function $F(z)$ declines faster than $\frac{1}{z}$ the path C_2 is equivalent to C_3 also indicated in Fig. A.1. The latter contour encircles the complex plane except the imaginary axis. Hence, C_3 captures all poles of $F(z)$ and the S becomes by use of the residue theorem a sum over the residues of $F(z)$

$$S = \frac{\epsilon}{2\pi i} \int_{C_3} dz \frac{F(z)}{e^{\beta z} - \epsilon} = -\epsilon \sum_{\text{RES}} F(z) . \quad (\text{A.6})$$

The minus sign stems from the mathematical negative orientation of C_3 . With the knowledge of the discrete pole structure of $F(z)$ we are enabled to evaluate the infinite Matsubara sum.

A.2.2 Numerical evaluation of the $i\omega$ -sum

The following numerical evaluation of Matsubara sums is used for the calculation of the check-sum (Eq. 3.86) in section 3.2.4. If the pole structure of the $F(z)$ in the above equations is not given explicitly, we are not able to calculate the residues analytically. But in case of a function $F(z)$ that is analytic everywhere except a certain region on the real axis an ingenious path in the complex plane can be created that eases the numerical summation.

We start from the path C_2 indicated in Fig. A.1. Assuming the function $F(z)$ having poles only in the interval $[-\Omega', 0[$ and $]0, \Omega']$ on the real axis and declining faster than $\frac{1}{z}$, the path C_2 can be deformed to the path indicated in Fig. A.2. The partial paths C_b, C'_b, C_h and C'_h are infinitesimal close to the real axis while C_e and C'_e are infinitesimal close to the imaginary axis. The paths C_d, C'_d, C_f and C'_f on the other hand are at an arbitrary distance δ . As we are considering Green's functions the cutoff Ω' is an upper limit of the spectrum, i.e.

$$\text{Im}F(\omega + i0^+) = 0 \quad ; \quad |\omega| > \Omega' . \quad (\text{A.7})$$

Furthermore we can use the relation $F(z^*) = F^*(z)$. In the following the parts contributing to the integration path will be analyzed in detail.

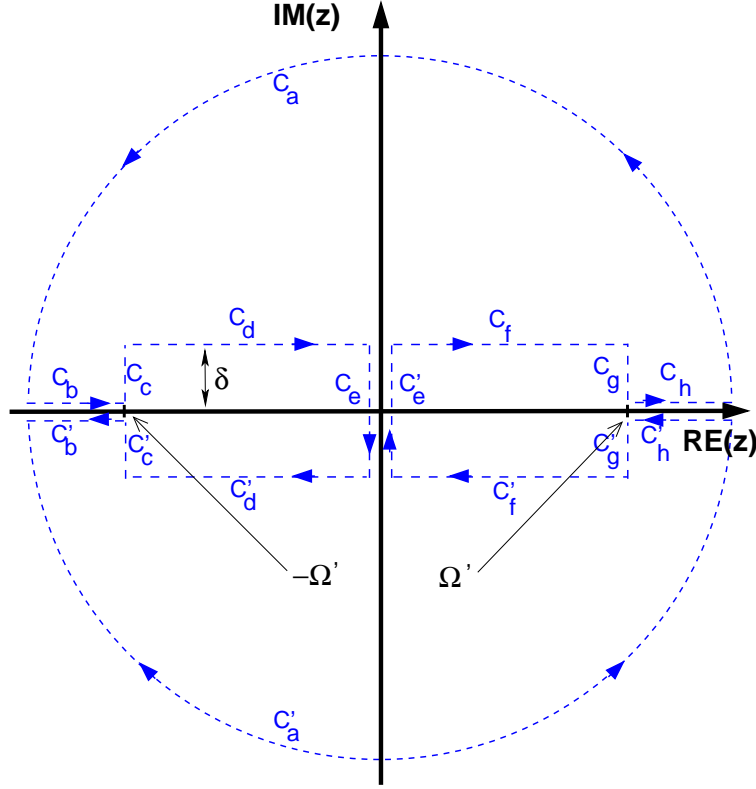


Figure A.2: Contour for the evaluation of a Matsubara sum of a function with poles only in the interval $[-\Omega', 0[$ and $]0, \Omega']$ on the real axis.

The contribution from the paths C_a and C'_a vanishes as these paths are at infinity. Next we consider the horizontal paths which become

$$\begin{aligned} S_h &= \frac{\epsilon}{2\pi i} \int_{C_b+C_d+C_f+C_h} dz \frac{F(z)}{e^{\beta z} - \epsilon} + \frac{\epsilon}{2\pi i} \int_{C'_b+C'_d+C'_f+C'_h} dz \frac{F(z)}{e^{\beta z} - \epsilon} \\ &= \frac{\epsilon}{\pi} \int_{C_b+C_d+C_f+C_h} dz \operatorname{Im} \frac{F(z)}{e^{\beta z} - \epsilon}. \end{aligned} \quad (\text{A.8})$$

It is noteworthy, that for a vanishing δ the common real axis integration is recovered. With Eq. (A.7) the horizontal contribution reduces to

$$S_h = \frac{\epsilon}{\pi} \int_{-\Omega'}^{\Omega'} d\omega \operatorname{Im} \frac{F(\omega + i\delta)}{e^{\beta(\omega+i\delta)} - \epsilon} \stackrel{T \rightarrow 0}{=} -\frac{1}{\pi} \int_{-\Omega'}^0 d\omega \operatorname{Im} F(\omega + i\delta). \quad (\text{A.9})$$

At last, we have to consider the vertical paths:

$$\begin{aligned} S_v &= \frac{\epsilon}{2\pi i} \int_{C_c+C'_c} dz \frac{F(z)}{e^{\beta z} - \epsilon} + \frac{\epsilon}{2\pi i} \int_{C_g+C'_g} dz \frac{F(z)}{e^{\beta z} - \epsilon} \\ &\quad + \frac{\epsilon}{2\pi i} \int_{C_e+C'_e} dz \frac{F(z)}{e^{\beta z} - \epsilon} = S_c + S_g + S_e. \end{aligned} \quad (\text{A.10})$$

The first two of the three parts defined in the above equation become:

$$\begin{aligned}
S_c &= \frac{\epsilon}{2\pi i} \int_0^\delta i dx \frac{F(-\Omega' + ix)}{e^{\beta(-\Omega' + ix)} - \epsilon} + \frac{\epsilon}{2\pi i} \int_{-\delta}^0 i dx \frac{F(-\Omega' + ix)}{e^{\beta(-\Omega' + ix)} - \epsilon} \\
&= \frac{\epsilon}{2\pi i} \int_0^\delta i dx \frac{F(-\Omega' + ix)}{e^{\beta(-\Omega' + ix)} - \epsilon} - \frac{\epsilon}{2\pi i} \int_0^\delta (-i) dx \frac{F(-\Omega' - ix)}{e^{\beta(-\Omega' - ix)} - \epsilon} \\
&= \frac{\epsilon}{\pi} \int_0^\delta dx \operatorname{Re} \frac{F(-\Omega' + ix)}{e^{\beta(-\Omega' + ix)} - \epsilon} \stackrel{T \rightarrow 0}{=} -\frac{1}{\pi} \int_0^\delta dx \operatorname{Re} F(-\Omega' + ix) \tag{A.11}
\end{aligned}$$

$$S_g = -\frac{\epsilon}{\pi} \int_0^\delta dx \operatorname{Re} \frac{F(\Omega' + ix)}{e^{\beta(\Omega' + ix)} - \epsilon} \stackrel{T \rightarrow 0}{=} 0$$

There is only the integration close to the imaginary axis left. But as this integral is simply given by the Matsubara sum over the frequencies $|\omega_l| < \delta$ we obtain

$$S_e = \frac{\epsilon}{2\pi i} \int_{C_e + C'_e} dz \frac{F(z)}{e^{\beta z} - \epsilon} = 2T \sum_{l=0}^{l_{max}} \operatorname{Re} F(i\omega_l) \stackrel{T \rightarrow 0}{=} \frac{1}{\pi} \int_0^\delta dx \operatorname{Re} F(ix), \tag{A.12}$$

with l_{max} such that $|\omega_l| < \delta$ holds. Combining all results in case of $T = 0$ yields:

$$S \stackrel{T \rightarrow 0}{=} -\frac{1}{\pi} \int_0^\delta dx \operatorname{Re} F(-\Omega' + ix) - \frac{1}{\pi} \int_{-\Omega'}^0 d\omega \operatorname{Im} F(\omega + i\delta) + \frac{1}{\pi} \int_0^\delta dx \operatorname{Re} F(ix) \tag{A.13}$$

Compared to the standard integration along the real ω -axis we have to evaluate the additional integrals along the vertical paths C_c and C_e which compensate the finite value of δ . But we gain a more smooth integration along C_d as this integration path is at the distance δ from the poles of $F(z)$. Hence, only a few points have to be calculated for the numerical integration. Note, that one has to use enough points for the path C_e near $\omega_l = 0$ in case of small temperatures and $F(z)$ having poles close to $\omega_l = 0$.

A.3 Particle-hole transformation in one spin-channel

The focus of this thesis is on the calculation of two-particle properties of high-temperature superconductors for which we use the Hubbard model. To access the superconducting phase a pairing Weiss field is introduced as a variational parameter in the VCA besides the chemical potential. Furthermore the antiferromagnetic phase is accounted for through an antiferromagnetic Weiss field (see section 3.1.5 for details). Hence, we explicitly break the U(1) and SU(2) invariance of the Hubbard model, but the S^z quantum number is still conserved. However, for practical reason it is advantageous to restore the U(1) symmetry as each particle-number subspace of the full Hilbertspace can be constructed for its own. For this reason we introduce a particle-hole transformation (ph-trafo) for only one spin channel (here spin-down):

$$c_{\alpha\uparrow} \xrightarrow{\text{ph-trafo}} c_{\alpha\uparrow} \quad ; \quad c_{\alpha\uparrow}^\dagger \xrightarrow{\text{ph-trafo}} c_{\alpha\uparrow}^\dagger \quad (\text{A.14})$$

$$c_{\alpha\downarrow} \xrightarrow{\text{ph-trafo}} c_{\alpha\downarrow}^\dagger \quad ; \quad c_{\alpha\downarrow}^\dagger \xrightarrow{\text{ph-trafo}} c_{\alpha\downarrow} \quad (\text{A.15})$$

The one-band Hubbard hamiltonian will be transformed as:

$$\begin{aligned} H_{Hubb} &= - \sum_{i,j,\sigma} (t_{ij} - \mu\delta_{ij}) c_{i\sigma}^\dagger c_{j\sigma} + U \sum_i n_{i\uparrow} n_{i\downarrow} \\ &\quad \downarrow \text{ph-trafo} \\ H_{Hubb}^{ph} &= - \sum_{i,j} (t_{ij} - \mu\delta_{ij}) (c_{i\uparrow}^\dagger c_{j\uparrow} - c_{j\downarrow}^\dagger c_{i\downarrow}) - U \sum_i n_{i\uparrow} n_{i\downarrow} + N\mu + N_\uparrow U \quad (\text{A.16}) \end{aligned}$$

And the Weiss fields (see section 3.1.5 for details) transform as:

$$\begin{aligned} \Delta_{SC}(\mathbf{R}_a) &= h_{SC} \sum_{n.n.} \frac{\eta_{ij}}{2} (c_{ai\uparrow} c_{aj\downarrow} + h.c.) \\ \Delta_{AF}(\mathbf{R}_a) &= h_{AF} \sum_i (n_{ai\uparrow} - n_{ai\downarrow}) e^{\mathbf{Q}_{AF}\mathbf{r}_i} \\ \Delta_\mu(\mathbf{R}_a) &= \mu' \sum_i (n_{ai\uparrow} + n_{ai\downarrow}) \\ &\quad \downarrow \text{ph-trafo} \\ \Delta_{SC}^{ph}(\mathbf{R}_a) &= h_{SC} \sum_{n.n.} \frac{\eta_{ij}}{2} (c_{ai\uparrow}^\dagger c_{aj\downarrow}^\dagger + h.c.) \quad (\text{A.17}) \end{aligned}$$

$$\Delta_{AF}^{ph}(\mathbf{R}_a) = h_{AF} \sum_i (n_{ai\uparrow} + n_{ai\downarrow}) e^{\mathbf{Q}_{AF}\mathbf{r}_i} \quad (\text{A.18})$$

$$\Delta_\mu^{ph}(\mathbf{R}_a) = \mu' \sum_i (n_{ai\uparrow} - n_{ai\downarrow}) + N\mu' \quad (\text{A.19})$$

Clearly, the SC-field transforms to a spin-flip term, wherefore the U(1) symmetry is restored but the prize is the violation of the S^z conservation.

At last we present the spin-down particle-hole transformed normal and anomalous Green's functions:

$$G_{\alpha\beta\uparrow}(\tau, \tau') = -\langle T_\tau \{c_{\alpha\uparrow}(\tau)c_{\beta\uparrow}^\dagger(\tau')\} \rangle \xrightarrow{\text{ph-trafo}} -\langle T_\tau \{c_{\alpha\uparrow}(\tau)c_{\beta\uparrow}^\dagger(\tau')\} \rangle = G_{\alpha\beta\uparrow}^{ph}(\tau, \tau') \quad (\text{A.20})$$

$$G_{\alpha\beta\downarrow}(\tau, \tau') = -\langle T_\tau \{c_{\alpha\downarrow}(\tau)c_{\beta\downarrow}^\dagger(\tau')\} \rangle \xrightarrow{\text{ph-trafo}} \langle T_\tau \{c_{\beta\downarrow}(\tau')c_{\alpha\downarrow}^\dagger(\tau)\} \rangle = -G_{\beta\alpha\downarrow}^{ph}(\tau', \tau) \quad (\text{A.21})$$

$$F_{\alpha\beta}(\tau, \tau') = -\langle T_\tau \{c_{\alpha\uparrow}(\tau)c_{\beta\downarrow}(\tau')\} \rangle \xrightarrow{\text{ph-trafo}} \langle T_\tau \{c_{\alpha\uparrow}(\tau)c_{\beta\downarrow}^\dagger(\tau')\} \rangle = G_{\alpha\beta\uparrow\downarrow}^{ph}(\tau, \tau') \quad (\text{A.22})$$

$$F_{\alpha\beta}^*(\tau, \tau') = -\langle T_\tau \{c_{\beta\downarrow}^\dagger(\tau')c_{\alpha\uparrow}^\dagger(\tau)\} \rangle \xrightarrow{\text{ph-trafo}} \langle T_\tau \{c_{\beta\downarrow}(\tau')c_{\alpha\uparrow}^\dagger(\tau)\} \rangle = G_{\beta\alpha\downarrow\uparrow}^{ph}(\tau', \tau) \quad (\text{A.23})$$

The $G_{\alpha\beta\uparrow\downarrow}^{ph}(\tau, \tau')$ denote spin-flip Green's functions.

A.4 Avoiding singularities in the vertex function

We mentioned in section 3.2.3 the numerical problems occurring from the inversion of the exact cluster susceptibility in the superconducting phase. To avoid these problems we apply some trivial algebraic transformations to Eq. (3.77) in order to derive an expression without an inversion of the exact cluster susceptibility for its own. There are two possible expression either containing the inversion of the $\chi_0^{VCA}(\mathbf{q}, i\omega_m^b)$ or the $\chi_0^c(i\omega_m^b)$.

$$\underline{\chi_0^{VCA}(\mathbf{q}, i\omega_m^b)}$$

$$\begin{aligned} \chi(\mathbf{q}, i\omega_m^b) &= \chi^c(i\omega_m^b) \left(\chi_0^c(i\omega_m^b) - \chi^c(i\omega_m^b) + \chi_0^c(i\omega_m^b) [\chi_0^{VCA}(\mathbf{q}, i\omega_m^b)]^{-1} \chi^c(i\omega_m^b) \right)^{-1} \\ &\quad \times \chi_0^c(i\omega_m^b) \end{aligned} \quad (\text{A.24})$$

$$\underline{\chi_0^c(i\omega_m^b)}$$

$$\begin{aligned} \chi(\mathbf{q}, i\omega_m^b) &= \chi^c(i\omega_m^b) \left(\chi^c(i\omega_m^b) + \chi_0^{VCA}(\mathbf{q}, i\omega_m^b) - \chi_0^{VCA}(\mathbf{q}, i\omega_m^b) [\chi_0^c(i\omega_m^b)]^{-1} \chi^c(i\omega_m^b) \right)^{-1} \\ &\quad \times \chi_0^{VCA}(\mathbf{q}, i\omega_m^b) \end{aligned} \quad (\text{A.25})$$

In the numerical implementation the latter expression is favorable as the $\chi_0^c(i\omega_m^b)$ has to be inverted only once for all of the values of \mathbf{q} .

Bibliography

- [1] S. Brehm, E. Arrigoni, M. Aichhorn, and W. Hanke, arXiv.org:0811.0552 (2008).
- [2] M. Aichhorn, private communication .
- [3] M. Aichhorn, E. Arrigoni, Z. B. Huang, and W. Hanke, Phys. Rev. Lett. **99**, 257002 (2007).
- [4] J. G. Bednorz and K. A. Müller, Zeit. Phys. B **64**, 189 (1986).
- [5] H. K. Onnes, Commun.Phys.Lab.Univ.Leiden **120b,122b,124c**, (1911).
- [6] J. Bardeen, L. N. Cooper, and J. R. Schrieffer, Phys. Rev. B **108**, 1175 (1957).
- [7] G. M. Eliashberg, Soviet Phys. JETP, **11**, 696 (1960).
- [8] W. L. McMillan and J. M. Rowell, Phys. Rev. Lett. **14**, 108 (1965).
- [9] *Superconductivity*, edited by R. D. Parks (Marcel Dekker, inc., New York, 1969), Vol. 1.
- [10] *Superconductivity*, edited by R. D. Parks (Marcel Dekker, inc., New York, 1969), Vol. 2.
- [11] E. Maxwell, Phys. Rev. **78**, 477 (1950).
- [12] N. Mott, Philos.Mag. **6**, 287 (1961).
- [13] N. Mott, *Metal-Insulator Transitions* (Taylor and Francis, London, 1990).
- [14] C. Tsuei and J. Kirtley, in *The Physics of Superconductors Vol.I*, edited by K. Bennemann and J. Ketterson (Springer, Berlin, Heidelberg, 2003), Chap. Pairing Symmetry in Cuprate Superconductors: Phase-Sensitive Tests.
- [15] M. Filipkowski, J. Budnick, and Z. Tan, Physica C: Superconductivity **167**, 35 (1990).

-
- [16] F. C. Chou, N. R. Belk, M. A. Kastner, R. J. Birgeneau, and A. Aharony, *Phys. Rev. Lett.* **75**, 2204 (1995).
- [17] S. Wakimoto, S. Ueki, Y. Endoh, and K. Yamada, *Phys. Rev. B* **62**, 3547 (2000).
- [18] A. N. Lavrov, Y. Ando, S. Komiyama, and I. Tsukada, *Phys. Rev. Lett.* **87**, 017007 (2001).
- [19] T. Timusk and B. W. Statt, *Rep. Prog. Phys.* **62**, 61 (1999).
- [20] M. Norman and C. Pepin, *Reports on Progress in Physics* **66**, 1547 (2003).
- [21] P. W. Anderson, *Science* **235**, 1196 (1987).
- [22] G. Baskaran, Z. Zou, and P. W. Anderson, *Solid State Communications* **63**, 973 (1987).
- [23] G. Kotliar and J. Liu, *Phys. Rev. Lett.* **61**, 1784 (1988).
- [24] N. Nagaosa and P. A. Lee, *Phys. Rev. B* **45**, 966 (1992).
- [25] V. J. Emery, S. A. Kivelson, and O. Zachar, *Phys. Rev. B* **56**, 6120 (1997).
- [26] I. Affleck and J. B. Marston, *Phys. Rev. B* **37**, 3774 (1988).
- [27] H. J. Schulz, *prb* **39**, 2940 (1989).
- [28] X.-G. Wen and P. A. Lee, *Phys. Rev. Lett.* **76**, 503 (1996).
- [29] P. A. Lee, N. Nagaosa, T.-K. Ng, and X.-G. Wen, *Phys. Rev. B* **57**, 6003 (1998).
- [30] D. A. Ivanov, P. A. Lee, and X.-G. Wen, *Phys. Rev. Lett.* **84**, 3958 (2000).
- [31] S. Chakravarty, R. B. Laughlin, D. K. Morr, and C. Nayak, *Phys. Rev. B* **63**, 094503 (2001).
- [32] C. M. Varma, *Phys. Rev. B* **55**, 14554 (1997).
- [33] M. E. Simon and C. M. Varma, *Phys. Rev. Lett.* **89**, 247003 (2002).
- [34] J. Rossat-Mignod, L. P. Regnault, C. Vettier, P. Bourges, P. Burlet, J. Bossy, J. Y. Henry, and G. Lepertot, *Physica C* **185–198**, 86 (1991).
- [35] M. Arai, T. Nishijima, Y. Endoh, T. Egami, S. Tajima, K. Tomimoto, Y. Shiohara, M. Takahashi, A. Garrett, and S. M. Bennington, *Phys. Rev. Lett.* **83**, 608 (1999).
- [36] S. Pailhès, Y. Sidis, P. Bourges, V. Hinkov, A. Ivanov, C. Ulrich, L. P. Regnault, and B. Keimer, *Phys. Rev. Lett.* **93**, 167001 (2004).
- [37] D. Reznik, P. Bourges, L. Pintschovius, Y. Endoh, Y. Sidis, T. Masui, and S. Tajima, *Phys. Rev. Lett.* **93**, 207003 (2004).

- [38] Y. Sidis, S. Pailhès, V. Hinkov, B. Fauqué, C. Ulrich, L. Capogna, A. Ivanov, L.-P. Regnault, B. Keimer, and P. Bourges, *Comptes Rendus Physique* **8**, 745 (2007), neutron scattering: a comprehensive tool for condensed matter research.
- [39] V. Hinkov, P. Bourges, S. Pailhès, Y. Sidis, A. Ivanov, C. D. Frost, T. G. Perring, C. T. Lin, D. P. Chen, and B. Keimer, *Nature* **3**, 780 (2007).
- [40] P. W. Anderson, *Science* **316**, 1705 (2007).
- [41] T. A. Maier, D. Poilblanc, and D. J. Scalapino, *Physical Review Letters* **100**, 237001 (2008).
- [42] B. Kyung, D. Senechal, and A. M. S. Tremblay, *Retarded interactions, short-range spin fluctuations, and high temperature superconductivity*, 2008.
- [43] S. D. Wilson, S. Li, P. Dai, W. Bao, J.-H. Chung, H. J. Kang, S.-H. Lee, S. Komiya, Y. Ando, and Q. Si, *Physical Review B (Condensed Matter and Materials Physics)* **74**, 144514 (2006).
- [44] S. V. Borisenko, A. A. Kordyuk, T. K. Kim, A. Koitzsch, M. Knupfer, J. Fink, M. S. Golden, M. Eschrig, H. Berger, and R. Follath, *Phys. Rev. Lett.* **90**, 207001 (2003).
- [45] J. Hwang, T. Timusk¹, and G. D. Gu, *Nature* **427**, 714 (2004).
- [46] J. F. Zasadzinski, L. Ozyuzer, N. Miyakawa, K. E. Gray, D. G. Hinks, and C. Kendziora, *Phys. Rev. Lett.* **87**, 067005 (2001).
- [47] T. Dahm, V. Hinkov, S. V. Borisenko, A. A. Kordyuk, V. B. Zabolotnyy, J. Fink, B. Büchner, D. J. Scalapino, W. Hanke, and B. Keimer, *Nature* **nphys1180**, (2009).
- [48] M. Vojta, T. Vojta, and R. K. Kaul, *Physical Review Letters* **97**, 097001 (2006).
- [49] G. S. Uhrig, K. P. Schmidt, and M. Grüninger, *Phys. Rev. Lett.* **93**, 267003 (2004).
- [50] H.-Y. Kee, S. A. Kivelson, and G. Aeppli, *Phys. Rev. Lett.* **88**, 257002 (2002).
- [51] A. Abanov, A. V. Chubukov, M. Eschrig, M. R. Norman, and J. Schmalian, *Phys. Rev. Lett.* **89**, 177002 (2002).
- [52] M. R. Norman, *Phys. Rev. B* **63**, 092509 (2001).
- [53] M. Eschrig, *Adv. Phys.* **55**, 47 (2006).
- [54] M. A. Kastner, R. J. Birgeneau, G. Shirane, and Y. Endoh, *Rev. Mod. Phys.* **70**, 897 (1998).
- [55] B. Keimer, R. J. Birgeneau, A. Cassanho, Y. Endoh, R. W. Erwin, M. A. Kastner, and G. Shirane, *Phys. Rev. Lett.* **67**, 1930 (1991).

-
- [56] B. Keimer, N. Belk, R. J. Birgeneau, A. Cassanho, C. Y. Chen, M. Greven, M. A. Kastner, A. Aharony, Y. Endoh, R. W. Erwin, and G. Shirane, *Phys. Rev. B* **46**, 14034 (1992).
- [57] V. J. Emery, *Phys. Rev. Lett.* **58**, 2794 (1987).
- [58] J. Hubbard, *Proc. R. Soc. London* **276**, 238 (1963).
- [59] M. Potthoff, *Eur. Phys. J. B* **32**, 429 (2003).
- [60] M. Potthoff, *Eur. Phys. J. B* **36**, 335 (2003).
- [61] M. Potthoff, M. Aichhorn, and C. Dahnken, *Phys. Rev. Lett.* **91**, 206402 (2003).
- [62] M. Potthoff, *Advances in Solid State Physics* (Springer, Berlin, 2006), Vol. 45, pp. 135–147.
- [63] R. Freund, in *Templates for the Solution of Algebraic Eigenvalue Problems: A Practical Guide*, edited by Z. Bai, J. Demmel, J. Dongarra, A. Ruhe, and H. van der Vorst (SIAM, Philadelphia, 2000), Chap. Band Lanczos method.
- [64] C. Dahnken, M. Aichhorn, W. Hanke, E. Arrigoni, and M. Potthoff, *Phys. Rev. B* **70**, 245110 (2004).
- [65] D. Sénéchal, P. L. Lavertu, M. A. Marois, and A. M. S. Tremblay, *Phys. Rev. Lett.* **94**, 156404 (2005).
- [66] M. Aichhorn and E. Arrigoni, *Europhys. Lett.* **72**, 117 (2005).
- [67] M. Aichhorn, E. Arrigoni, M. Potthoff, and W. Hanke, *Phys. Rev. B* **74**, 024508 (2006).
- [68] M. Aichhorn, E. Arrigoni, M. Potthoff, and W. Hanke, *Phys. Rev. B* **76**, 224509 (2007).
- [69] M. Aichhorn, E. Arrigoni, M. Potthoff, and W. Hanke, *Phys. Rev. B* **74**, 235117 (2006).
- [70] I. Eremin, D. K. Morr, A. V. Chubukov, K. H. Bennemann, and M. R. Norman, *Phys. Rev. Lett.* **94**, 147001 (2005).
- [71] A. Abanov and A. V. Chubukov, *Phys. Rev. Lett.* **83**, 1652 (1999).
- [72] I. Sega, P. Prelovšek, and J. Bonča, *Phys. Rev. B* **68**, 054524 (2003).
- [73] P. Prelovšek and I. Sega, *Physical Review B (Condensed Matter and Materials Physics)* **74**, 214501 (2006).
- [74] R. Zeyher, *Theory of the hourglass dispersion of magnetic excitations in high-T_c cuprates*, 2008.
- [75] E. Demler and S.-C. Zhang, *Phys. Rev. Lett.* **75**, 4126 (1995).

-
- [76] E. Demler, W. Hanke, and S.-C. Zhang, *Rev. Mod. Phys.* **76**, 909 (2004).
- [77] M. Opel, R. Nemetschek, C. Hoffmann, R. Philipp, P. F. Müller, R. Hackl, I. Tütto, A. Erb, B. Revaz, E. Walke, H. Berger, and L. Forró, *Phys. Rev. B* **61**, 9752 (2000).
- [78] M. L. Tacon, A. Sacuto, A. Georges, G. Kotliar, Y. Gallais, D. Colson, and A. Forget, *Nature Phys.* **2**, 537 (2006).
- [79] K. Tanaka, W. S. Lee, D. H. Lu, A. Fujimori, T. Fujii, Risdiana, I. Terasaki, D. J. Scalapino, T. P. Devereaux, Z. Hussain, and Z. X. Shen, *Science* **314**, 1910 (2006).
- [80] T. Kondo, T. Takeuchi, A. Kaminski, S. Tsuda, and S. Shin, *Physical Review Letters* **98**, 267004 (2007).
- [81] M. Hashimoto, T. Yoshida, K. Tanaka, A. Fujimori, M. Okusawa, S. Wakimoto, K. Yamada, T. Kakeshita, H. Eisaki, and S. Uchida, *Phys. Rev. B* **75**, 140503 (2007).
- [82] N. D. Mermin and H. Wagner, *Phys. Rev. Lett.* **17**, 1133 (1966).
- [83] E. Arrigoni, M. Aichhorn, M. Daghofer, and W. Hanke, [arXiv.org:0902.0535](https://arxiv.org/abs/0902.0535) (2009).
- [84] F. C. Zhang and T. M. Rice, *Phys. Rev. B* **37**, 3759 (1988).
- [85] H. Bethe, *Z. Phys.* **71**, 205 (1931).
- [86] W. Nolting, *Grundkurs Theoretische Physik 7* (Springer, Berlin, Heidelberg, 2002), 5th edition.
- [87] G. D. Mahan, *Many-Particle Physics* (Plenum Press, New York, 1990).
- [88] A. L. Fetter and J. D. Walecka, *Quantum theory of many-particle systems* (McGraw-Hill, Boston, Mass., 1971).
- [89] J. W. Negele and H. Orland, *Quantum many-particle systems*, Vol. 68 of *Frontiers in physics* (Addison-Wesley, Redwood City, Calif., 1988).
- [90] E. Dagotto, *Rev. Mod. Phys.* **66**, 763 (1994).
- [91] S. R. White, *Phys. Rev. Lett.* **69**, 2863 (1992).
- [92] S. R. White, *Phys. Rev. B* **48**, 10345 (1993).
- [93] A. Georges, G. Kotliar, W. Krauth, and M. J. Rozenberg, *Rev. Mod. Phys.* **68**, 13 (1996).
- [94] T. A. Maier, M. Jarrell, T. C. Schulthess, P. R. C. Kent, and J. B. White, *Phys. Rev. Lett.* **95**, 237001 (2005).
- [95] A. I. Lichtenstein and M. I. Katsnelson, *Phys. Rev. B* **62**, R9283 (2000).

-
- [96] G. Kotliar, S. Y. Savrasov, G. Pálsson, and G. Biroli, *Phys. Rev. Lett.* **87**, 186401 (2001).
- [97] G. Biroli and G. Kotliar, *Phys. Rev. B* **65**, 155112 (2002).
- [98] C. J. Bolech, S. S. Kancharla, and G. Kotliar, *Phys. Rev. B (Condensed Matter and Materials Physics)* **67**, 075110 (2003).
- [99] M. H. Hettler, A. N. Tahvildar-Zadeh, M. Jarrell, T. Pruschke, and H. R. Krishnamurthy, *Phys. Rev. B* **58**, R7475 (1998).
- [100] D. Sénéchal, D. Perez, and M. Pioro-Ladriere, *Phys. Rev. Lett.* **84**, 522 (2000).
- [101] D. Sénéchal, D. Perez, and D. Plouffe, *Phys. Rev. B* **66**, 075129 (2002).
- [102] C. Gros and R. Valenti, *Phys. Rev. B* **48**, 418 (1993).
- [103] D. Senechal, arXiv:0806.2690 (2008).
- [104] J. M. Luttinger and J. C. Ward, *Phys. Rev.* **118**, 1417 (1960).
- [105] M. Potthoff, *Condens. Mat. Phys.* **9**, 557 (2006).
- [106] G. Biroli, O. Parcollet, and G. Kotliar, *Phys. Rev. B* **69**, 205108 (2004).
- [107] Y. M. Vilk and A.-M. S. Tremblay, *J. Phys. I* **7**, 1309 (1997).
- [108] T. Devereaux and R. Hackl, *Rev. Mod. Phys.* **79**, 175 (2007).
- [109] Y. Nambu, *Phys. Rev.* **117**, 648 (1960).
- [110] N. W. Ashcroft and N. D. Mermin, *Solid State Physics* (Saunders College, Philadelphia, 1976).
- [111] M. Aichhorn, *Ordering Phenomena in Strongly-Correlated Systems: Cluster Perturbation Theory Approaches*, PhD Thesis, Technische Universität Graz, 2004.
- [112] H. F. Fong, P. Bourges, Y. Sidis, L. P. Regnault, J. Bossy, A. Ivanov, and B. Keimer, *Phys. Rev. B* **61**, 14773 (2000).
- [113] A. G. Loeser, Z.-X. Shen, D. S. Dessau, D. S. Marshall, C. H. Park, P. Fournier, and A. Kapitulnik, *Science* **273**, 325 (1996).
- [114] H. Ding, T. Yokoya, J. C. Campuzano, T. Takahashi, M. Randeria, M. R. Norman, T. Mochiku, K. Kadowaki, and J. Giapintzakis, *Nature (London)* **382**, 51 (1996).
- [115] T. A. Maier, M. S. Jarrell, and D. J. Scalapino, *Phys. Rev. Lett.* **96**, 047005 (2006).
- [116] R. Preuss, W. Hanke, C. Gröber, and H. G. Evertz, *Phys. Rev. Lett.* **79**, 1122 (1997).

Danksagung

Ich möchte mich an dieser Stelle bei Herrn Prof. Dr. Werner Hanke bedanken, der es mir ermöglichte, in einem hochaktuellen und spannenden Forschungsgebiet zu arbeiten. Prof. Hanke hat Wert darauf gelegt, dass trotz intensiver mathematischer und numerischer Arbeitsphasen stets die zugrunde liegende Physik und der Bezug zum Experiment im Vordergrund steht. Man konnte sich aber auch mit nicht-physikalischen Dingen immer an Herrn Hanke wenden und ihn um seinen wertvollen Rat fragen.

Weiterhin danke ich Herrn Prof. Dr. Enrico Arrigoni für die freundschaftliche Zusammenarbeit. Von seinen exzellenten analytischen und mathematischen Fähigkeiten konnte ich in vielen Diskussionen profitieren, da er zu jeder Zeit ein offenes Ohr für Fragen und Probleme hatte, die sich im Rahmen der Forschungsarbeit ergeben hatten. Es war eine Freude mit Herrn Arrigoni zusammen zu arbeiten.

Für viele interessante und hilfreiche Diskussionen und die Überlassung einiger Programm-teile danke ich Herrn Dr. Markus Aichhorn, der vor allem in den zwei Jahren, während wir ein Büro teilten, sehr wichtig für den Erfolg meiner Arbeit war und darüber hinaus ein Freund wurde. Gleiches gilt für Herrn Prof. Dr. Michael Potthoff. Wurde eine Problemstellung auch noch so kompliziert, er nahm sich immer die Zeit, um gemeinsam und mit Erfolg an einer Lösung zu arbeiten.

Nun gilt mein Dank den Kollegen und Freunden, die ich im Laufe der Zeit kennenlernen durfte. Es gab unzählige Diskussionen über Physik aber auch viele andere Dinge, die die Arbeit ungemein bereicherten. Allen voran sei hier genannt Dr. Stephan Hochkeppel, Matthias Balzer, Dr. Martin Jöstingmeier, Dr. Andrzej Fleszar, Dr. Thomas Eckl, Dr. Christopher Dahnken, Marcel Gutberlet, Christian Platt, Thomas Lang, Jutta Ortloff, Lee Martin, Maximilian Aulbach, Manuel Protze und Zhong-Bing Huang. Bei Maximilian Kiesel möchte ich mich besonders bedanken für die wertvollen Korrekturen bei der Durchsicht meiner Dissertation.

Da ich aber nicht nur wissenschaftlich sondern auch als Systemadministrator tätig war, möchte ich Herrn Andreas Vetter und Herrn Andreas Klein für die sehr gute und freundschaftliche Zusammenarbeit danken. Ich hatte die Möglichkeit, sehr viel über Computernetzwerke von ihnen zu lernen. Weiterhin danke ich Herrn Prof. Dr. Georg Reents für die sehr gute Organisation, die er als IT-Beauftragter leistete. Weiterer freundschaftlicher Dank gebührt den Kollegen Andreas Ruttor und Guido Klingschat.

Nun danke ich den Menschen, die eine der wichtigsten Funktionen an einem Lehrstuhl einnehmen, unseren Sekretärinnen. Dies waren bei uns Christine Schmeisser, Bettina Spiegel und Judith Stahl. Die perfekte Organisation und das Wissen über Dienstvorgänge war von unschätzbarem Wert. Und nicht zuletzt stellen sie einen gewissen erfrischenden Gegenpol zu dem wissenschaftlichen Kollegium dar.

Schließlich bedanke ich mich bei den wichtigsten Menschen in meinem Leben. Dies sind meine Freundin Eva und meine Familie, besonders meine Eltern. Ihr habt mich immer unterstützt und gebt meinem Leben Wärme, Sinn und Stabilität. Vielen Dank.

Versicherung an Eides statt

Hiermit versichere ich, Sascha Brehm, geboren am 15. Mai 1978 in Fulda, an Eides statt, dass ich die vorliegende Arbeit selbstständig, d.h. insbesondere ohne Hilfe eines kommerziellen Promotionsberaters angefertigt habe. Es wurden keine anderen als die in der Arbeit angegebenen Quellen und Hilfsmittel benutzt. Diese Arbeit liegt nicht in gleicher oder anderer Form in einem anderen Prüfungsfach vor.

Würzburg, 26.02. 2009

Sascha Brehm

